ABSTRACT

Title of dissertation: ADVANCING UNDERSTANDING OF CANONICAL FIRE PHENOMENA THROUGH NOVEL EXPERIMENTAL TECHNIQUES AND DATA ANALYSIS

Xingyu Ren
Doctor of Philosophy, 2021

Dissertation directed by: Professor Michael J. Gollner
Department of Fire Protection Engineering

Physical modeling of both stationary fires and wildland fire spread requires a thorough understanding of underlying heat transfer processes which result from the interaction of flames with their surrounding environment. However, the hostile fire environment makes it difficult to conduct detailed experiments that measure and describe common thermal phenomena in many of these configurations, limiting both our understanding and the opportunity for model validation. In this dissertation, new measurement techniques were developed to characterize the thermal and fluid structures of three canonical fires: a buoyant-driven flame, a wind-driven flame, and an inclined flame, providing both enhanced understanding and new data for model validation.

The first experiment applied a dual-thermocouple technique to turbulent buoyant flame measurements with a newly developed method for uncertainty analysis. A 15 kW turbulent buoyant diffusion flame was established over a round gas burner

with a 13.7 cm inner diameter at FM Global's laboratory. A dual-thermocouple probe, consisting of two fine-wire thermocouples with 25 μm and 50 μm wire diameters, was used to determine a compensated turbulent gas temperature. Flame temperatures including the mean, root-mean square (rms) and probability density function were obtained in a two-dimensional plane across the flame centerline. These temperature measurements, alongside existing data such as the radiant power distribution, local soot volume fraction and soot temperature, as well as future gas velocity measurements will provide a detailed dataset of this flame for validation and development of radiation models.

The second experiment, performed at the University of Maryland, investigated convective heat transfer from a wind-driven flame under the effect of freestream turbulence. An image analysis technique was developed to extract the sub-scale flame structures: flame streaks and troughs. It was observed that freestream turbulence initiated an earlier onset of visible coherent flame streaks. Both spacing and fluctuation frequency of the flame streaks showed a nearly quadratic growth at high turbulence intensities. This quadratic growth promoted the transition of flames to a turbulent state, which ultimately modified the overall flame heating dynamics. The forward attachment length of the flame was found to be negatively correlated to the turbulence intensity. Two heating modes, a momentum-dominated and a plume mode, were observed and found to be segregated by a critical Richardson number. The downstream heat flux was found to increase from 30 to 40 kW/m^2 in the momentum-dominated regime, when flow turbulence intensity changed from less than 1% to a level of 14.9–16.8%. Finally, it was observed that placing a bar

upstream of the burner tripped the flow to the point where the downstream flame structure closely resembled flames under the highest turbulence intensity investigated, suggesting a simplistic configuration for future study.

The third experiment developed a temperature-correlation velocimetry technique (TCV) to examine the thermal structure and flow dynamics of inclined fires. The experimental data was provided by the USDA Forest Service Missoula Fire Sciences Laboratory. A 10 kW partially premixed propane flame was first produced over a small tilt table. Shadowgraph images were taken to illustrate the motion of the flow governing the resulting inclined fire plume. Large-scale fire tests with heat-release rates ranging from 81 kW to 2.25 MW were also conducted over a large tilt table. The angle of inclination, θ, was varied between 0° and 30°. A micro-thermocouple array along the centerline of the table was used to measure downstream gas temperatures. Flames were seen to start attaching to the inclined surface at $\theta = 18°$, independent of the fire intensity. The centerline temperatures under attached flame conditions are consistent with McCaffrey's buoyant flame temperature correlation, suggesting the buoyancy-driven nature of the inclined fires. The local gas velocity was measured using cross-correlation velocimetry through the streamwise temperature signals. Results show that the local flow was accelerated in the attached flame region driven by buoyancy before reaching a peak. Velocity of the flow slowed after the peak due to weaker buoyancy within the intermittent and plume regions. The mean surface velocity of the attached flame scales directly with the angle of inclination ($\sin^2 2\theta$) and the fire intensity ($\dot{Q}'^{2/3}$) , providing a promising method to evaluate convective heat transfer using the geometry of an inclined fire.

ADVANCING UNDERSTANDING OF CANONICAL FIRE PHENOMENA THROUGH NOVEL DATA ANALYSIS

by

Xingyu Ren

Dissertation submitted to the Faculty of the Graduate School of the
University of Maryland, College Park in partial fulfillment
of the requirements for the degree of
Doctor of Philosophy
2021

Advisory Committee:
Professor Michael J. Gollner, Chair & Advisor
Professor Arnaud Trouvé
Professor Stanislav I. Stoliarov
Professor Peter B. Sunderland
Professor James Baeder, Dean's Representative

Acknowledgments

My PhD research started at the University of Maryland, moved forward at FM Global, and finished up at the University of California, Berkeley. This journey has been wonderful primarily because of the people who have supported me along the way. First and foremost, I would like to thank my advisor, Prof. Michael J. Gollner, who has provided me enormous chances and guided me throughout the past four years. His consistent support and encouragement were vital in making this dissertation a reality. Michael has the magic power to motivate me whenever I feel frustrated, and this has allowed me to achieve some remarkable results. His dedicated work ethic and enthusiasm impressed me and will serve as a personal goal for my future career.

I express my deepest appreciation to my committee members: Professor James Baeder, Peter B. Sunderland, Stanislav I. Stoliarov and Arnaud Trouvé. They have been very supportive during the course of my Ph.D. research. Special thanks to Prof. Arnaud Trouvé whose valuable inputs from the fire modeling perspective have greatly improved this dissertation.

I was also fortunate to have the opportunity to work with some of the excellent researchers at FM Global. Much gratitude to Dr. Yi Wang, Dr. Dong Zeng and Dr. Gang Xiong whose critical thinking and professional attitude have helped push this research to a better stage. The experimental concepts and skills I learned from you will pay off forever. Thank you for inviting me to your sweet parties which added so much fun to my stay at Boston.

I also had great pleasure of working with Dr. Mark Finney and Dr. Torben Grumstrup at the Missoula fire sciences lab in Missoula. They have shared valuable large-scale experiments data and provided magnificent inputs to my work during the Covid-19 pandemic. Thank you for making this work completed.

I would like to extend my sincere thanks to Prof. Simo Mäkiharju at the University of California, Berkeley. This work has greatly benefited from his professional inputs from the fluid mechanics perspective.

I would also like to thank Dr. Yu Hu, Michael V. Heck, Evan T. Sluder, Janis Tieck and Dr. Xiaoyu Ju for their important contributions to the experiments. I am very thankful for the great discussions with Dr. Yan Ding, Dr. Mohammadhadi Hajilou, Priya Garg, Dr. Sriram B. Hariharan, Dr. Franz Richter, and Dr. Cong Zhang. Many thanks to my colleagues at the Department of Fire Protection Engineering (FPE), University of Maryland: Dr. Salman Verma, Dr. Dushyant M Chaudhari, Dr. Zhengyang Wang, Dr. Wei Tang, Dr. Rui Xu, Dr. Dennis Kim, Dr. Raquel Hakes, Dr. Tao Xu, Dr. Junhui Gong, Dr. Zhengxiang Tao, Joseph Dowling, Lana Benny, Luying Zhai, Shiyun Wu, Xinyu Fan, Hong Zhu. Special thanks to the Department of Mechanical Engineering, University of California, Berkeley for hosting me in the past two years.

Finally, I would like to thank my parents for their love and support throughout this journey. Thank you so much for believing in me.

Financial support for this work was provided by the National Science Foundation through CBET award 1554026.

Table of Contents

List of Tables

List of Figures

Chapter 1: Introduction

1.1 Wildland Fire

Wildland fires are an essential process in Earth's ecosystems. Yet, the unwanted destruction resulting from wildland fire's huge energy release and associated smoke generation has threatened many communities, human health and natural resources [1]. Satellite data shows that the global annual area burnt was nearly 840 million acres from 2000 to 2015. In the United States, wildland fires occur year round in the southern and western regions (see Fig. 1.1). Data from the National Interagency Fire Center (NIFC) [2] shows that 5 million acres of land were burnt by wildland fires annually from 1983 to 2020; this number increases to 7.5 million if looking at the data from the most recent 10 years. More than 10 million acres of land were burnt in the years 2015, 2017, and 2020. Although the number of fires in the U.S. has decreased over the past two decades, the size and severity of these fires have drastically increased, as illustrated in Fig. 1.2. Beyond acreage burned, since 2005 over 89,000 structures have been destroyed by wildland fires in the United States, including the destruction of whole communities, untold numbers of fatalities, and tens of billions of dollars in financial losses [3]. Fire modeling has the potential to alleviate some of this destruction, through fire spread predictions, suppression

planning, fire risk analysis, and realistic training. Improving these models to more accurately predict the spread of fires is necessary for these tools to remain accurate, especially for the largest and most intense fires which tend to cause the majority of destruction.

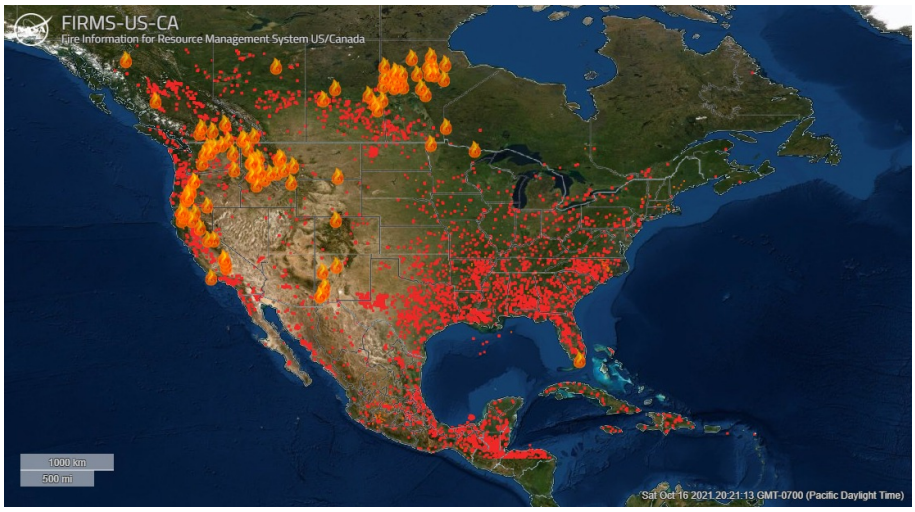

Figure 1.1: US and Canada fire map with the fire symbols representing active fires larger than 1000 acres (date: Oct. 11 to 17, 2021). Credit: Fire Information for Resource Management System.

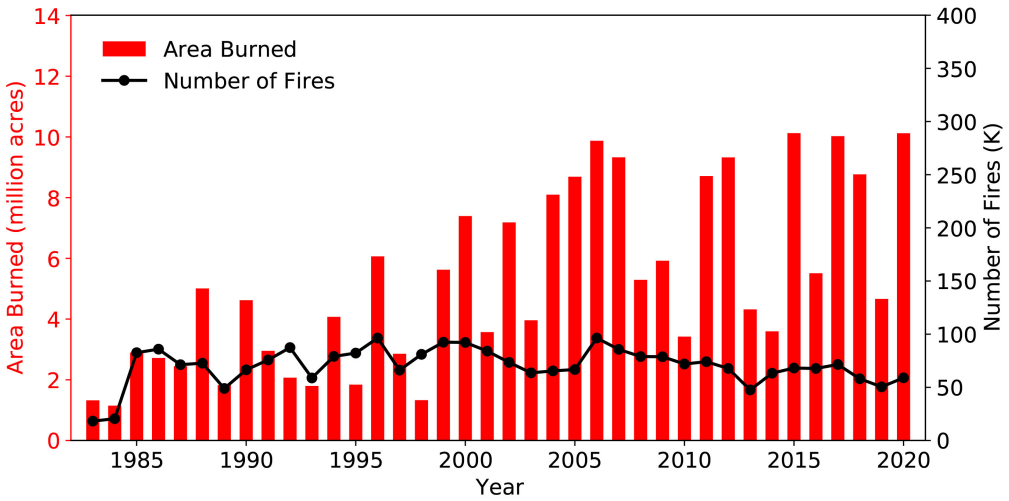

Figure 1.2: The number of and area burned from wildfires in the US. Data Credit: National Interagency Fire Center.

1.2 Modeling fire spread

Fire spread is a coupled process which consists of energy release from gas-phase combustion of pyrolysis gaseous, transport of a portion of this energy to unignited fuel, and heating of this fuel to the point where it releases combustible gaseous at a rate that will maintain a self-sustained flame, often assumed to be a constant ignition temperature for a solid fuel [4]. A fundamental thermal model which describes this process was proposed by Williams [5],

$$\rho V \Delta h = \dot{q}^{''}, \tag{1.1}$$

where ρ is the fuel density, V is the rate of fire spread, Δh is the difference in thermal enthalpy between ignited and un-ignited fuel, and $\dot{q}''$ is the net heat flux to the surface of the fuel. Many fire spread models are based on Eq. 1.1 but with different bias on the selection of the dominant heat transfer mode. The three most common heat transfer modes are conduction, radiation and convection. However, for wildland fire scenarios where the fuel elements are often discrete, conduction heat transfer is less likely to dominate the fire propagation. Therefore, the principal mechanisms are usually radiation and convection of hot gases [5]. However, incorporating these physical processes into a wildland fire spread model is challenging, mostly due to the lack of a fundamental theory. Existing physically based models are found to be using assumptions without an experimental basis, thus failing to predict the ignition of fuel elements and subsequent fire spread [6].

Prediction of the ignition process is critical since fire spread results from sustained ignition. Equation 1.1 is only valid when the net energy input ($\dot{q}''$) is large enough to ignite the fuel. However, how ignitions occur at fine-fuel particle scales is not yet fully understood. Usually, fuel elements can be characterized using the fuel size and shape, moisture content, and chemical composition [6]. The last two parameters can be characterized using laboratory-scale experiments and used in large-scale wildfire application, regardless of the fuel size. However, the heat transfer model for different fuel sizes cannot be generalized. Recent findings have shown that ignition of a fuel element is not dominated by a single heat transfer mode, but rather is controlled by a mixed process of radiant heating, convective heating, and convective cooling, depending on the characteristic size the fuel. In wildland fire scenarios, the size of the fuel elements range from 10^{-3} to 10^{0} m with a general classification for fuel size based on the time lag for evaporation in the US as: 1 hr: $< 1/4''$ (0.64 cm), 10 hr: $1/4''$ (0.64 cm) $\sim 1''$ (2.54 cm), 100 hr: $1''$ (2.54 cm) $\sim 3''$ (7.62 cm), 1000 hr: $3''$ (7.62 cm) $\sim 8''$ (20.32 cm), as illustrated in Fig. 1.3. Precise prediction of fuel ignition across different scales is then necessary for modeling wildland fire spread. For that purpose, we need to have a thorough understanding of the role of different heat transfer mechanisms in wildland fires.

1.2.1 Role of radiation

A critical question within the research community is which heat transfer mode dominates wildland fire spread: radiation or convection? The fire research commu-

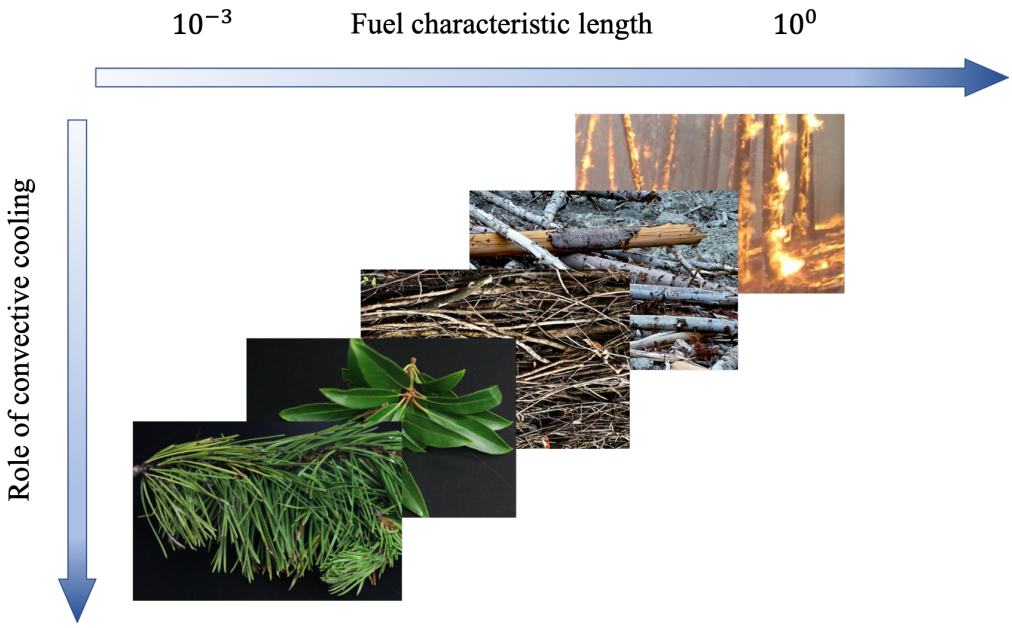

Figure 1.3: Wildland fuels with different sizes

nity has not come to a firm conclusion yet. Often times, it is "a modeller's judgment that determines the process assumptions without an experimental basis", as stated by Finney et al. [6]. Consequently, a portion of wildland fire spread models were developed with radiation as the controlling heat transfer mechanism as large fires tend to have observably high radiative heat fluxes which could govern the rate of fire spread [7].

With the assumption that the developed flame zone blocks most forward convective heat transfer, Albini [4] developed a radiation dominated wildland fire spread model. The propagating flame front was treated as a steady plane which acts as a perfect diffuse radiator that provides the heat for fire spread. In later work [8], he revised the model to include cooling of the fuel by natural convection. However, initialization of the fuel temperature distribution was based on the occurrence of ignition rather than experimental observation, which has demonstrated that con-

vective cooling effectively offsets radiative heating [6] and thus, ignition for fine fuels. Similarly, a significant number of works on wildland fire spread assumed radiation as the dominant heat transfer mode [9–17]. There are several reasons behind this selection. First, isolated measurements of radiative and convective heating in a propagating fire are lacking. Flow field measurements in large-scale fires are challenging and thus, limited towards understanding convective heat transfer. Second, experiments that characterize the fine-fuel particle ignition process are missing. Finally, for large-scale wildland fires, in particular for crown fires, it is argued that the vertical buoyant force is so strong that the majority of the forward convection is blocked.

These arguments have been challenged by others from both numerical and experimental perspectives [6, 18, 19]. The most common finding is that radiation is insufficient to heat adjacent fine-fuel particles ($0.02 \sim 0.025$ m away from the flame base) to the ignition temperature. Dupuy et al. [20] measured the radiant heat flux 10 cm ahead of a spreading fire with fuel beds made from *pinus halepensis* needles. A 1.3 ± 0.5 kW/m^2 and a 4.6 ± 0.6 kW/m^2 radiant heat flux were measured when the heat flux gauge was placed perpendicular and parallel to the fuel beds, respectively. Such a heating power is not enough to ignite the un-burned fuel. As this laboratory scale experiment may not apply at larger scales, the role of radiation in fire spread through discrete particles needs to be re-examined at multiple scales.

1.2.2 Role of convection

The role of the convection in fire spread can be separated into convective cooling and convective heating, depending on the temperature difference between the fuel and the surrounding gases. As discussed in section 1.2.1, a heated fine-fuel particle is subject to convective cooling, which is caused by the low-temperature air flow induced by the heated fuel. Although convective cooling has been considered in wildland fire spread models [8, 19], the appropriateness of this term and its implications have not yet been evaluated. Carefully designed experiments are needed to examine the role of convective cooling on fuel particle ignition.

Given the fact that fires continue to spread with insufficient radiation and substantial convective cooling, it is reasonable to re-think the contributions of the convective heating. Byram et al. [21] have concluded that 'the nearly continuous envelopment of the surface fuel for some distance ahead of the leading edge of the active burning zone plus random flame contacts at greater distances ignite the surface fuel'. In other words, it is impingement of the flame (or high-temperature plume) that heats the fuel in the manner of convection. Convection could be dominant considering the high-temperature combustion gas and the substantial velocity associated with the propagating flame. The results of both small-scale and large-scale experiments using *matchstick*, *wooden dowel*, *excelsior*, and laser-cut *cardboard* arrays [18,22–26] have clearly demonstrated the dominant role of convection. However, quantification of the convection versus radiation in flame spread is still limited.

Singh et al. [27] directly measured the convective heat flux of vertical laminar

wall flames (methanol and ethanol) using the local temperature gradient. A $\sim$ 20 kW/m^2 convective heat flux from the flame to the wall was obtained, which is more than 85% of the total heat flux. This is reasonable since the flame is less sooty compared to the common wildland fires. Ju et al. [28] measured the radiative and total heat fluxes for turbulent wind-driven methane and propane fires, finding that the convective heat flux (total $-$ radiative) is almost 60% higher than the radiation. Similar measurements were also conducted for spreading fires. Silvani and Morandini [29, 30] measured the radiative and total heat fluxes of a spreading fire over *excelsior* beds with inclination. Although they stated that the difference between the total and radiation is not equal to the convection due to measurement uncertainty, multiple surges of such differences were observed, being much higher than radiation. The simultaneous occurrence of the surge of the total heat flux and the fast spread of the flame leads to questions concerning the contribution of the convective heating.

Aside from the inconclusive experimental research on the role of the convection, the heating mechanics of convection in wildland fire scenario has not been fully understood yet. Recent findings [26, 31, 32] on the convection dynamics indicate that the previous time-averaged or uniformly heating concept may not be suitable for modeling wildland fire spread. Coherent flame structures (see Fig. 1.4) have been observed over a wide range of scales, ranging from saw toothed structures in large-scale wind-driven wildland fires to coherent streamwise streaks in bench-scale boundary-layer flame experiments. Experiments at smaller scales have shown how coherent structures in laminar flames can modify heat transfer from flames

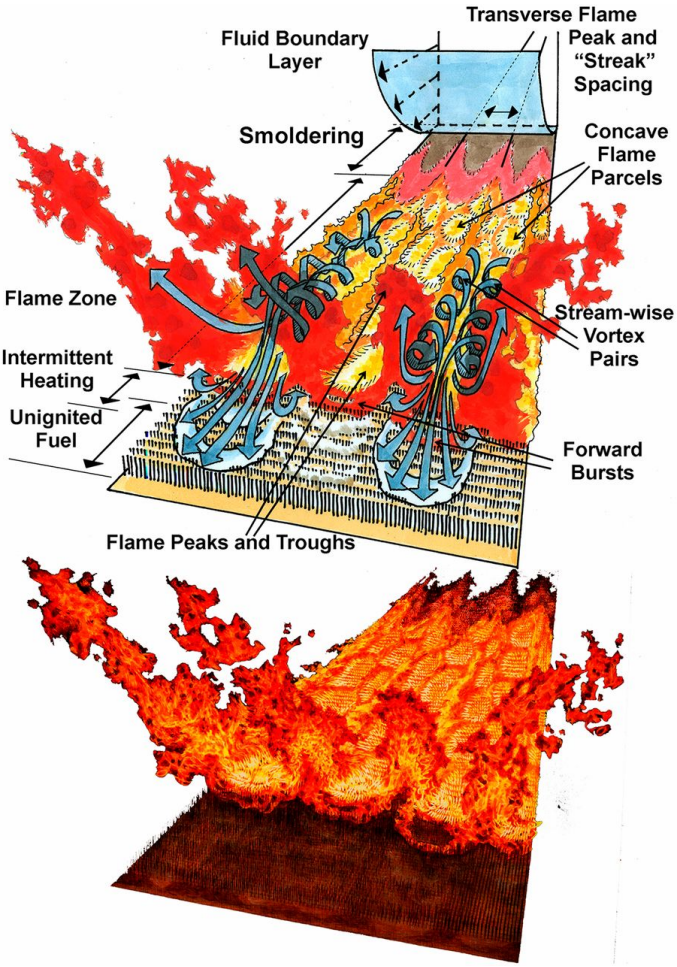

Figure 1.4: Illustrations of flame dynamics and related flow instabilities observed in experimental burns. Flame-zone buoyancy creates stream-wise vortex pairs that alternately push flames up into peaks and down into troughs. Concave flame parcels travel through the flame zone and burst intermittently forward through the troughs to heat unignited fuels [26]

to downstream surfaces, by redistributing hot combustion gases [31, 32]. Large-scale studies on spreading fires have identified the production of intermittent high-temperature fluctuations ahead of spreading flame fronts [26], presumed to occur due to the formation of counter-rotating vortices [33]. These findings affirmed the three-dimensional nature of many boundary-layer flames [34]. Physical processes reflecting these three-dimensional structures may have to be considered for the prediction of wildland fire spread, where the traditional lumped heat transfer model is no longer

suitable.

1.2.3 Effect of topography

When fire spreads upslope, both radiation and convection can be enhanced [20]. As the slope increases, fires tend to bend toward the uphill surface, mostly due to a combination of buoyancy-induced flow and a 'blockage' effect between the flame and downstream surface. Such an effect elongates the flame height and reduces the angle between the flames and the preheated fuel bed, thus resulting in an enhanced radiant heat flux onto the fuel bed. As for convection, a 'critical angle' often acts as a threshold that separates the convective cooling and heating. Fuel ahead of the flame is cooled by the air entertainment when the slope is low. Once the slope is higher than the 'critical angle', the hot combustion gas dominates the flow, and thus heating the unburnt fuel through convection. In summary, the inclination angle of the slope may determine the dominate heating mode.

1.3 Challenges, Motivation, and Scope

To examine the aforementioned physical processes, experiments are needed. However, the hostile fire environment makes it difficult to conduct detailed experiments that measure and describe common thermal phenomena in many of these configurations. Diagnostic techniques used for low-temperature measurements are no longer suitable. On the other hand, local gas temperatures, flow velocities, subscale flame structures, and other detailed fire properties are needed for the charac-

terization of these physical phenomena and future wildland fire model development. Towards that purpose, the development of new methodologies and techniques is needed.

This dissertation aims to develop new methodologies and techniques to provide improved insight into the fire heat transfer processes and establish validation dataset for fire model evaluation. Experiments were ultimately conducted to characterize the thermal and fluid structures of three canonical fires: a buoyant-driven flame, a wind-driven flame, and an inclined flame.

The first experiment applied a dual-thermocouple technique to turbulent buoyant flame measurements with newly developed uncertainty analysis method. A 15 kW turbulent buoyant diffusion flame was established over a round gas burner with a 13.7 cm inner diameter at FM Global's laboratory. A dual-thermocouple probe, consisting of two fine-wire thermocouples with 25 μm and 50 μm wire diameters, was used to determine a compensated turbulent gas temperature. Flame temperatures including the mean, root-mean square (rms) and probability density function were obtained in a two-dimensional plane across the flame centerline. These temperature measurements, alongside existing data such as the radiant power distribution, local soot volume fraction and soot temperature, as well as future gas velocity measurements will provide a detailed dataset of this flame for validation and development of radiation models.

The second experiment, performed at the University of Maryland, investigated convective heat transfer from a wind-driven flame under the effect of freestream turbulence. An image analysis technique was developed to extract the sub-scale

flame structures: flame streaks and troughs. A wind-driven fire experiment was conducted with the flame being disturbed by freestream turbulence. Homogeneous grid-generated turbulence was produced in a wind tunnel via a perforated grid; the corresponding turbulence intensity was adjusted through varying the grid size. Local flame coherent structures reflecting the heat transfer processes, in particular, the generation of streamwise streaks, as well as the corresponding streak spacing, and streak time scale were evaluated under different turbulence intensities. Meanwhile, the flame's overall attachment length and heat flux to the surface were captured to illustrate the global influence of freestream turbulence.

The third experiment developed a temperature-correlation velocimetry technique (TCV) to examined the thermal structure and flow dynamics of inclined fires. The experimental data was privoded by the USDA Forest Service Missoula Fire Sciences Laboratory. A 10 kW partially premixed propane flame was first produced over a small tilt table. Shadowgraph images were taken to illustrate the motion of the flow governing the resulting inclined fire plume. Large-scale fire tests with heat-release rates ranging from 81 kW to 2.25 MW were also conducted over a large tilt table. The fundamental relationships that govern the coupling effect among slope, fire intensity and fire-induced flow were investigated. Meanwhile, this experiment aims to provide additional flow velocity measurements for the flame characterization of inclined line fires. Using cross-correlation velocimetry, the flow velocity was derived from the temporal temperature profiles of a thermocouple array. Finally, a generalized relationship was proposed to correlate the mean flow velocity in the flame zone using the fire intensity and angle of inclination.

Chapter 2: Buoyant-driven Turbulent Diffusion Flame

This chapter investigates the thermal structure of a turbulent buoyant ethylene diffusion flame. In alignment with the IAFSS Working Group on Measurement and Computation of Fire Phenomena (i.e., the MaCFP Working Group), a detailed temperature dataset for the *Flame Extinction* target case under the *Gas Phase Phenomena Subgroup* was sought. Medium-scale, 15 kW ethylene diffusion flames are produced using a 15.2 cm round water-cooled burner with a controlled co-flow at FM Global's laboratory [35]. Local gas temperatures were measured using a dual-thermocouple (dual-TC) probe made with two type-S fine-wire thermocouples. This test case is intended to provide a dataset to validate soot and radiation models in buoyant flames. The radiative characteristics, including radiant power distribution, local soot volume fraction and soot temperature under normal and reduced-oxygen conditions have been reported in [35,36]. Here, temperature measurements including local mean, root-mean square (rms) fluctuation, and probability distribution profiles are presented, which are necessary for future development of this validation dataset.

2.1 Introduction

Fire modeling has become a critical tool in fire science, used in both research and applied design scenarios. Two large-eddy simulation (LES)-based models in particular are commonly used in the field, FireFOAM [37, 38] and the Fire Dynamics Simulator (FDS) [39]. Fundamental physical and chemical models are integrated into these computational codes to capture multi-physics, multi-scale fire dynamics including a combination of chemical reactions, turbulent mixing, thermal and fluid dynamics. In order to use these models for research or applied scenarios, validation must occur both for realistic scenarios and of underlying physical models used in simulations. In order to perform such validations, high accuracy experimental datasets are needed.

The gas-phase temperature serves as an important fire characteristic, as it provides a direct scalar comparison with computational results. However, the turbulent reactive flow field in fires makes it challenging to obtain time-resolved temperature information. To date, researchers have used thermocouples, thin-filament pyrometry, multi-color optical probes and coherent anti-Stokes Raman scattering (CARS) thermometry to measure local gas temperatures in various configurations. CARS [40] appears to be the most unobtrusive way to measure local gas temperature without modifying the flame; however, the complex experimental setup requires an extensive investment and considerable calibration. Thin-filament pyrometry has also been successfully applied on both a methanol pool fire and a blue whirl [41–43]; however, this technique is limited to soot-free flames which don't reflect most practi-

cal scenarios. Multi-color optical probes feature simultaneous soot volume fraction and temperature measurements, however only soot, not gas temperature can be detected [35]. Thermocouples, on the other hand, have been widely used for high temperature measurements [44–46]; however, physical and mathematical models need to be employed to account for the thermal inertia of the thermocouple bead under turbulent, fluctuating fire conditions.

Several methods have been proposed to compensate for the thermal inertial effect and reconstruct the true local temperature from raw thermocouple readings [47–56]. The frequency response of a thermocouple, in principle, is a first-order lag system and can be compensated for using a first-order coefficient, namely a time constant. For a steady combustion process, the mean time constant of a thermocouple bead can be determined using an electrical heating method [50]. However, the dramatic fluctuations in both temperature and velocity in a fire environment leads to a varying time constant, where use of a mean value might lead to both over- and under-compensation of temperature signals. Measurement of the instantaneous time constant in turbulent conditions can be extremely difficult as it is a function of the local temperature and velocity, requiring synchronized measurements [51]. Previously, a dual-thermocouple technique has been proposed to estimate the fluctuating time constant without direct measurement of velocity [52–54]. This technique relies on assumption of fixed bead sizes of the thermocouples, which may change in sooty environments, ultimately introducing large errors [52]. Further improvements of the dual-thermocouple technique show a possible application in sooty flames, as the instantaneous time constant can be estimated without assuming bead diameters, only

incorporating diameters to compensate for radiant losses [55, 56].

2.2 Experimental setup

2.2.1 Water-cooled enclosure and gas burner

A 1.22 by 1.22 m^2 wide, 1.83 m tall water-cooled enclosure [35] with matte black interior walls was employed to conduct turbulent buoyant diffusion flame experiments, as show in Fig. 2.1. Air co-flow was supplied by a rotameter at a flow rate of $\sim$ 43 L/s, which provides more than 10 times the stoichiometric oxidant requirement of the fuel. To ensure a uniform co-flow, a flow distribution section consisted of several screens and a layer of 3.81 cm sand ($\sim$ 0.07 cm diameter) was installed at the bottom of the enclosure. During each test, products of the combustion were discharged through an exhaust duct at the top of the enclosure.

A buoyancy-driven turbulent diffusion flame was established on a water-cooled round gas burner with a 15.2 cm outer diameter (D) and a 13.7 cm inner diameter. Chemically pure ethylene (>99.9 %) was fed through a mass flow controller (Sierra C100M-DD-3-OV1-SV1-PV2-S0) to the burner with a 15 kW theoretical heat release rate (HRR). Before reaching the burner surface, fuel passes through a honeycomb with a 0.32 cm cell size and 2 cm thickness followed by two layers of coarse and fine steel beads (with a 2.54 cm thick layer of 0.48 cm diameter beads and a 2.54 cm thick layer of 0.31 cm diameter beads, respectively) to assure a uniform exit flow velocity. During each test, the water-cooled burner surface remains at about 353 K.

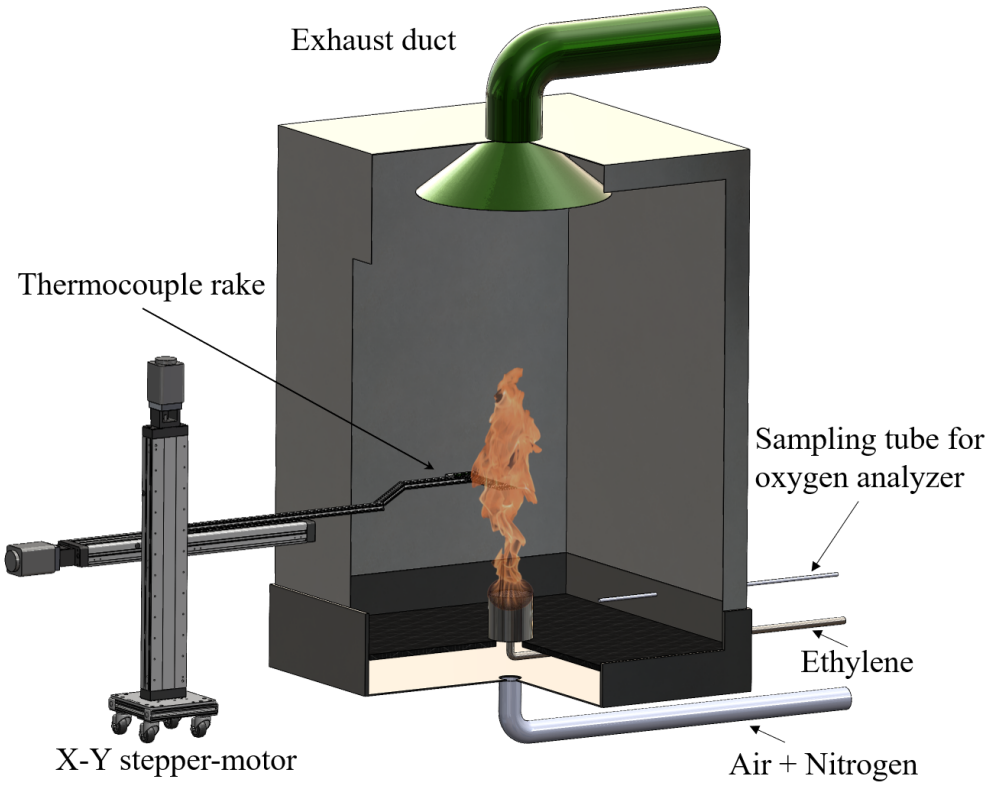

Figure 2.1: Gaseous round burner setup in a water-cooled enclosure.

2.2.2 Thermocouples

2.2.2.1 Thermocouple calibration

For a given temperature, a thermocouple outputs a voltage signal. To convert the voltage signal to temperature reading, a NIST conversion table is used [57]. A type-S micro-thermocouple with a 25 μm wire diameter ($\sim$ 88 μm bead diameter) was calibrated against a black-body (IR-301 Controller), with a black-body temperature ranges from 1073 K to 1473 K. The results are displayed in Fig. 2.2. A maximum of 9 K difference is observed between the black-body temperature and the thermocouple measured temperature, with a relative error less than 0.6%.

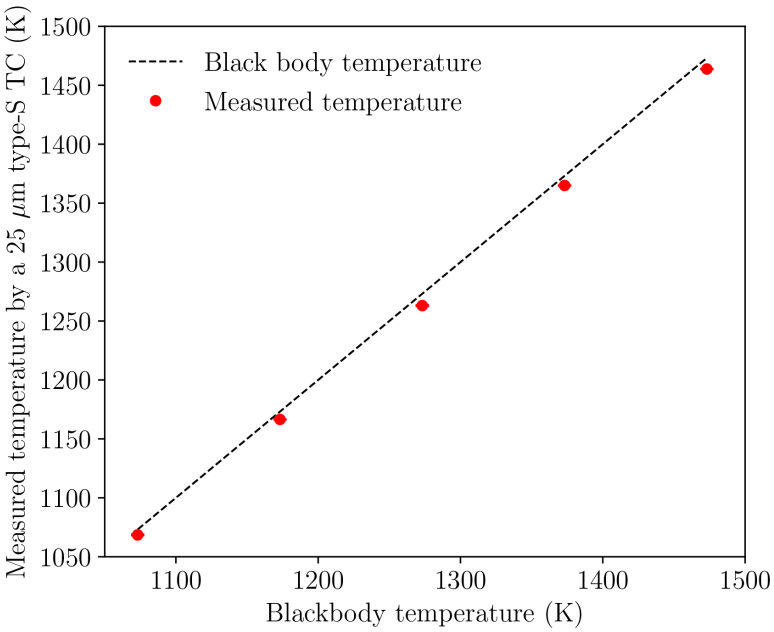

Figure 2.2: Thermocouple calibration

2.2.2.2 Dual thermocouple

The dual-thermocouple pair was made with two type-S thermocouples, with 25 μm and 50 μm wire diameters (Omega Engineering, P10R-001 and P10R-002). The corresponding average bead diameters are measured as 88 μm and 126 μm, respectively, using a microscope. The thermocouple wires were supported by a single 1.6 mm diameter twin bore ceramic cylinder (Omega Engineering, TRX-164116) with a $\sim$ 8 mm length of thermocouple wire exposed. Analysis of the single-thermocouple method was performed using the data of the 25 μm wire diameter thermocouple.

2.3 Single- and dual-thermocouple techniques

2.3.1 Single thermocouple method

A energy balance for a single thermocouple (Single-TC) bead under an unsteady turbulent flame with negligible conduction to lead wires can be written as

$$mc_p \frac{dT_{th}}{dt} = A[(T_g - T_{th})h - \epsilon\sigma T_{th}^4 + \varepsilon \dot{q}''_{rad}], \tag{2.1}$$

where the left-hand side (LHS) of the equation represents the energy change of the thermocouple bead, m is the bead mass (kg), c_p is the bead heat capacity ($\mathrm{Jkg^{-1}K^{-1}}$), and T_{th} is the thermocouple bead temperature (K). The right-hand side (RHS) includes convective heating/cooling, radiant heat losses from the bead, and radiant heat absorption of bead from the surrounding fire, respectively. Heat absorption from the ambient air is sufficiently small and is ignored. Here, A is the bead area ($\mathrm{m^2}$), T_g is the local gas temperature (K), h is the heat-transfer coefficient ($\mathrm{Wm^{-2}K^{-1}}$), ε is the bead emissivity (assumed to be 0.95 for soot-coated bead), and $\dot{q}''_{rad}$ is the radiant heat flux ($\mathrm{W/m^2}$) from the surrounding fire. Eq. 2.1 can be re-written with T_g on the LHS,

$$T_g = T_{th} + \frac{V}{A}\frac{\rho c_p}{h}\frac{dT_{th}}{dt} + \frac{1}{h}(\varepsilon\sigma T_{th}^4 - \sigma \dot{q}''_{rad}) \tag{2.2}$$

where h can be calculated as $(\mathrm{Nu}k_g)/d$, with Nu representing the Nusselt number, k_g being the temperature-dependent thermal conductivity ($\mathrm{Wm^{-1}K^{-1}}$) of gas, and d

being the thermocouple bead diameter (m). Further, V/A represents the inverse of a surface to volume ratio of a thermocouple bead and ρ is the bead density (kg/m^3). According to observations of thermocouples used in this study using a microscope, a spherical structure is assumed for the thermocouple beads, providing $V/A = d/6$. In some previous studies a cylindrical structure is also used [48, 55], resulting in $V/A = d/4$. Substituting the above parameters into Eq. 2.2 provides

$$T_g = T_{th} + \frac{\rho c_p d^2}{6\mathrm{Nu}k_g}\frac{dT_{th}}{dt} + \frac{d}{\mathrm{Nu}k_g}(\varepsilon\sigma T_{th}^4 - \varepsilon\dot{q}''_{rad}), \tag{2.3}$$

where

$$\mathrm{Nu} = 2 + 0.6\mathrm{Re}^{0.5}\mathrm{Pr}^{0.4} \tag{2.4}$$

and

$$\tau = \frac{\rho c_p d^2}{6\mathrm{Nu}k_g}. \tag{2.5}$$

Using a Nu correlation for flow around a sphere [58] from Eq. 2.4, where Re is the Reynolds number (Ud/μ, where μ is the kinematic viscosity of the fluid in m^2/s), and Pr is the Prandtl number (μ/α, where α is the thermal diffusivity of the fluid in m^2/s), the time constant can be calculated using Eq. 2.5, ultimately becoming a strong function of local gas velocity, temperature and bead diameter, i.e., $\tau = f(U, T_g, d)$. The local gas temperature in Eq. 2.3 can then be solved after accounting for any additional external $\dot{q}''_{rad}$.

In practice, the complex geometry of the thermocouple bead and wire combination leads to large uncertainties in bead diameter. Especially for sooty flames,

soot deposits on the thermocouple bead due to thermophoresis and leads to growth of the bead size throughout the duration of measurements. To determine the influence of this phenomena on measured temperatures and response rates, a sensitivity and uncertainty study was conducted. A temperature signal sampled in the flame centerline at a height of $2.5D$ was used. Normalized sensitivity $s(T_{g,i})$ and absolute uncertainty values $u(T_{g,i})$ were calculated using following equations [59, 60],

$$s(T_{g,i}) = \frac{x_i}{T_{g,i}} \frac{\partial T_{g,i}}{\partial x_i}, \tag{2.6}$$

$$u(T_{g,i}) = \Delta x_i \frac{\partial T_{g,i}}{\partial x_i}, \tag{2.7}$$

where x_i is the input variable at step i and Δx_i is the uncertainty of any input parameter x_i. Fig. 2.3(a) shows the sensitivities of the time-resolved compensated T_g signal to the measured parameters. We can see T_g is very sensitive to the original thermocouple output temperature T_{th} and bead diameter d, and less sensitive to the local gas velocity U and radiant heat flux $\dot{q}''_{rad}$.

In experiments, the relative uncertainty of T_{th} is relative small, estimated to be $\pm$ 0.60% for a type-S thermocouple and associated data acquisition system, thus the overall T_g uncertainty is $\pm$ 22 K within a 95% confidence interval (CI) in the flame, shown in Fig. 2.3(b). For velocity measurements, a 1.4 m/s flow velocity has been used based on previous measurement at FM Global using particle image velocimetry (PIV). A 20% measurement uncertainty is assigned in this analysis due to the fluctuating fire environment, with a resulting uncertainty of $\pm$ 14 K at 95%

CI. For a small thermocouple bead, the effect of radiant heat flux on the temperature correction can usually be ignored. In the present work, with a 15 kW ethylene flame approximately 0.7 m in height and 0.152 m in diameter, the radiant heat flux to a thermocouple bead at the flame centerline and a height of $2.5D$, may be as high as 45 kW/m^2, see Appendix A. This external radiant heat flux results in an uncertainty ranging from $-$ 28 K to $-$ 16 K in a 95% CI for the 25 μm diameter wire (88 μm bead diameter). The bead diameter, on the other hand, is conservatively estimated to change only 20%, even though soot deposition may cause even more significant changes. The resulting uncertainty reaches $-$ 199 K to 297 K in a 95% CI. The preceding analysis demonstrates that the single-TC compensation method is most sensitive to thermocouple bead diameter, with inaccurate bead size measurements leading to large temperature uncertainty, which may be exacerbated in sooty flames.

Notice that the thermocouple bead emissivity was treated as soot emissivity according to the experimental observation. If considering an emissivity of the thermocouple material (platinum-10% rhodium), e.g., $\bar{\varepsilon} \approx 0.158$ for a $T_g = 1200$ K [61], uncertainties of measurement change to $\pm$ 21 K for the thermocouple and data acquisition system, $\pm$ 13 K for the flow measurement uncertainty, -5 to -3 K for the external radiant heat flux, and - 206K to 294 K for the thermocouple bead diameter uncertainty. The uncertainty caused by the external radiant heat flux dramatically decreases for a clean bead surface.

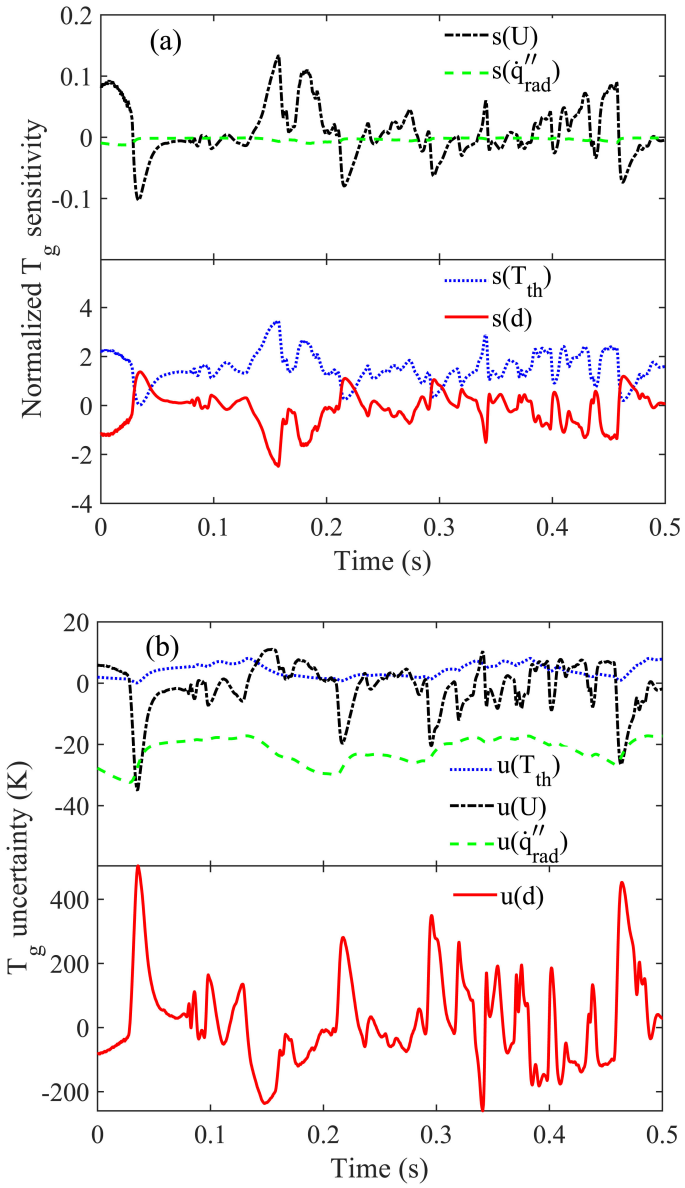

Figure 2.3: Time-resolved sensitivities (s) and uncertainties (u) of single-TC method: (a) Normalized T_g sensitivities, (b) Absolute T_g uncertainties.

2.3.2 Dual-thermocouple method

A dual-thermocouple (Dual-TC) method has been proposed by Tagawa and Oath [55] to compensate the local gas temperature which is less affected by the geometrical features of the thermocouple beads. The basic assumption is that, by

putting two fine-wire thermocouple beads close together, typically smaller than the characteristic length of the flow, both thermocouples are under identical surrounding conditions. To find a desirable value, separation distances ranging from 0.4 to 3.8 mm were tested using two thermocouples made with 50 μm wire diameter. A 15 cm diameter methanol pool fire was selected to minimize any affects caused by soot deposition. An example of the measured temperatures by this special dual-TC with a 0.4 mm separation distance is plotted in Fig. 2.4(a). Both signals are able to reflect the same temperature fluctuations and almost overlap with each other. Disagreements are observed at peaks and troughs of the temperature signals, which could be caused by the slightly different bead size ($\pm$ 7% calculated using current data) of the two 50 μm thermocouples and the minimal spatial distance. To evaluate the similarity between the measured temperature signals, cross-correlation coefficients of the temperature fluctuations, R_{12}, were calculated as Eq. 2.8

$$R_{12} = \frac{\overline{T'_{th1} T'_{th2}}}{(\overline{T'^2_{th1}}\ \overline{T'^2_{th2}})^{0.5}}. \tag{2.8}$$

Results are displayed in Fig. 2.4(b). An R_{12} between 0.98 to 0.99 is obtained when the separation distance is smaller than 1 mm, indicating the strong similarity between these two temperature signals. Beyond this distance, a clear decreasing trend in R_{12} is observed when increasing the separation distance, indicating that signals start to deviate from each other. In this work, a 0.5 mm spatial distance is selected to ensure both thermocouples are exposed to nearly identical thermal field conditions, resulting in a cross-correlation coefficient larger than 0.99 for most of

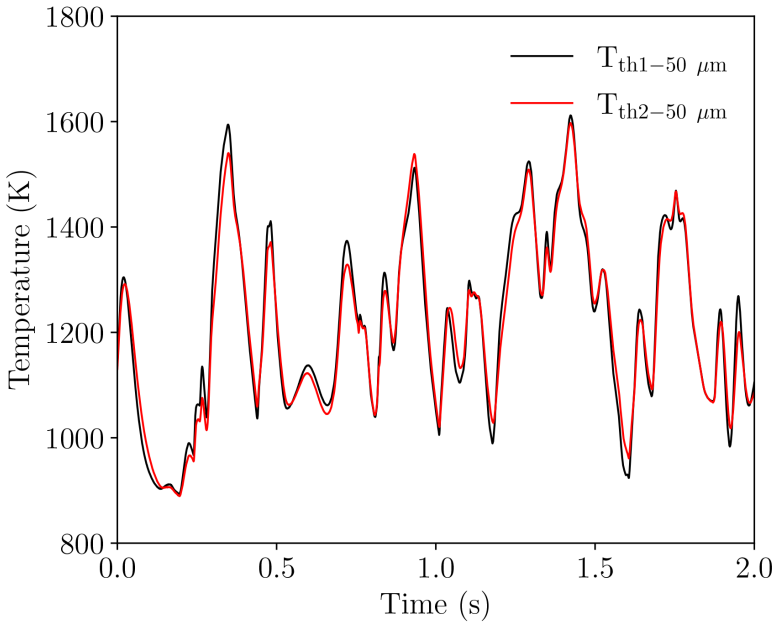

(a)

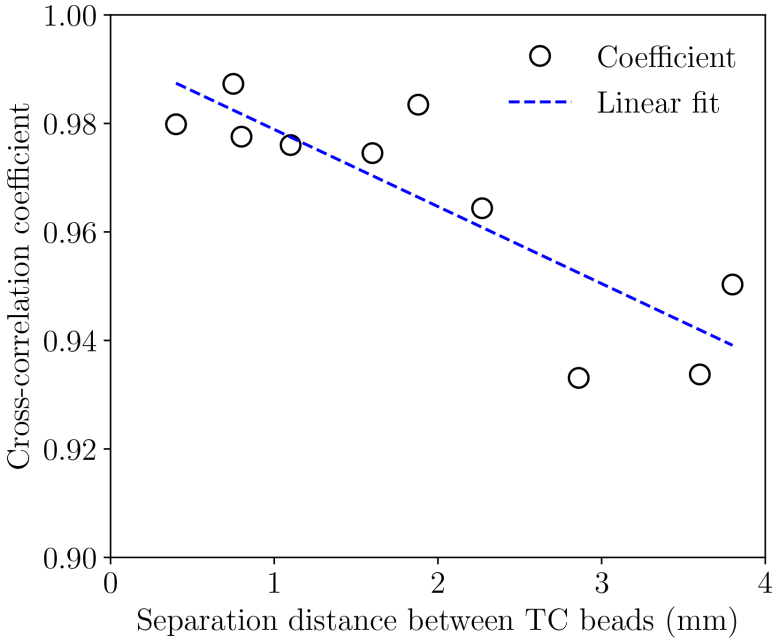

(b)

Figure 2.4: (a) Temperature difference between two 50 μm type-S TC vs. TC tip spatial distance, (b) cross-correlation of TC signals

the experimental tests.

The following two equations are then formed for two thermocouples,

$$T_{g1} = T_{th1} + \tau_1(\frac{dT_{th1}}{dt} - \frac{6}{\rho c_p})(\frac{\varepsilon \dot{q}''_{rad} - \varepsilon\sigma T^4_{th1}}{d_1}) \tag{2.9}$$

$$T_{g2} = T_{th2} + \tau_2(\frac{dT_{th2}}{dt} - \frac{6}{\rho c_p})(\frac{\varepsilon \dot{q}''_{rad} - \varepsilon\sigma T^4_{th2}}{d_1}), \tag{2.10}$$

where the subscripts 1 and 2 denote two thermocouples with wire diameters of d_1 (25 μm) and d_2 (50 μm), respectively. Assuming identical surrounding conditions,

$$T_{g1} = T_{g2} = T_g, \tag{2.11}$$

which implies that both compensated temperatures should equal the true local gas temperature. Equation 2.11 holds true for all temperature pairs; therefore, the problem is reduced to finding τ_1 and τ_2 to satisfy Eq. 2.11 for temperature pairs measured at all times. Assuming there are a total of N pairs of measurements, N of Eq. 2.9 and Eq. 2.10 can be solved for by finding τ_1 and τ_2 to minimize Eq. 2.12 using a least-squares method

$$e = \frac{\sum_1^N |T_{g1} - T_{g2}|}{N} \tag{2.12}$$

Rewrite Eq. 2.12 using Eqs. 2.9 and 2.10, we have

$$\begin{aligned} e = \sum(\Delta T_{21})^2 + \bar{\tau}_1^2\Big(\sum {G_1}^2\Big) + \bar{\tau}_2^2\Big(\sum {G_2}^2\Big) - 2\bar{\tau}_1\Big(\sum G_1\Delta T_{21}\Big) \\ +2\bar{\tau}_2\Big(\sum G_2\Delta T_{21}\Big) - 2\bar{\tau}_1\bar{\tau}_2\Big(\sum G_1 G_2\Big) \end{aligned} \tag{2.13}$$

The minimum of the e is found by setting the gradient to zero,

$$\begin{aligned} \frac{\partial e}{\partial \bar{\tau}_1} &= 0, \\ \frac{\partial e}{\partial \bar{\tau}_2} &= 0. \end{aligned} \tag{2.14}$$

The resulting time constants are calculated as

$$\begin{aligned} \bar{\tau}_1 &= \frac{\left(\sum {G_2}^2\right)\left(\sum G_1 \Delta T_{21}\right) - \left(\sum G_1 G_2\right)\left(\sum G_2 \Delta T_{21}\right)}{\left(\sum {G_1}^2\right)\left(\sum {G_2}^2\right) - \left(\sum G_1 G_2\right)^2}, \\ \bar{\tau}_2 &= \frac{\left(\sum G_1 G_2\right)\left(\sum G_1 \Delta T_{21}\right) - \left(\sum {G_1}^2\right)\left(\sum G_2 \Delta T_{21}\right)}{\left(\sum {G_1}^2\right)\left(\sum {G_2}^2\right) - \left(\sum G_1 G_2\right)^2}. \end{aligned} \tag{2.15}$$

The duration over which N pairs of temperature signals are acquired is defined as the time window. In order to include sufficient data points to evaluate τ_1 and τ_2, a time window needs to be selected that is large enough to reflect the heat transfer process but, ideally, small enough to resolve turbulent fluctuations. Moreover, the signal to noise ratio (SNR) of the turbulent flame temperature also requires a sufficient large time window to smooth out the random measurement noise. Selection of a time window that is too short may amplify the noise, which could result in unrealistic time constants. Previous literature [55, 56] suggest a time window selection between $1.5 \sim 3.0$ times of the mean time constant of the thinner thermocouple. In the present work, a 0.06 s ($\sim 4\bar{\tau}_1$, where $\bar{\tau}_1$ is the mean time constant of the 25 μm wire thermocouple) time window was used. The mean time constant $\bar{\tau}_1$ was obtained through use of all temperature pairs (i.e. a 60 s signal with a 5 kHz sampling rate, totaling 300,000 data points).

The advantage of this dual-TC scheme is that the thermocouple diameters are only used to calculate the radiant loss term, which results in less uncertainty. Measured velocities are no longer needed, which makes the experiments more convenient and cost effective. Sensitivity and uncertainty analyses were conducted to evaluate the effect of the bead diameter. Fig. 2.5(a) shows the sensitivities and uncertainties of the two thermocouple beads. Compared with the single-TC method, T_g is much less sensitive to the bead diameter. A 20% increase in diameter leads to only a – 25 K to 8 K uncertainty at a 95% CI, which is much less than the uncertainties induced by the single TC method. The temperature compensation contributed by different terms in Eq. 8 is plotted in Fig. 2.5(b). As shown, the most important term is $\tau dT_{th}/dt$, which represents the contribution of convective heating, while the radiant heat loss term, $\tau(6\varepsilon\sigma T_{th}^4/\rho c_p d)$, plays a secondary role. For the radiant absorption term, $\tau(-6\varepsilon\dot{q}''_{rad}/\rho c_p d))$, a 45 kW/m^2 heat flux leads to a temperature compensation ranging from - 31 K to - 2 K in a 95% CI. Considering the uncertainties caused by a 0.25% data acquisition error, a 20% bead size change, and a 45 kW/m^2 external radiant heat flux, the overall uncertainty on the compensated local hot gas temperature T_g was estimated at $\pm$ 41 K. Notice that the overall uncertainty can decrease to $\pm$ 23 K for soot-free condition where $e \approx 0.158$ at $T_g = 1200$ K.

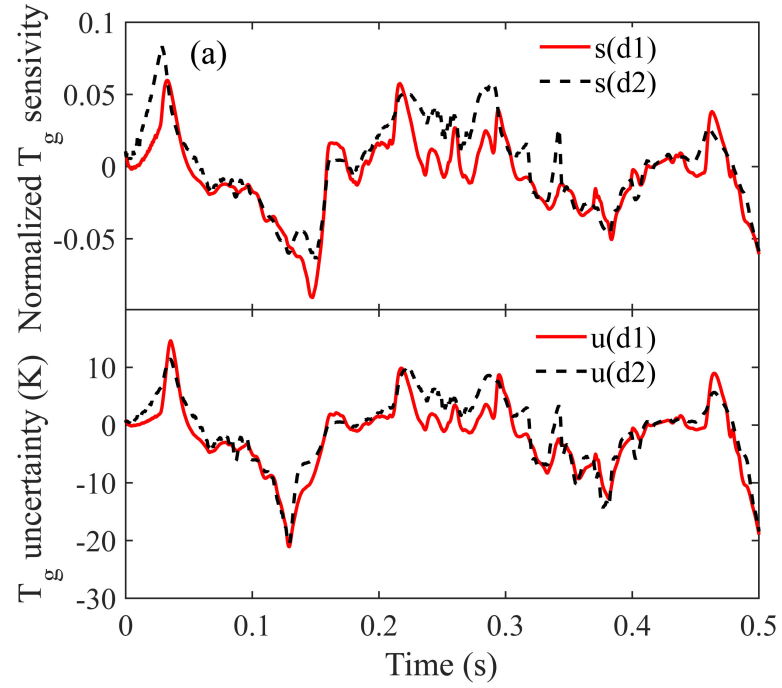

(a)

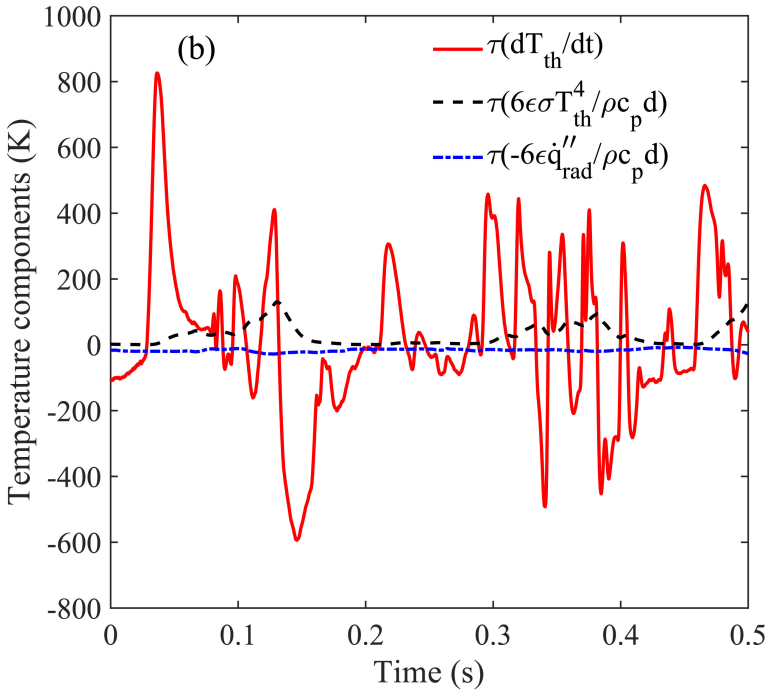

(b)

Figure 2.5: Time-resolved sensitivities and uncertainties on thermocouple bead diameter of dual-TC methods, (b) Time-resolved temperature compensation components on a μm wire diameter TC

2.4 Results

2.4.1 Time dependent gas temperature

Fig. 2.6(a) shows an example of a 1 s duration of compensated temperatures and the corresponding fluctuating time constants along the flame centerline at a height of $2.5D$. Uncompensated temperatures from the 25 μm wire diameter TC, T_{th1} show a higher sensitivity and wider temperature range than the 50 μm wire diameter T_{th2} measurements due to its smaller thermal inertia. Although both T_{th1} and T_{th2} reflect fluctuations in the flow field, details, especially in higher and lower temperature ranges, are missing (T_{th1}: 400 $\sim$ 1770 K, T_{th2}: 620 $\sim$ 1280 K). In comparison, the compensated temperature signals T_{g1} and T_{g2} show good agreement, with a cross-correlation coefficient around 0.99. Compensated temperature fluctuations with a higher frequency resolution show a broader temperature range, from 300 K $\sim$ 2100 K, where the lower and upper limits correspond to the ambient air temperature and flame temperature of ethylene, respectively. The maximum temperature in a turbulent ethylene diffusion flame should be less than the adiabatic flame temperature of ethylene, i.e. 2370 K, primarily due to radiant losses.

For lower height at $1.0D$, the raw and compensated gas temperature is shown in Fig. 2.7(a). Compared to $2.5D$ height, the temperature fluctuation in this height is much smaller, indicating the presence of a laminaried 'necking' region where the mixing between fuel and air in insufficient.

The computed time constants are shown in Fig. 2.6(b) and Fig. 2.7(b).

Both time constant signals fluctuate with changes in the surrounding flow field and follow the same trend. The 25 μm wire thermocouple has a smaller fluctuating time constant, with a mean value of 0.015 s, while for the larger wire diameter the time constant is 6 to 7 times larger.

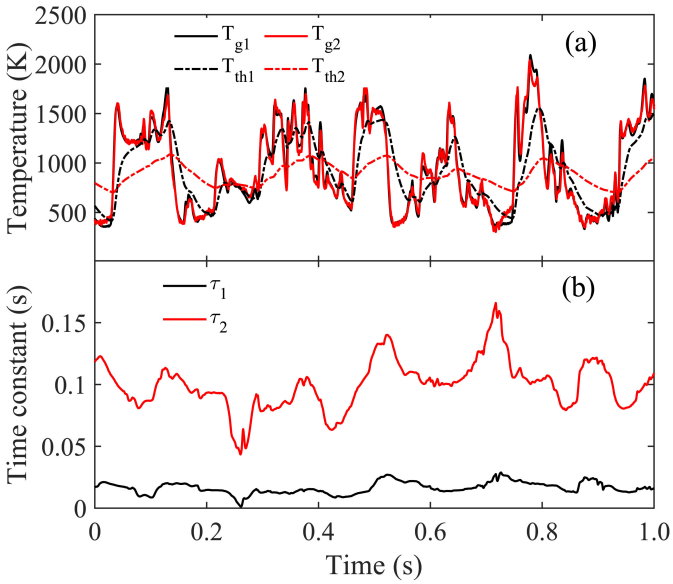

Figure 2.6: Time resolved compensated temperature and time constants at the flame centerline and a height of 2.5D: (a) raw and compensated gas temperature, (b) calculated fluctuating time constants.

2.4.2 Flame centerline temperature

Fig. 2.8(a) shows the mean, rms and ratio between rms and mean temperatures, i.e. the coefficient of variation (CV), along the centerline of the flame. The mean temperature reaches a maximum value at a height of 1.5D, followed by a slight decrease until 2.5D, after which the mean temperature drops due to the end of the flame region; similar results have been reported in the literature [51,62]. The rms temperature fluctuations show a different trend, which increases from a height

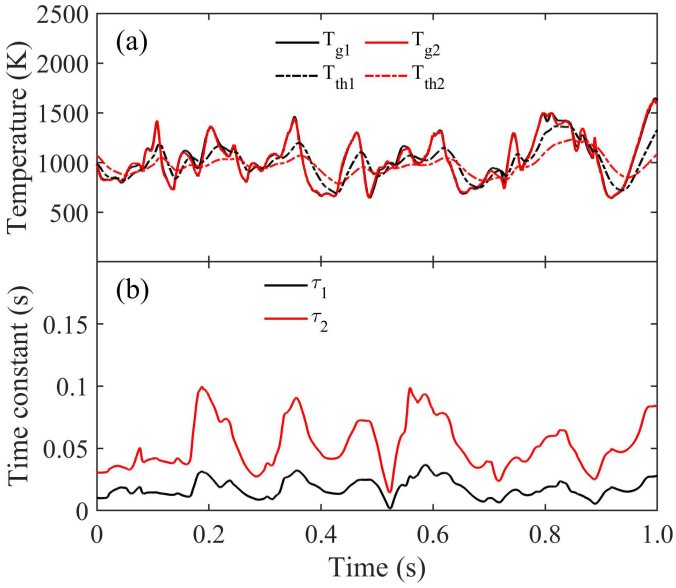

Figure 2.7: Time resolved compensated temperature and time constants at the flame centerline and a height of $1.0D$: (a) raw and compensated gas temperature, (b) calculated fluctuating time constants.

of $1.0D$ with a maximum value at $2.5D$. The CV, $T_{g,rms}/T_{g,mean}$, follows a similar trend with the rms temperature, but with a maximum value at a height of $3.0D$.

Probability density function (PDF) profiles of temperature are presented as a function of height in Fig. 2.8(b). At a height of $1.0D$, the temperature PDF shows a single peak distribution with a temperature value around 1100 K at the maximum probability and a reduced temperature probability under 600 K. This occurs because, at a height of $1.0D$, a narrow necking region is present between intermittent 'puffs' of the flame, as shown in Fig. 2.8(c), where the flame is less turbulent and relatively steady. Insufficient mixing of fuel and air results in less frequency of flame occurrence, and thus a lower mean and rms temperature. As height increases, buoyancy-driven turbulence gradually increases, enhancing mixing between fuel and air. Lower temperatures from 300 K to 600 K are evident in PDF

profiles at heights of $1.5D$ to $2.5D$, meanwhile, PDF profiles shift toward larger values and temperatures higher than 2000 K are detected. This broader temperature distribution leads to a higher rms temperature. At a height of 3.0D, the PDF profile shows a bi-modal distribution, with the upper temperature limits shifting back to a lower value. This is attributed to the combination of fuel burn out and increased air entrainment in this region. For larger heights of 3.5D, the flame is more intermittent and hot burnt gases and air dominate. The PDF profile again shows a single peak distribution with a much lower peak temperature.

2.4.3 Overall temperature statistics

To have a better understanding of the overall flame structure, the mean and rms temperature distributions in a two-dimensional plane across the flame centerline were measured, as shown in Fig. 2.9, where the error bar represents the standard deviation between 2 to 3 repeated measurements. For a height of $1.0D$, a dip in the mean temperature at the flame centerline (r = $0 \sim 1$ cm) is consistently observed. This same trend was also observed by Weckman et al. [16] for methanol pool fires. As discussed before, fuel-rich conditions at this location lead to lower mean and rms temperatures. Away from the centerline, enhanced mixing between fuel and air results in increased mean and rms temperatures. From $1.5D$ to $3.5D$, the mean temperature monotonically decreases moving away from the centerline in the radial direction, with the peak mean temperature near 1200 K. The peak rms temperature fluctuates around $400 \sim 425$ K and is observed 4 cm away from the centerline at

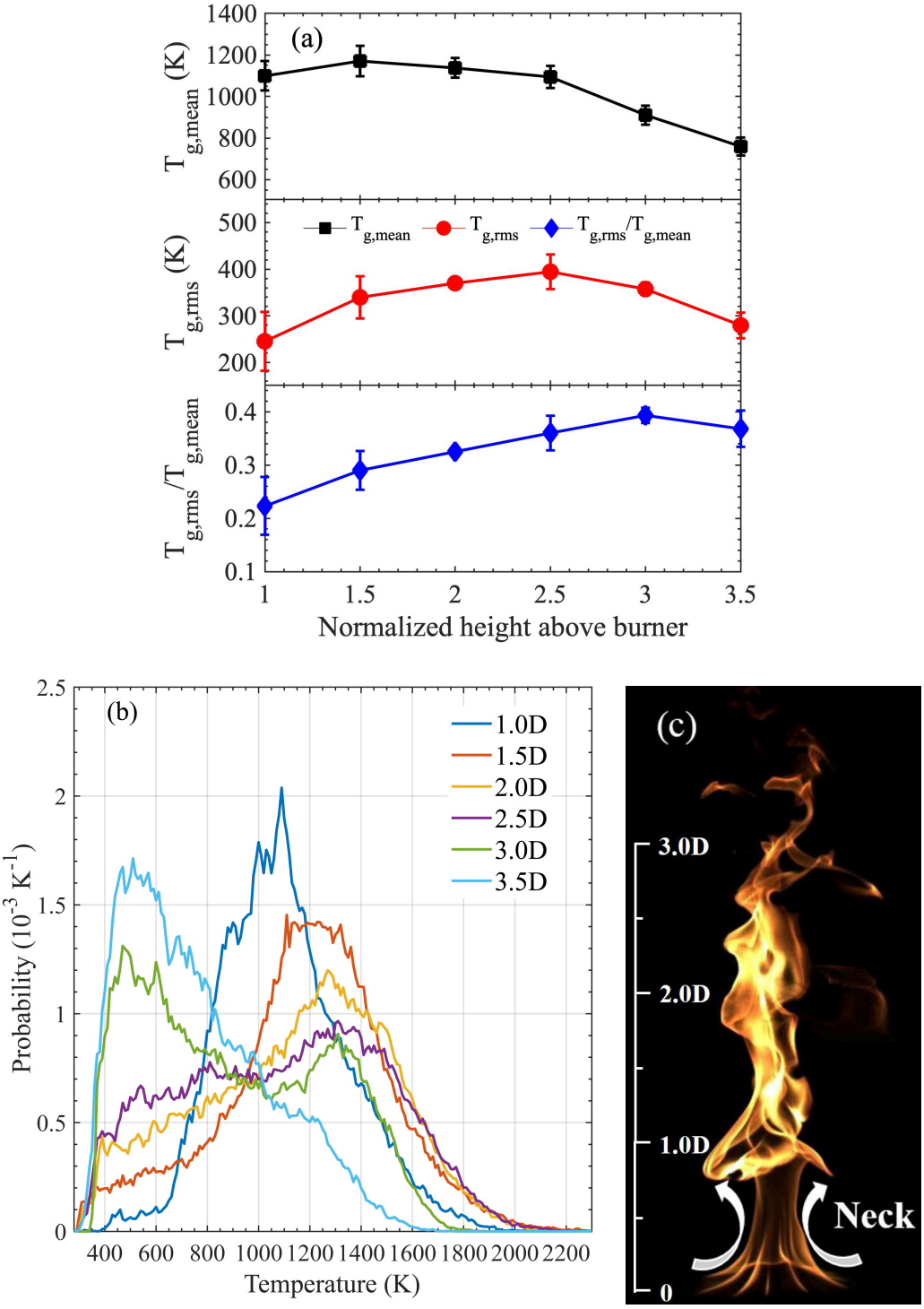

Figure 2.8: Flame centerline temperatures at different heights: (a) mean, rms and ratio of rms and mean temperatures, (b) PDF profiles of temperature, (c) image of the flame. Note the necking of the flame at the base which is responsible for significant mixing and variability at the base.

1.0D. This is consistent with the necking behavior shown in Fig. 2.8(c), where intense mixing occurs in this region away from the flame centerline. As the height increases, the location of the peak rms temperature moves toward the centerline of the flame. After a height of 2.5D, the peak rms temperature is located at the flame centerline.

Temperature PDF profiles in both horizontal (0 to 4 cm) and vertical directions are plotted in Fig. 2.10. At a height of 1.0D, there is a large probability of high temperatures, i.e. $>$ 1200 K, at r = 2 cm, showing good mixing between fuel and air; inward from this location, the environment tends to be fuel rich. For the outward direction, the PDF shifts to a lower value due to increased penetration of ambient air. PDF profiles at a height of 1.5D have a similar trend with those at 1.0D, except the probability of air entrainment into the centerline region increases, promoting better mixing compared to the 1.0D location. From heights of 2.0D to 3.5D, PDF profiles become similar in the radial direction. A relatively homogeneous region is observed and enlarged from 0 $\sim$ 2 cm at a height of 2.0D to 0 $\sim$ 4 cm at 3.0D. The maximum temperature decreases from near 2050 K to 1700 K. After a height of 3.0D, fuel burn out leads to a narrower temperature range and finally results in single peak distribution at 3.5D mainly corresponding to burnt gas. Overall, starting from 1.0D at the flame centerline, mixing between fuel and air is enhanced both horizontally and vertically with a corresponding increase in probability of high temperatures, e.g. the presence of the flame. At the base of the flame, large vortical structures form which oscillate within the necking flame region. As the flame evolves upward, flow instability increases, and vortex structures break down into smaller

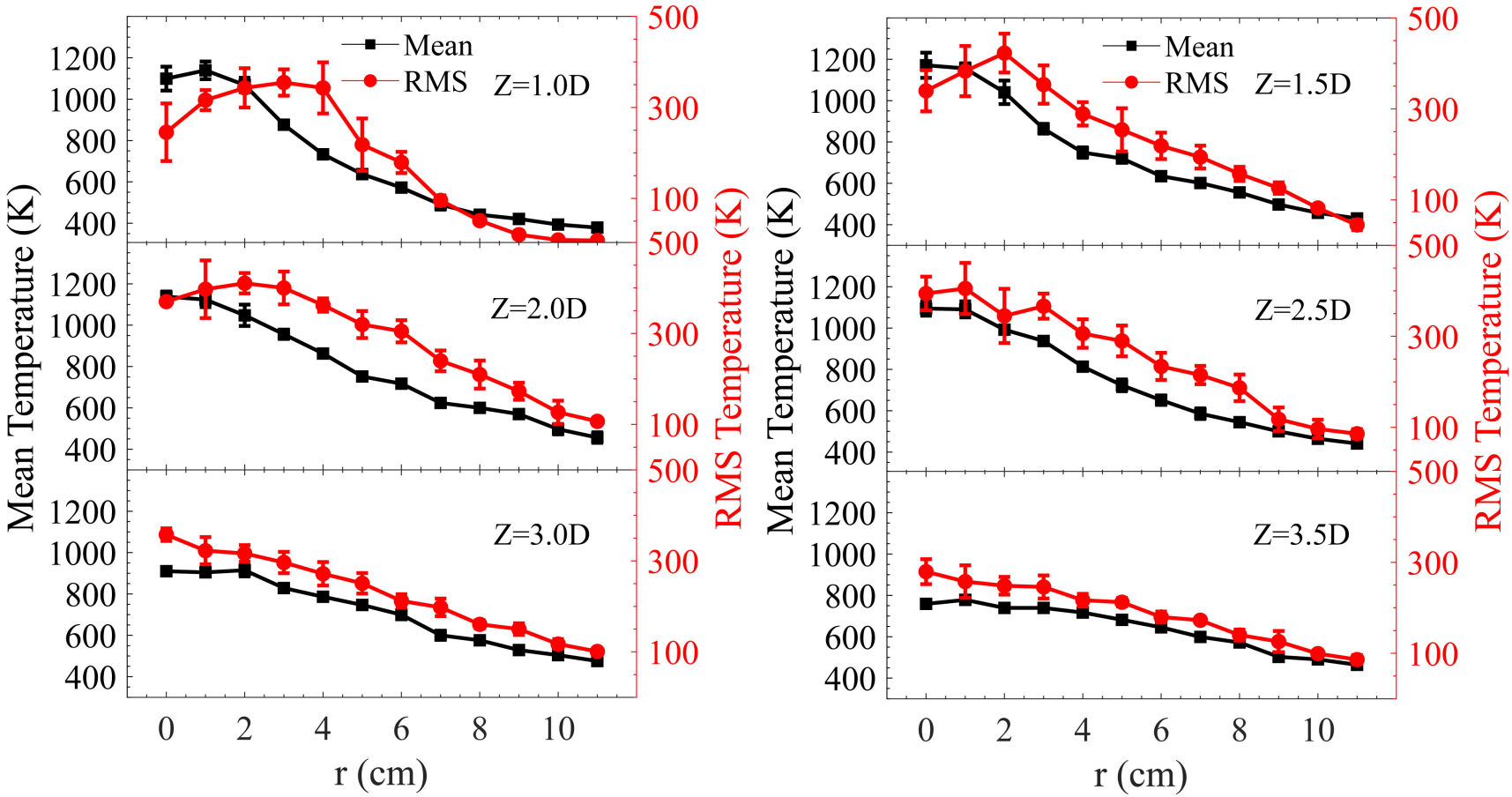

Figure 2.9: Mean and rms temperatures at different heights and radial locations

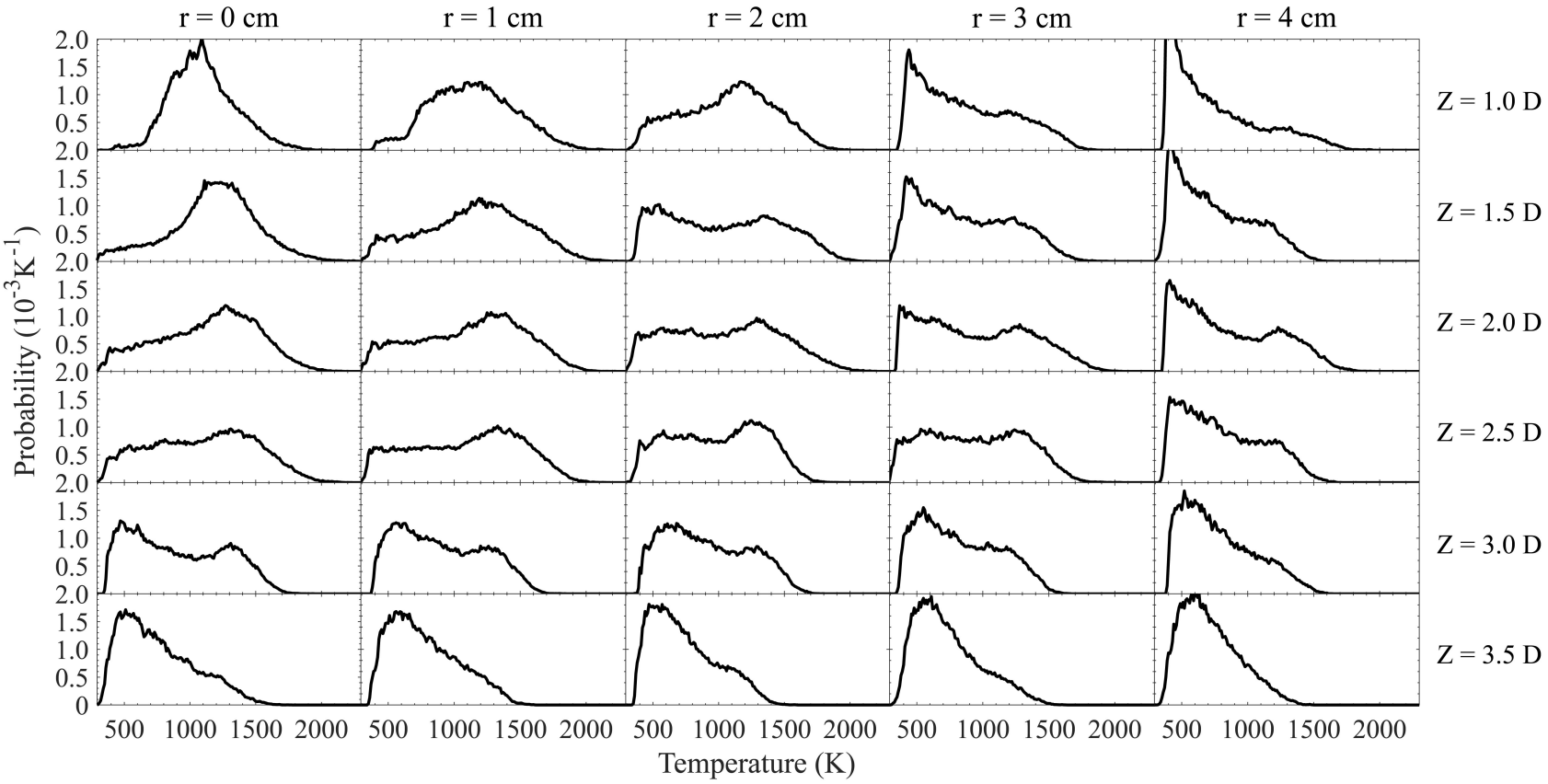

Figure 2.10: Temperature probability distribution at different locations

vortices, promoting mixing between fuel and air and leading to increased mean gas temperatures. Further upward, the combined effects of buoyancy-induced turbulence development and fuel burnout result in homogeneous burning with a reduced mean temperature.

2.5 Ongoing work: understanding soot deposition effects

Following previous observations, the effect of soot deposition on thermocouple measurements was determined to be of importance, especially for highly-sooting low-oxygen flames. A substantial amount of effort was placed in resolving this issue; however, results presented in this section of the thesis are still preliminary and need further examination. Ongoing investigation is being carried out at FM Global and will be incorporated into future publications. Still, these preliminary results will hopefully serve as a stepping stone to better understand the effect of soot on thermocouple measurements in the future.

2.5.1 How soot deposition affects thermocouple measurements

When a thermocouple is inserted into a sooty flame, soot will deposit on the thermocouple bead [63]. The formation of the soot layer affects both the emissivity and the size of the thermocouple bead. Generally, the bead emissivity is found to increase from ~ 0.1 (type-S TC, depends on bead temperature) to 0.95 (soot emissivity) when soot deposition occurs. When the soot layer is thin, the reading of the thermocouple can be corrected using the soot emissivity (0.95). However, when

the amount of soot deposition exceeds a threshold, properties of the thermocouple bead will be significantly affected, including the heat capacity, bead density, and most importantly the thermal conductivity. Under such conditions, the temperature that a thermocouple measures is more close to the coated soot temperature. As a result, the existing temperature correction approach is not applicable.

In order to examine what a soot-coated thermocouple is measuring, we need to re-evaluate the properties of the thermocouple bead. Using a type-S thermocouple as an example, its condition under exposure to a turbulent flame can be expressed using Eq. 2.1. This equation holds true with an intrinsic assumption that the thermocouple bead is thermally thin. However, when soot deposition occurs, such an assumption may not be valid. To examine the validity of this assumption, we used a Biot number, which is defined as

$$\mathrm{Bi} = \frac{hd}{k} \tag{2.16}$$

where h is the heat transfer coefficient between the thermocouple bead and surrounding flow, d is the bead diameter and k the bead thermocouple conductivity. These properties could change significantly following soot deposition. Figure 2.11 shows a diagram of a soot-coated thermocouple bead (25 μm wire diameter, 75 μm bead diameter). The majority of the metal bead is made of platinum (a blend of platinum -90%/rhodium-10% alloy and pure platinum), thus having a thermal conductivity of platinum which ranges from 71.8 to 80.8 W/m-K when the temperature increases from 300 to 725 K [64]. However, the thermal conductivity of the soot

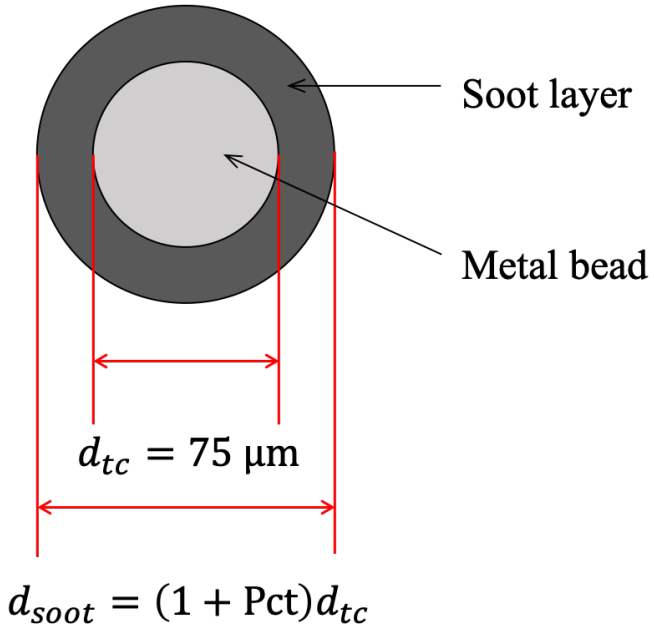

Figure 2.11: Thermocouple bead with soot layer.

layer can be as low as 0.047 W/m-K [65], which acts as an insulation layer.

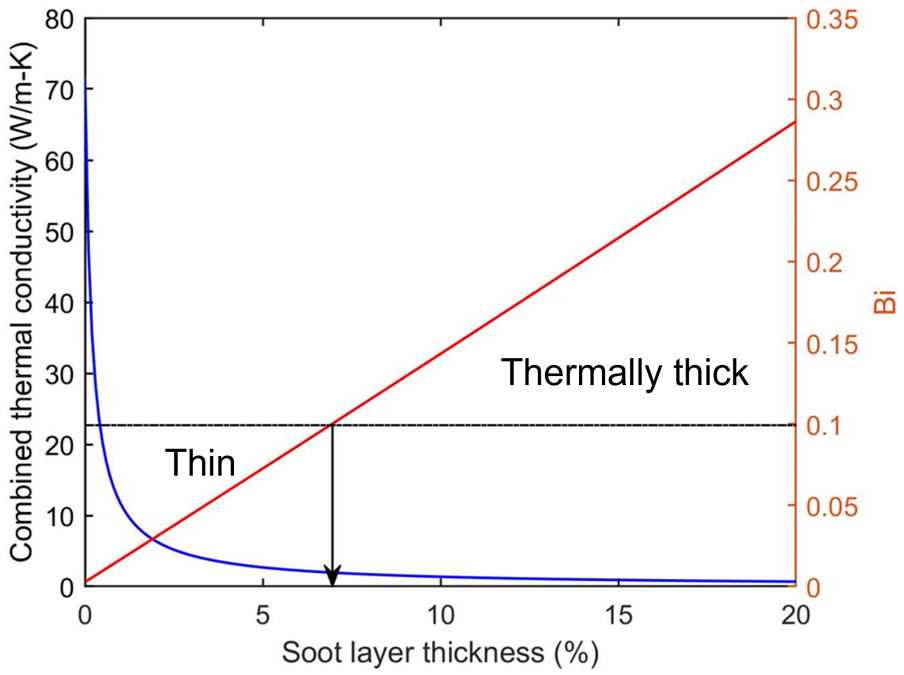

Figure 2.12: Lumped thermal conductivity and Biot number vs. soot layer thickness.

To evaluate the Bi of the soot-coated thermocouple, a lumped thermocouple conductivity was calculated, as displayed in Fig. 2.12. When Bi < 0.1 [66], the

thermocouple bead is thermally thin, thus having a uniform temperature even under turbulent flame conditions. While for Bi > 0.1, the thermocouple bead is thermally thick. A temperature gradient is therefore likely to exist within the bead, meaning that the soot layer and metal bead have different temperatures. For a 75 μm diameter bead, a $\sim 7\%$ thickness soot layer is found to segregate the thermally thin and thick regimes. Such results indicate that soot deposition has to be minimized when using thermocouples. This further requires a thorough understanding of the soot deposition/oxidization process.

2.5.2 Exploring the soot deposition and oxidization process

To examine the soot deposition/oxidization process, a series of laminar flame tests were first conducted. A laminar ethylene diffusion flame was established on a Santoro-type burner [67] with a circular fuel tube of 16.4 mm inner diameter (17.6 mm outer diameter). The fuel tube was surrounded by an air (or air-N_2 mixture) co-flow passing through a 10 $\times$ 10 cm^2 flow straightener with 5 cm thick metal beads (1 mm outer diameter) sandwiched between two layers of wire-mesh screens. Ethylene with a 0.28 standard liters per minute (SLPM) flow rate and 65 SLPM of air flow were fed to the fuel tube and co-flow exit, respectively. Three oxygen concentrations, 20.9%, 16.8% and 15.2% were tested.

To explore how soot deposits on the thermocouple bead, a 25 μm wire diameter (75 $\sim$ 80 μm wire diameter) type-S thermocouple was carefully traversed across the diffusion flame sheet. The thermocouple was configured as a 'Y' shape (see Fig.2.13)

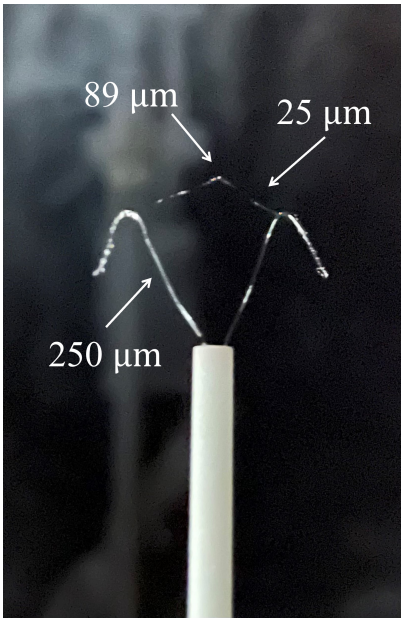

Figure 2.13: A 'Y' shape type-S thermocouple

with the 25 μm wire diameter probe supported by 250 μm diameter prongs of materials identical to those of the thermocouple wires. Such a design reduced the measurement disturbance to the flame structure as well as the heat losses to (or heat gain from) the ceramic tube. When moving across the reacting flame zone, the bead of the thermocouple passes a soot-free fuel lean region and sooty fuel rich region, as illustrated in Fig. 2.14. It is likely that the soot accumulates in the sooty fuel rich side but is oxidized in the fuel-lean side. However, the hostile high-temperature environment prohibits the precise measurement of soot deposition and oxidization rates. Instead, we evaluated such process using the temperature history of the thermocouple bead.

Figure 2.15 displays the thermocouple bead temperature when it was inserted into the flame centerline (30 mm height above burner) and extracted out to ambient air. The dwell time of the thermocouple bead at the flame centerline was 3 s.

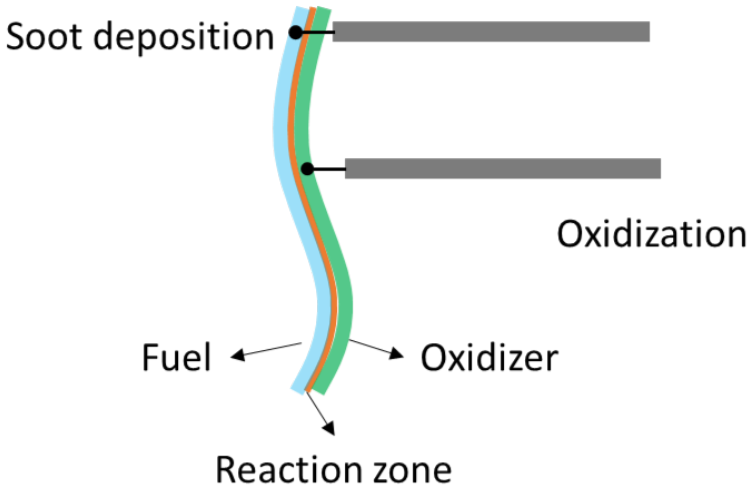

Figure 2.14: A type-S thermocouple placed near the ethylene diffusion flame sheet.

The first peak represents the bead temperature when it passed across the reacting flame sheet with a clean surface. After the first peak, at t_1 time, the thermocouple bead was positioned at the flame centerline and stayed for 3 s. It is observed that the bead temperature decreased during this period. Initially, from t_1 to t_2, a non-linear temperature decrease occured due to the increasing bead emissivity caused by the soot deposition, and thus contributed to higher radiation losses and a lower temperature. At t_2, the bead emissivity was nearly equal to the soot emissivity. A linear temperature decrease was observed from t_2 to t_3, which is attributed to the increasing bead size due to soot deposition. Similar results have also been reported in the literature [63,68]. After t_3, when the thermocouple bead passed across the fuel lean zone, soot was oxidized. This is further confirmed by repeating the insertion and extraction process, as displayed in Fig. 2.16. The higher peaks of the temperature profile maintained the same value, indicating that the thermocouple had a clean surface between each test. In summary, the deposited soot on the bead surface was

oxidized when the bead passed through the fuel lean region of the flame sheet.

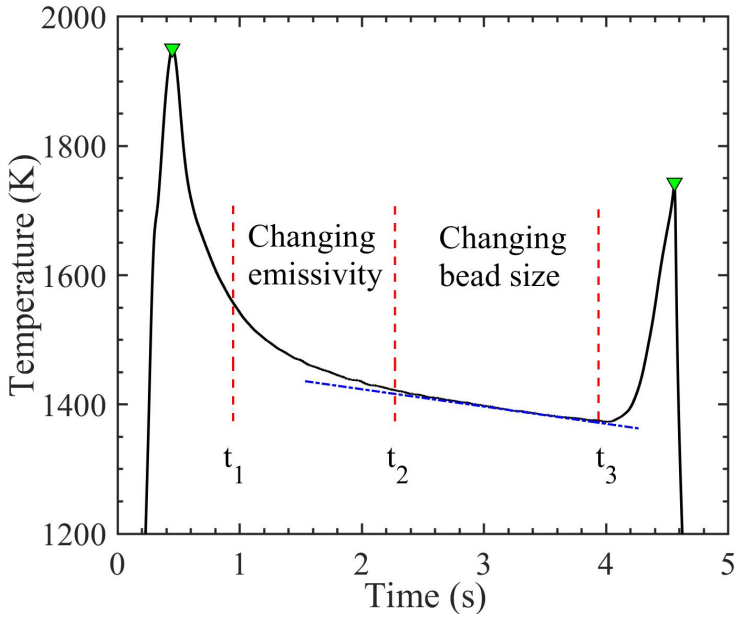

Figure 2.15: Temperature history of the thermocouple bead moving into and out of the flame centerline at 30 mm height above the burner.

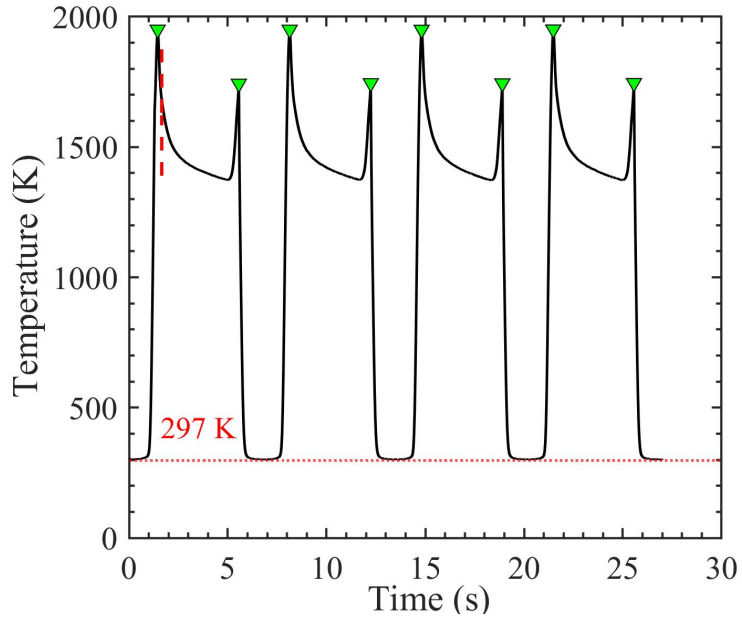

Figure 2.16: Temperature history of the thermocouple bead which is repeatedly moving into and out of the flame centerline at 30 mm height above the burner.

2.5.3 Turbulent flame condition

As discussed in section 2.5.1, soot deposition has to remain less than a threshold to maintain a thermally thin assumption for thermocouple measurements. Otherwise, temperature compensation for turbulent flame conditions will be impossible due to contaminated raw data. The above findings indicate that the 'Y' shaped thermocouple is a better configuration to reduce the soot accumulation, which could be used for turbulent flame measurements. Under turbulent flame conditions, the reacting flame sheets frequently sweep through the thermocouple bead with a relatively fast speed, resulting in a repeated process of soot deposition and oxidization. If we can assure that soot accumulation during each test is below a threshold, the turbulent flame temperature can be properly compensated. Therefore, future experiments under turbulent flame and reduced oxygen conditions are needed.

2.6 Conclusions

A dual-thermocouple technique has been applied to a carefully-instrumented turbulent ethylene diffusion flame in order to provide accurate gas temperature measurements. Both sensitivity and uncertainty analyses show that this improved dual-TC technique has advantages under hostile flame environments where the bead diameter may change due to soot deposition or other effects. Measured temperatures were compensated using a temporally-varying time constant, producing a systematic temperature validation dataset for 15 kW buoyant turbulent ethylene flames useful for future model development and validation. The resultant mean, rms and PDF

temperature profiles provide a detailed picture of the turbulent flame structure.

These temperature measurements, alongside existing data such as the radiant power distribution, local soot volume fraction and soot temperature, as well as future gas velocity measurements will provide a detailed dataset of this flame for validation and development of radiation models.

Chapter 3: Wind-driven flame experiment

3.1 Introduction

Coherent flame structures have been observed over a wide range of scales, ranging from saw toothed structures in large-scale wind-driven wildland fires (see Fig. 3.1 and Finney et al. [26]) to coherent streamwise streaks in bench-scale boundary-layer flame experiments [26, 31, 32]. Experiments at smaller scales have shown how coherent structures in laminar flames can modify heat transfer from flames to downstream surfaces, by redistributing hot combustion gases [31, 32]. Large-scale studies on spreading fires have identified the production of intermittent high-temperature fluctuations ahead of spreading flame fronts [26], presumed to occur due to the formation of counter-rotating vortices [69]. Contrary to previous two-dimensional assumptions [27, 70], these findings affirmed the three-dimensional nature of many boundary-layer flames [34]. Therefore, resolving these three-dimensional structures becomes crucial for the prediction of flame spread in many applied fire scenarios and for the fundamental study of flames, which uses computational fluid dynamic (CFD) simulations. Within flame structures such as streaks and troughs, velocity measurements remain extremely challenging, whereas the light emitted from the sooty flame serves as an effective tool to visualize these structures [71]. This en-

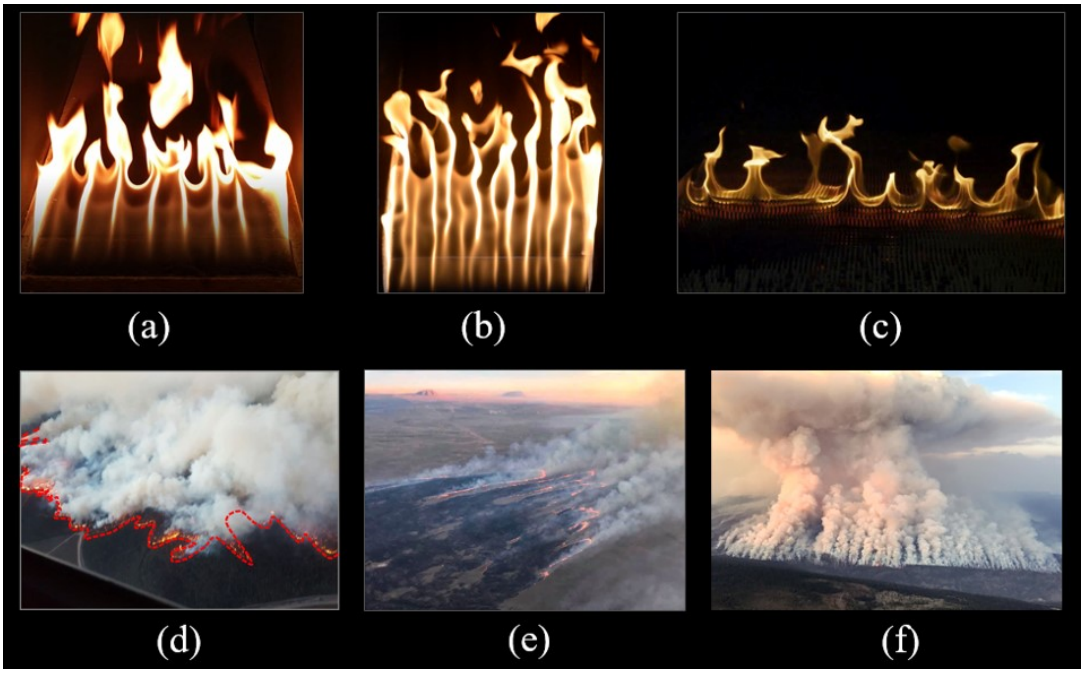

Figure 3.1: Coherent structures in the form of streamwise streaks emanating from the leading edge of wind-blown flames are clearly visible over a wide range of scales. (a) Top-view of a propane flame under combined inclination and forced flow [73], (b) top-view of a propane burner in crossflow with a high freestream turbulence intensity, (c) front view of a propagating flame over a cardboard tine fuel bed (Missoula Fire Sciences Laboratory), (d) a saw-toothed fire front (red dashed line) spreading across the Kynsna area (source: South African Red Cross), (e) aerial view of the Sheep Fire northwest of Idaho Falls (credit: Idaho National Laboratory), (f) aerial view of smoke from the 2017 Elephant Hill wildfire, British Columbia, Canada (credit: BC Wildfire Service).

ables the characterization of their length and time scales, e.g., the spacing between streaks (i.e., wavelength of the flame front) and time of persistence for local streaks. Such parameters can be of practical use to predict the growth of coherent flame structures, to understand intermittent flame motions, and to perform scaling analysis of the flame [72]. However, a systematic investigation of these parameters, in particular their relationship with the disturbance in turbulent incoming flows, has not been conducted.

Streamwise flame streaks and troughs (also known as “towers and troughs”

or "crests and troughs") are two distinct structures, which have been observed in three-dimensional boundary-layer flames [26, 31, 32]. Much like their formation, the structure's growth is thought to be closely coupled with pre-existing flow disturbances, scaling with the boundary-layer thickness of the incoming flow and buoyancy from flame-derived heat release. Miller et al. [31] investigated coherent flame structures, using a stable laminar boundary-layer flame, finding that the flame streaks (e.g. streak spacing) are controlled by pre-existing structures in the cold flow. At the same time, the streamwise growth of the downstream streak height within the flame is affected by buoyancy, following Rayleigh–Taylor instability scaling [74]. In a later work [32], they measured the spacing between neighboring streaks, finding that the initial streak spacing is proportional to the incoming boundary-layer thickness. However, these findings were limited to stable laminar flames. Turbulent boundary-layer diffusion flames differ from these laminar configurations, mostly due to the complicated instabilities within the flow [75, 76]. Finney et al. [26] examined the separation between flame towers (e.g. streak spacing) of spreading turbulent boundary-layer flames, finding that the separation distance is linearly related to the flame length. Similarly, Frangieh et al. [77] simulated a three-dimensional propagating turbulent flame front formed over a homogeneous solid-fuel layer, finding that the streak spacing scales with the 2/3 power of fire intensity. This fire intensity was also found to be linearly related to the incoming flow velocity. However, the turbulent disturbances of the flow, arising naturally, were found to couple with a buoyancy-induced instability, thus being difficult to separate and quantify. Zhou et al. [78, 79] quantitively examined the effects of freestream turbulence on the burning

of Polymethyl methacrylate (PMMA) in a wind tunnel, where freestream turbulence with a controllable intensity can be produced by a perforated grid upstream of the tunnel. They found that the mass burning rate of the PMMA increased at high turbulence intensity due to enhanced convective heat transfer. Recently, Singh et al. [80] examined the burning behavior of mixed-convection wind-driven flames under varying freestream conditions, defining a unified mixed-convection parameter $\xi = \mathrm{Gr}/\psi^3$ for both laminar and turbulent boundary layer flames, where ψ represents the momentum force with freestream turbulence accounted. However, no information about the coherent flame structures was reported.

In non-reactive boundary-layer flows, the influence of flow turbulence on streamwise streaky structures has been extensively examined [81–84]. It has been found that coherent streaky structures, denoted as Klebanoff modes [81], are often induced by low levels of freestream turbulence. Matsubara and Alfredsson [82] visualized streamwise streaks in a boundary-layer flow, which was subjected to 1% to 6% freestream turbulence, finding a larger streak spacing at higher turbulence intensities. Furthermore, a numerical study by Brandt et al. [83] showed that amplification of a streak led to transition from a linear to non-linear mode when the intensity of freestream turbulence was larger than 3%. Recently, Farrell and Ioannou [84] have demonstrated that a sufficiently high freestream turbulence intensity can lead to a self-sustaining state. Under this state, the turbulent system is maintained by the non-normal parametric growth, which arises from the interaction between a time-dependent streak and the perturbation. These studies indicate a positive relationship between the growth of streamwise streaks and the incoming flow turbulence

intensity.

Given the fact that streaky structures are a well-known instability that form in near-wall flows as they transition to turbulence, it is reasonable to expect similar structures in reacting boundary-layers. These features are also known to be influenced by freestream turbulence. What is also important for a fire problem, e.g., wildland fires, is that the changing of the global thermal structures, such as the overall flame attachment length, and the flame heat flux to the surface where fuel usually sits beneath. The flame attachment length [85–89] (also known as flame drag/extension length) is an important length scale because it represents the region over which the flame directly impinges on the combustible material. As a result, fuel pyrolysis/gasification takes place within this region. The magnitude of the heat flux further determines the rate of pyrolysis/gasification and eventually affects the spread rate of the flame [66, 90–92]. Freestream turbulence appears to affect these parameters through destabilization of the streaks and a transition to turbulence in the boundary layer, but a fundamental understanding of their relationships is still missing.

Numerical modeling of the laminar to turbulence transition for near wall flames also remains a challenge. Often times, a trip mechanism, e.g., a small metric bar, is employed to promote transition to turbulence in relatively small-scale flame simulations [35, 93]. However, the effect of the trip mechanism can be hard to quantify. Freestream turbulence provides a means to achieve a similar effect with a quantifiable turbulence intensity, facilitating the development of validation datasets for numerical models.

3.2 Experimental methods

3.2.1 Wind tunnel

A specially-designed wind tunnel was used to generate both laminar and turbulent flows in all experimental tests, as displayed in Fig. 3.3. A controllable centrifugal blower was employed to pressurize a large plenum which then passed through a reducer into a 115 cm long straight section with a 30.48 $\times$ 30.48 cm cross-section. By controlling the output of the blower with a pulse width modulation controller, wind velocity could be adjusted from 0.5 to 6.0 m/s. Four velocities, 0.99, 1.48, 2.01, and 2.43 m/s were selected in this study. To maintain uniform laminar flows, screens consisting of a 0.033-mm wire mesh, a 6:1 honeycomb, another 0.033-mm wire mesh, and a 0.017-mm mesh were placed 80 cm upstream of the tunnel exit. The honeycomb was employed to dampen swirl and lateral velocity variations within the flow, while the wire mesh screens were used to reduce turbulence by breaking up large-scale turbulent eddies [94]. As a result, low levels of turbulence, on the order of 0.5 - 0.8%, were achieved for all tested velocities at the tunnel exit. Conversely, to generate freestream turbulence, an additional staggered perforated grid (see Fig. 3.2 was added 10 cm upstream of the tunnel exit. This method, proving both simple and repeatable, has been widely used to generate nearly homogeneous turbulence in wind tunnel studies [95]. Through varying the hole diameter (d) and center-to-center distance of the grid (h), turbulence intensities of the flow can be

adjusted, which is defined as

$$\mathrm{TI} = u'_{rms}/U, \tag{3.1}$$

where u'_{rms} is the root-mean square of the velocity fluctuations and U is the mean flow velocity. u'_{rms} is calculated as

$$u'_{rms} = \sqrt{\frac{1}{N}\sum_{i=1}^{N}(u_i - U)^2} \tag{3.2}$$

where u_i is the velocity at time i and N the total number of data points.

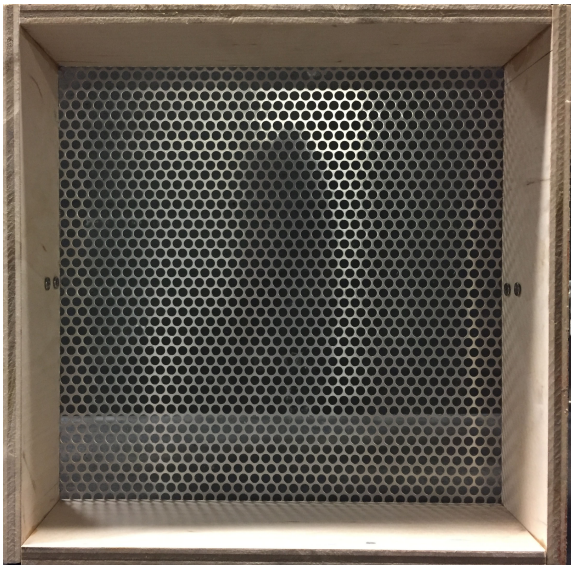

Figure 3.2: Perforated grid 1

In order to test flow uniformity, the wind tunnel exit was fully characterized with a hot wire anemometer. Nearly homogeneous turbulence was measured across the vast majority of the tunnel exit at grid 1, grid 2 and grid 3 conditions.Turbulence intensity of the flow was adjusted through varying the solidity ratio of the grid, α, hich is calculated as

$$\alpha = 1 - \pi d^2/4h^2 sin60^\circ \tag{3.3}$$

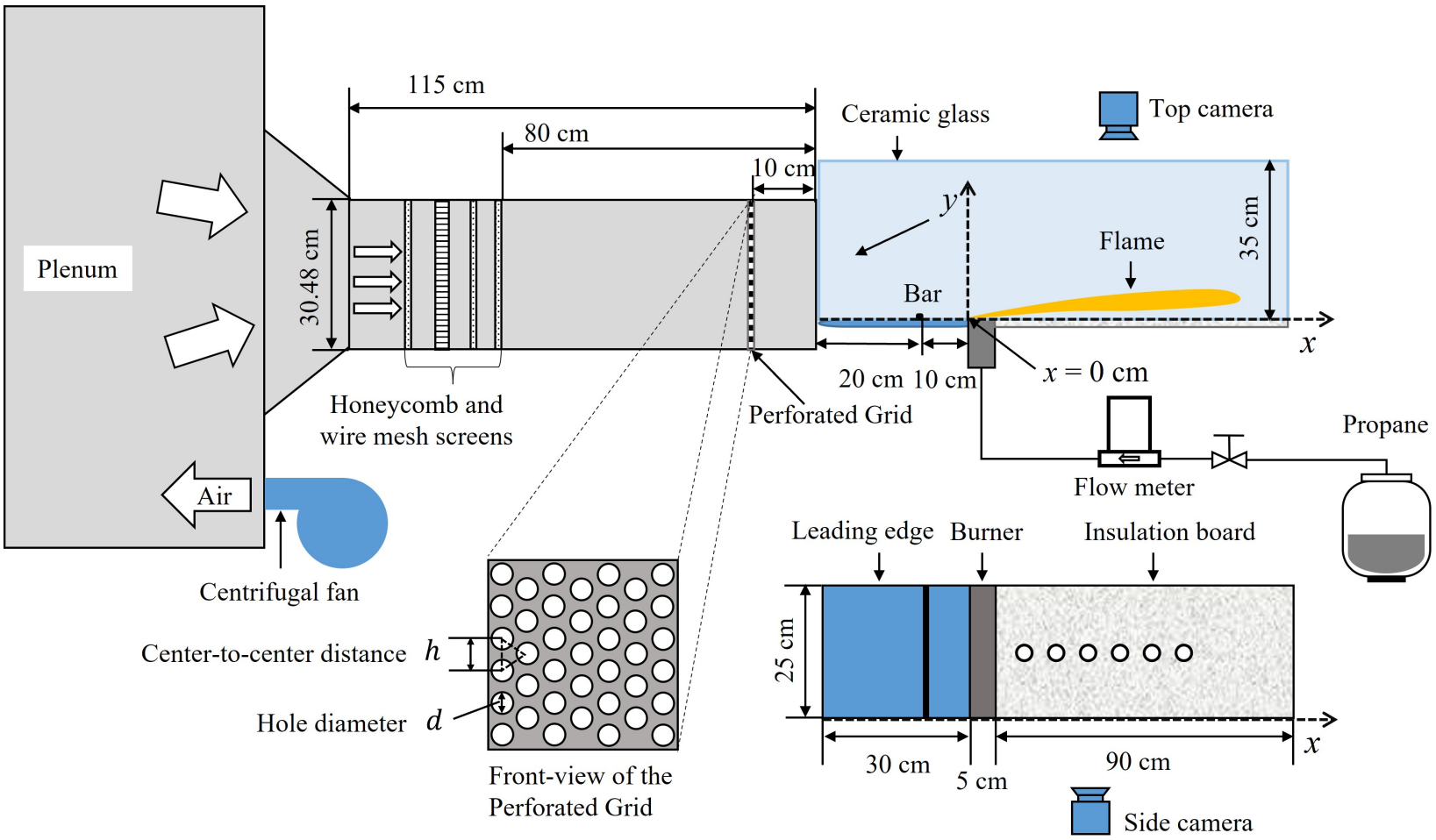

Figure 3.3: Schematic of wind tunnel and experimental setup

where d is the hole diameter, and h is the center-to-center distance (see Fig. 3.3). Detailed information of the grid sizes and flow turbulence intensities is listed in Table 3.1. It is noted that a 2.43 m/s flow velocity was unable to be achieved at the grid 3 condition due to the high backpressure caused by the high solidity ratio of the grid. For comparison, an additional 'bar' test was carried out, where an aluminum bar, 1.5 cm wide with a 0.5 cm by 25 cm cross area was placed 20 cm downstream of the tunnel exit. This bar perturbs the laminar boundary layer to turbulent by creating a reversed flow regime.

Table 3.1: Perforated grid sizes and corresponding turbulence intensities (TIs).

Grid	Hole diameter d [mm]	Center-to-center distance, h [mm]	Solidity ratio, α	Wind velocity (m/s) 0.99	1.48	2.01	2.43
No Grid	–	–	–	0.8%	0.5%	0.5%	0.8%
Grid 1	6.4	8.0	0.42	4.1%	2.5%	2.1%	2.2%
Grid 2	1.6	3.2	0.77	8.3%	8.6%	8.6%	8.1%
Grid 3	1.6	4.8	0.91	16.8%	15.3%	14.9%	–

Note: Solidity ratio is calculated as ratio of effective solid area to enclosed area of the perforated grid.

The remainder of the experimental configuration, displayed in Fig. 3.3, was placed at the exit of the wind tunnel. A 6.4-mm-thick aluminum plate of length 30 cm with a super elliptical 8:1 aspect ratio leading edge was positioned nearly adjacent to the wind tunnel exit. This design helps to minimize boundary layer separation and bluff body effects [96,97], which could introduce unwanted flow turbulence by disturbing the development of the boundary layer or creating a recirculation zone. The boundary layer development length was dictated by the length of the alu-

minum plate. Immediately following this plate, a propane sand burner was placed, with its surface held flush to the lip of the aluminum. The 8-cm-deep burner was made with 3-mm-thick stainless steel with a 25×5 cm cross-sectional opening to the ambient. Chemically pure propane (>99.0%) was fed through a mass flow controller to the bottom of the burner, distributed within a 2-cm-tall plenum. Before reaching the burner surface, fuel passed through a metal honeycomb and mesh screen followed by a 6 cm depth of multi-purpose sand (diameter range: 0.1 – 0.5 mm) to assure a uniform exit velocity. Stationary fires of 5, 7.5, and 10 kW heat release rates (HRR) were produced by setting the propane flow rates to 0.10 g/s, 0.15 g/s and 0.20 g/s, respectively. Beyond the burner, a 90-cm long insulation board (1.27-cm-thick alkaline earth silicate wool) was placed and kept flush with the burner edge to maintain a horizontal surface over which the flame would develop. Two 35-cm-tall ceramic glass sheets of 125 cm length were placed on both sides of the test apparatus to minimize the effects of side entrainment.

3.2.2 Velocity measurement

Velocity measurements of the cold-flow were made using a miniature single hot-wire probe (55P16, 5 μm diameter and 1.25 mm length) oriented normal to the flow direction. This probe was coupled to a Dantec Dynamics constant-temperature anemometry (CTA) system. The CTA system outputs voltage signal directly, therefore, a calibration function is needed to convert the voltage reading to velocity data. The hot-wire probe was calibrated in a 17-mm diameter (see Fig. 3.4) free-jet style

Figure 3.4: 17 mm free-jet style rig and the model 6542 OMNI probe

rig against a pre-calibrated Kanomax Climomaster handheld hot-wire anemometer with a 0.01 m/s resolution (Model 6501, with a model 6542 OMNI probe). Flow of the rig was supplied by a flow controller, which produced an exit velocity ranging from 0 to 4 m/s. The accuracy of the handheld hot-wire anemometer was further verified against volumetric flow rate measurements using a Dantec calibration unit, as shown in Fig. 3.5. Voltage data from the CTA was acquired using a LabVIEW program at a sampling rate of 50 kHz. Three independent tests were performed at each calibration point at a given flow velocity. Finally, a 6^{th}-order polynomial calibration function was obtained to convert the voltage of the CTA to velocity. For all velocity measurements recorded at a given spatial position, data was collected for a duration of 60 s at 50 kHz.

The instantaneous response of the hot wire to the flow velocity can be written

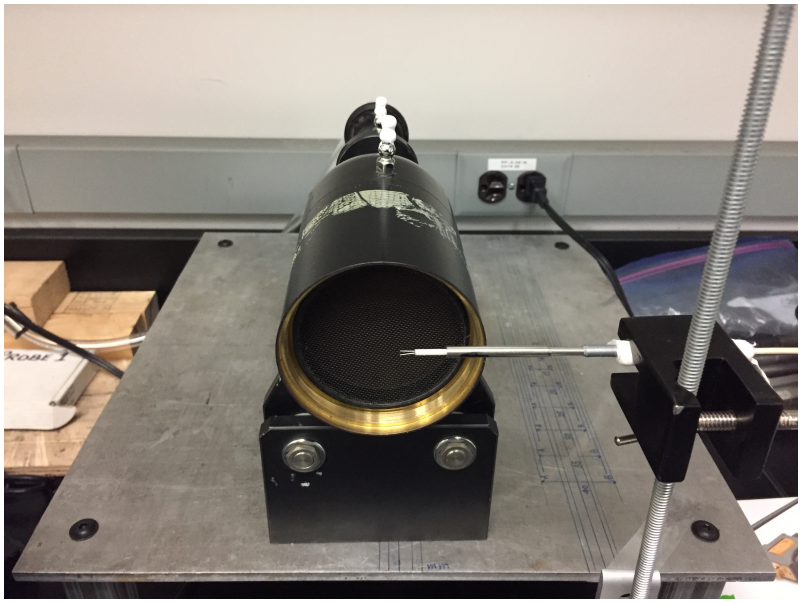

(a)

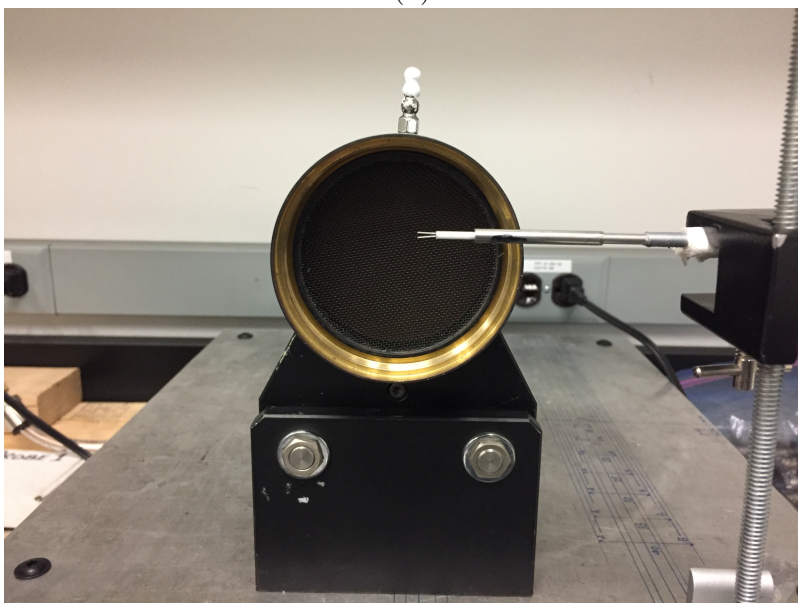

(b)

Figure 3.5: Dantec calibration unit (a) overview and (b) front view

as Eq. 3.4

$$E^2 = A + B(U)^n \tag{3.4}$$

where A and B are constants from the calibration. Eq. 3.4 is known as King's law [98]. Fig. 3.6 shows that the hot-wire voltage output fits the King's law well

in general. However, for lower velocities, deviation is observed, as shown in Fig. 3.6(a). Given the consideration that the current work focuses on low speed flow, a 6 order polynomial fit was used to covert the hot-wire voltage output to velocity, as shown in Fig. 3.6(b). A maximum velocity of 4 m/s was used since the average flow velocity in this dissertation ranges from 0 to 2.5 m/s. The 50 kHz sampling rate enables us to obtain the integral information of the flow turbulence, including the integral time and integral length, which are used to calculate the Taylor microscope Reynolds number of the incoming flow.

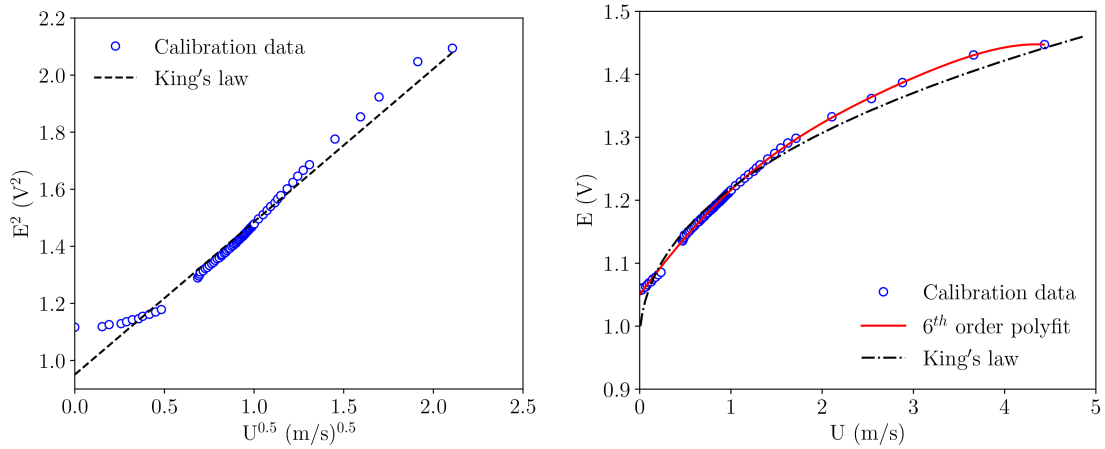

(a) (b)

Figure 3.6: King's law

3.2.3 Heat flux measurement

Flame to surface heat flux is an important parameter since it controls the heat transfer between the flame sheet and combustible surface. The magnitude of the heat flux further determines the rate of pyrolysis/gasification and eventually affects the spread rate of the flame [66, 90–92]. For wind driven flame, the flame

to surface heat flux is measured by Hukseflux water-cooled total heat flux gauges (model SBG01, see Fig. 3.7), which was calibrated against a reference heat flux sensor (the reference sensor is calibrated according to NIST standard) under a cone calorimeter at UMD's fire lab. The calibration curve is shown in Fig. 3.8. The voltage response of the heat flux gauge is linearly related to the received heat flux. The flame to surface heat flux was measured at 50 Hz. Before each test, the heat flux gauges were calibrated against a standard reference heat flux gauge in a cone calorimeter. The heat flux gauges were placed 6 cm downstream of the burner at 6 cm intervals. Each case has been repeated six times to ensure the repeatability of the measured results.

Figure 3.7: Hukseflux water-cooled total heat flux gauge (HFG)

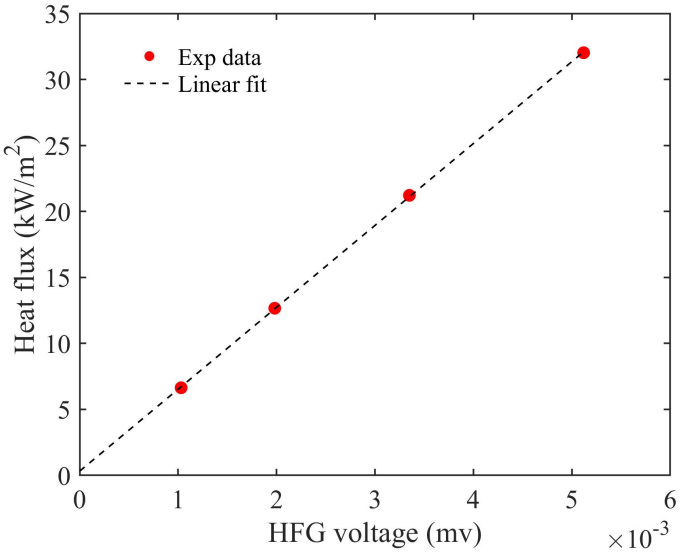

Figure 3.8: Calibration curve for Hukseflux total HFG

3.3 Image processing technique

The flame structures, including the flame attachment and flame streaks were analyzed using image analysis technique. Two cameras, a high-speed Sony digital camera (RX10 II) and a Nikon digital SLR camera (D7100), were employed to acquire flame videos. The Sony was placed at $\sim$ 1.5 m height above the wind tunnel exit to capture the movement of coherent flame structures from a top view at 240 frames per second (FPS). The video was recorded in 1824 $\times$ 1026 pixels and further cropped to 1080 $\times$ 608 pixels so that only the flaming region was retained. The Nikon was placed on one side of the test apparatus ($\sim$0.5 m away from the side wall) to record the side view of the flame at 60 FPS in 1080 $\times$ 720 pixels. Diagonal fields of view of the Sony and Nikon cameras were around 63° and 76°, respectively. The obtained images and videos were processed in MATLAB to extract the geometric information of flame structure.

Flame streaks with a 0.99 m/s flow velocity and a 16.8% TI, displayed in Fig. 3.9a, were tracked using a peak detection algorithm by examining the luminosity profile of the top-view flame video. Figure 3.9b shows the local luminous intensity profile extracted at $x = 8$ cm from Fig. 3.9a. Using this method, the location of the flame streak at a certain downstream distance was mapped as a function of time (2-s time duration, totaling 480 frames). The space between neighboring streaks was measured as streak spacing, l. The path of the streak was recorded by continuously mapping the peak locations of a streak at different time steps (frames). Meanwhile, the width of a flame streak was tracked by finding the minimal values on the left and right sides of the local peak. The left boundary of the streak is defined as the middle location between the left minimum and the peak. Similarly, the right boundary of the streak is defined as the middle location between the right minimum and the peak. The distance between the left and right boundaries of the streak was obtained and defined as the streak width, as shown in Figs. 3.9 and 3.10. The maximum movement of a continuous streak between frames was defined at 85% of its width. Life of a streak ends once its movement exceeds 85% of its width. A detailed description of the detection method can be found in Ref. [32].

When subject to high momentum cross flow, flame is attached to the surface of the ground, resulting in a long extension region. The length of this attached region is defined as the flame attachment length. Side-view videos (60 s recorded at 60 FPS) were used to determine the attachment length of the flame. Each frame of video was firstly converted to a black-white (BW) binary image as shown in Figs. 3.11(a-b), then 3600 BW images were averaged to get the flame appearance

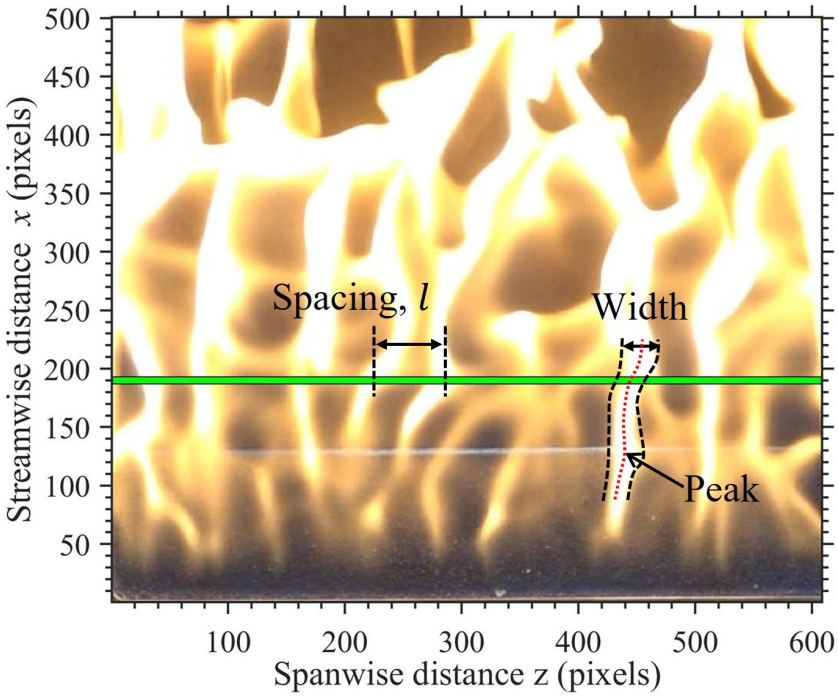

(a)

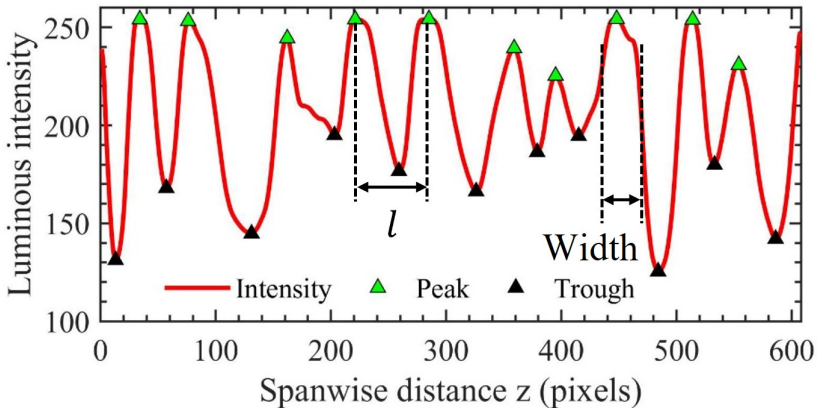

(b)

Figure 3.9: Flame streak detection: (a) top-view of the propane boundary-layer flame at $U = 0.99$ m/s and TI = 16.8%. The thin green slit represents the analysis region at $x = 8$ cm. (b) Smoothed luminous intensity profile of the analysis region, black triangles mark the detected trough location, green triangles mark the detected streak location and the space between neighboring peaks, determined as the streak spacing (l).

probability, shown in Fig. 3.11(c). Finally, a 50% appearance probability was used to determine the mean flame geometry, which is represented by the red dash line in Fig. 3.11(d). The distance between the burner trailing edge to the furthest point

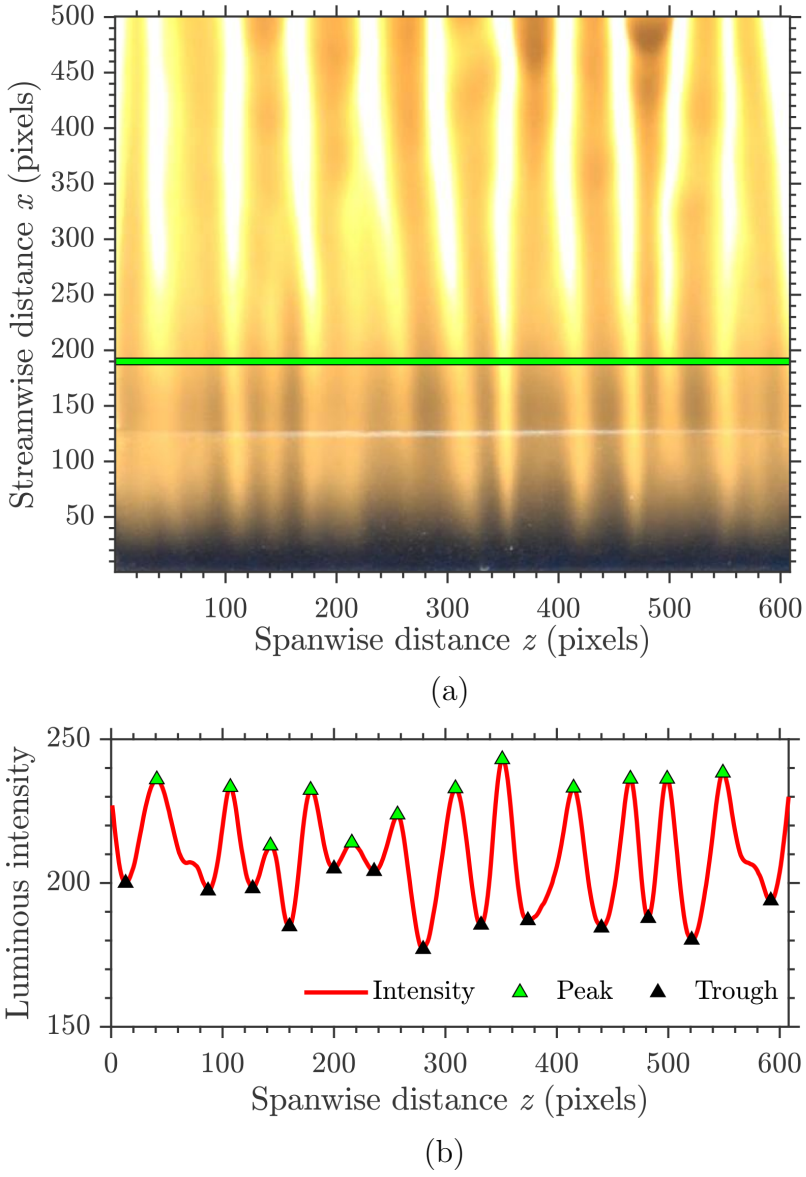

Figure 3.10: Flame streak detection: (a) top-view of the propane boundary-layer flame at $U = 0.99$ m/s and TI = 0.8%. The thin green slit represents the analysis region at $x = 8$ cm. (b) Smoothed luminous intensity profile of the analysis region, black triangles mark the detected trough location, green triangles mark the detected streak location and the space between neighboring peaks, determined as the streak spacing (l).

where flame was determined to be present (within 5 mm of the downstream surface)

was defined as the flame attachment length [89].

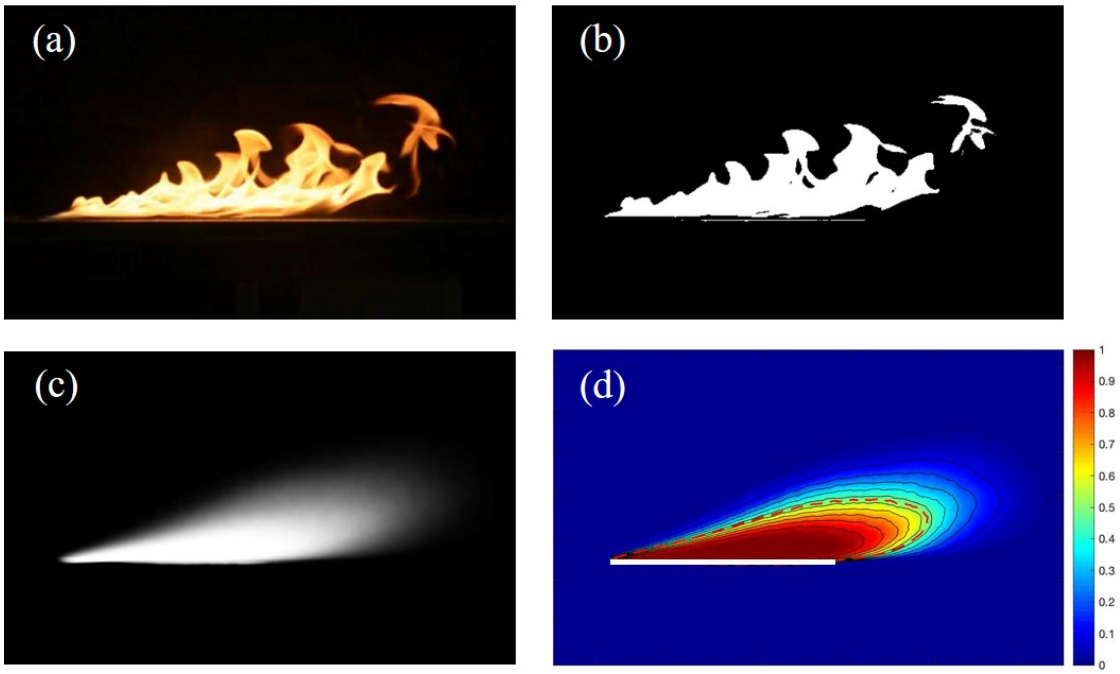

Figure 3.11: Image processing on attached flame

3.4 Results

3.4.1 Flow characterization

In order to understand the effect of freestream turbulence on the downstream flame, it is necessary to characterize the incoming flow. Velocity measurements upstream of the test apparatus were taken for different wind speeds and perforated grids used. In the test region of the wind tunnel, the centerline velocity was first characterized at heights from 30 mm to 140 mm off the base of the tunnel. The mean flow velocity (U) displayed in Fig. 3.12(a) shows a uniform flow profile across the tunnel height for all flow velocities. Meanwhile, Fig. 3.12(b). shows that the background turbulence intensity (TI) of the wind tunnel remains low (TI $< 1\%$) for all cases, ensuring a laminar incoming flow which will be examined as a reference

case.

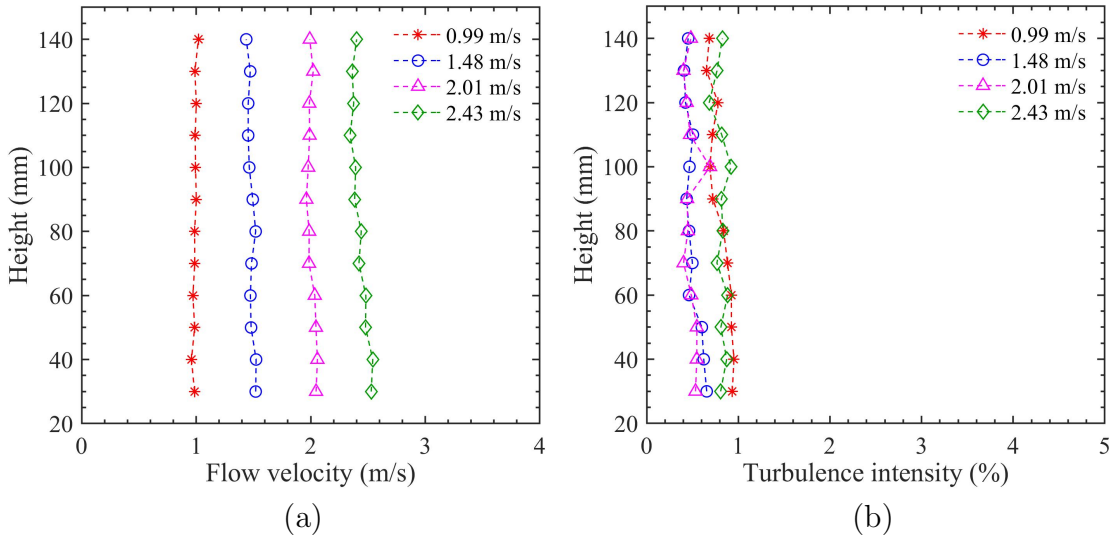

Figure 3.12: (a) Centerline flow velocity at different heights of the test region and (b) the background turbulence intensity (TI) of the flow at different heights.

Additionally, the flow velocity and turbulence intensity at 5 cm away from the tunnel exit was mapped with a 2.5 cm spatial resolution for no-grid and grid 1 conditions. The results were further interpolated using a 200 $\times$ 200 resolution. Figures 3.13 and 3.14 display the U and TI under laminar and grid 1 conditions, respectively. Note that for grid 1 condition, the TI at the edges were set to zero for a better illustration of the overall TI. The core region of the tunnel maintains a relatively uniform U and TI across different bulk flow velocities, confirming that nearly homogeneous turbulence were produced in the current wind tunnel. For grid 2 and grid 3 conditions, the flow condition was examined along the vertical centerline to ensure the uniformity of the flow.

Within the boundary-layer, separate velocity measurements over the test surface were taken to better characterize the incoming flow. Figure 3.15(a) displays the velocity profiles of the flow at $x = 28$ cm, which are formed using perforated grids

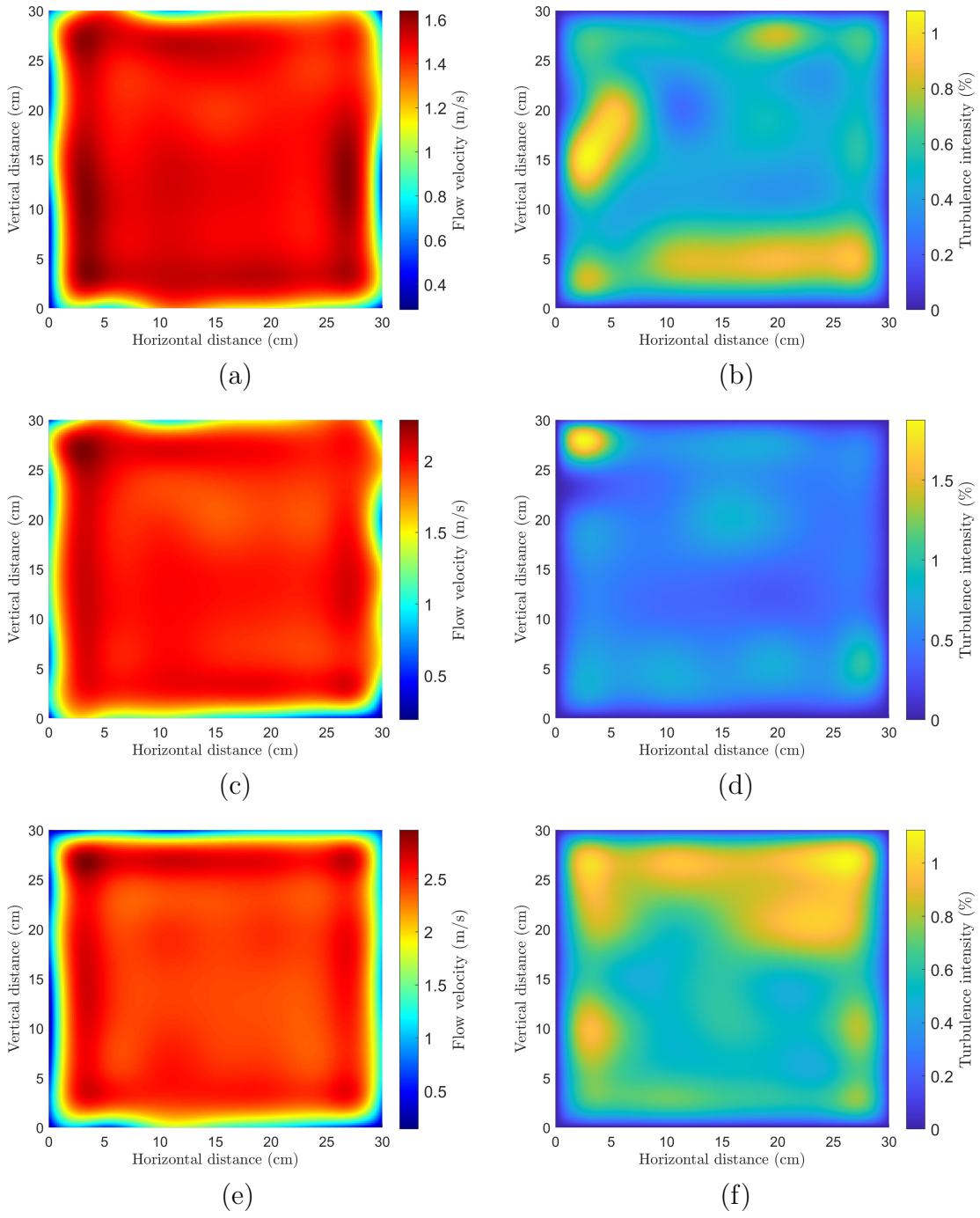

Figure 3.13: Map of the flow velocity and turbulence intensity at $x = 5$ cm: (a) $U = 1.48$ m/s, (b) TI under $U = 1.48$ m/s without grid, (c) $U = 2.01$ m/s, (d) TI under $U = 2.01$ m/s without grid, (e) $U = 2.43$ m/s, (f) TI under $U = 2.43$ m/s without grid.

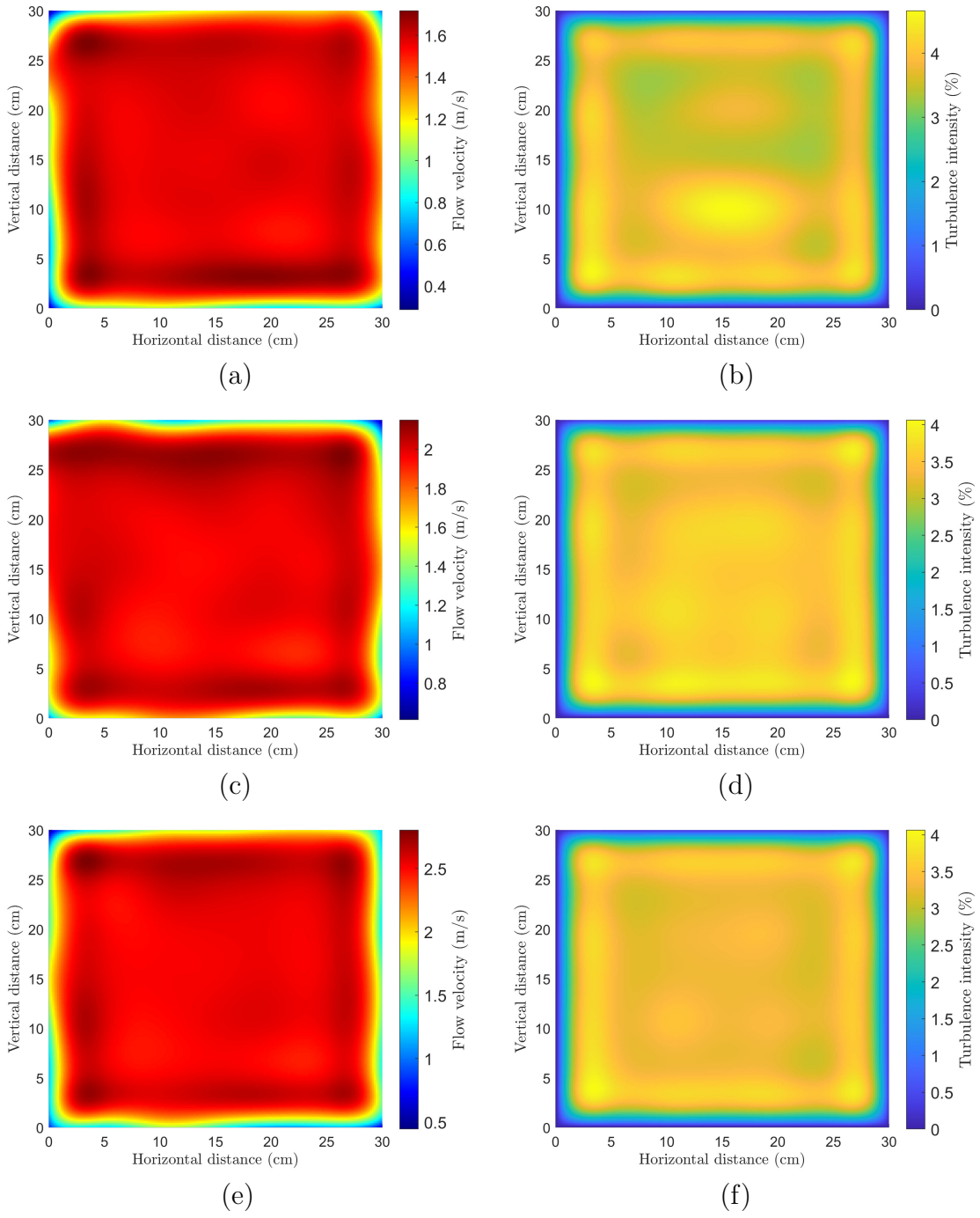

Figure 3.14: Map of the flow velocity and turbulence intensity at $x = 5$ cm: (a) $U = 1.48$ m/s, (b) TI under $U = 1.48$ m/s with grid 1, (c) $U = 2.01$ m/s, (d) TI under $U = 2.01$ m/s with grid 1, (e) $U = 2.43$ m/s, (f) TI under $U = 2.43$ m/s with grid 1.

and a bar with a 1.48 m/s mainstream velocity. Results show that the presence of the grid has less of an impact on the freestream velocity (with a velocity difference less than 0.1 m/s). In contrast, different levels of TI ranging from 2.5% to 15.3% were achieved using different grids, as plotted in Fig. 3.15(b). A combination of small hole size and high solidity ratio contributed to the highest flow TI under the grid 3 condition in this experiment. Meanwhile, higher levels of TI were detected within the near-wall region (with a height less than 10 mm) due to the low near-wall flow velocity. Beyond this region, the flow had a relatively uniform TI along the vertical direction. The root-mean-square (RMS) of the velocity fluctuation displayed in Fig. 3.15(c) shows a similar trend but with less variation within the near-wall region. Compared with the perforated grids, adding a metric bar upstream of the burner perturbed the near-wall flow. High resolution near-wall flow profiles under laminar and bar conditions in Fig. 3.15(d) show the existence of a near zero downstream velocity behind the bar. This fact suggests the formation of a reversed flow regime which further promotes boundary-layer transition to turbulence.

Without additional perturbations to the flow, freestream turbulence (FST) naturally decays along the streamwise direction. Figure 3.16 displays the flow TI downstream of the wind tunnel exit (10 cm after the grid) with the plotted data representing an average of TIs measured at 5, 10 and 15 cm heights above the test surface. It is observed that relatively stable flow TIs were achieved after an initial decay. Figure 3.16(a) shows that flow TIs generated by the same grid remain relatively similar at different flow velocities. In contrast, the plotted data in Fig. 3.16(b) shows that a higher grid solidity ratio leads to a significant increase of flow

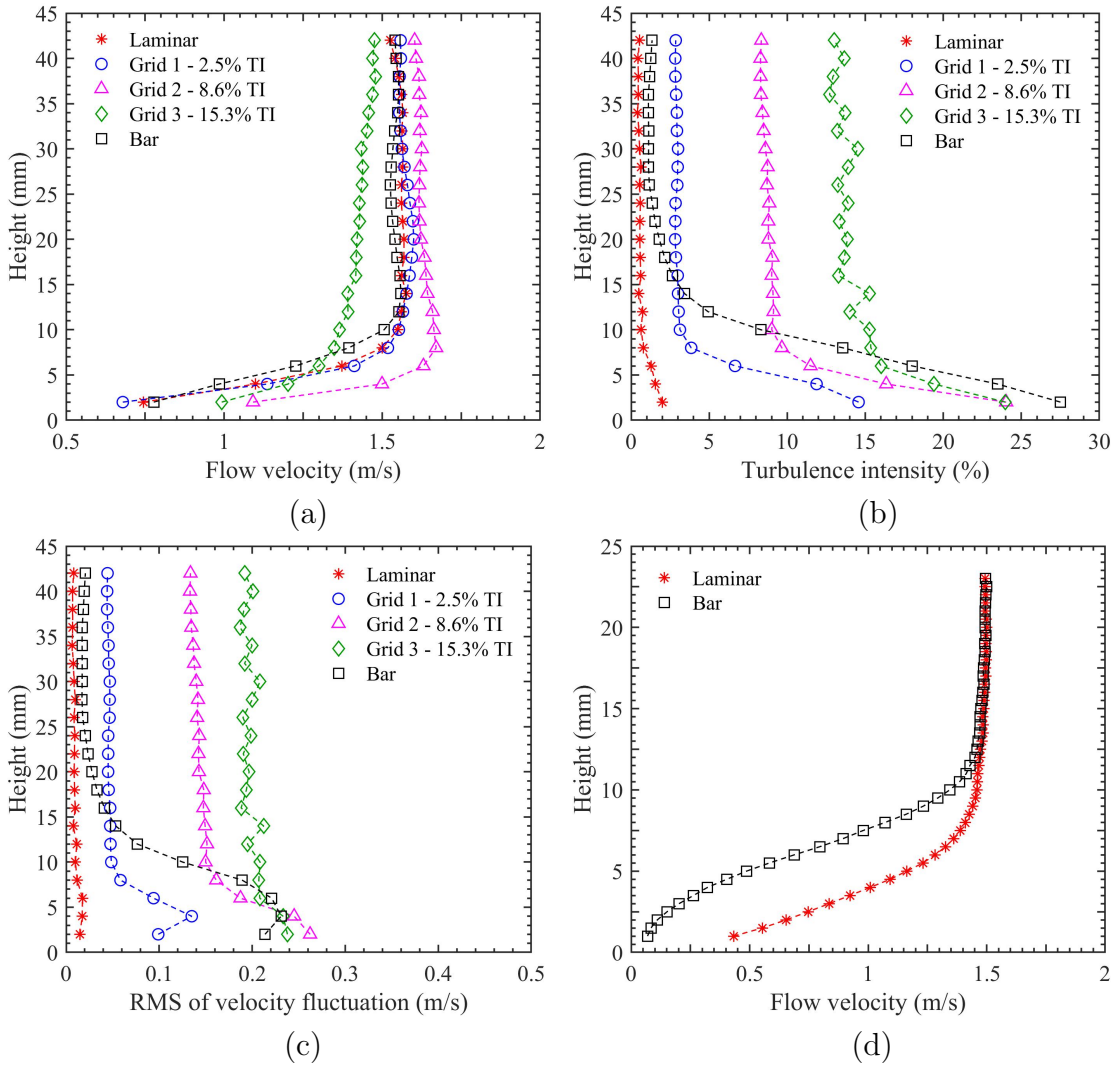

Figure 3.15: (a) Boundary layer velocity profiles at $x = 28$ cm with a 1.48 m/s mainstream velocity, (b) turbulence intensity (TI) profiles, (c) RMS of the velocity fluctuation and (d) very fine near-wall velocity profiles under laminar and bar conditions at $x = 23$ cm (3 cm behind the bar).

TI. The solidity ratio, furthermore, is determined by the grid hole size and the center-to-center distance of adjacent holes, as defined in Eq. 3.3.

3.4.2 Flame streaks

Top-views of a 7.5 kW boundary-layer flame under different flow TIs were taken and are displayed in Fig. 3.17. Under laminar flow conditions, stable spanwise

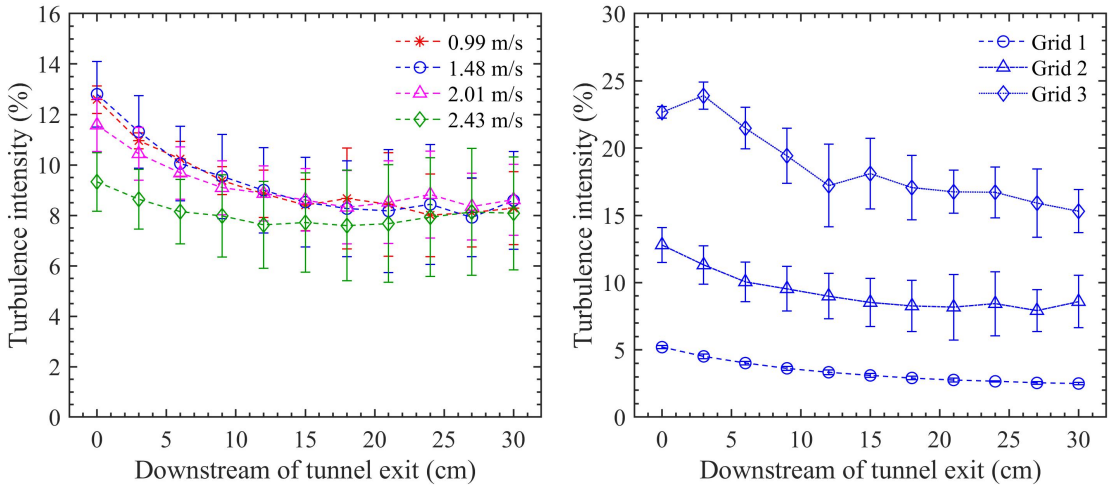

Figure 3.16: (a) Turbulence decay measured at grid 2 condition with different flow velocities and (b) turbulence decay for different grids at $U = 1.48$ m/s. Error bars shown represent the standard deviation of the measured TIs at 5, 10 and 15 cm heights above the test surface.

vortex roll structures are observed in Fig. 3.17(a), suggesting that coherent structures are prevalent even in the laminar boundary layer. Downstream of the flame, these pre-existing coherent structures develop into profound flame streaks, i.e., the prominent luminous streaks described earlier. In-between adjacent flame streaks, the low brightness region is defined as a flame trough. The observation of these well-established streaks and troughs indicates a three-dimensional boundary-layer flame. When freestream turbulence is imposed to the incoming flow, the pre-existing coherent structures are disturbed. The flame starts to transition to turbulence at an early stage as seen in Figs. 3.17(b-e). Increasing TI destabilizes streaky flame structures and leads to interactions between adjacent streaks. At a 2.5% TI, streamwise streaks start to exhibit sinuous behavior downstream; when TI increases to 8.6%, the streamwise flame extension length decreases and flame streak breaking, merging, and splitting are observed; the most significant flame streak interaction is observed

when the TI reaches 15.3%. Moreover, at 15.3% TI, flames are observed to exhibit very similar properties to the tripped bar case, indicating that the flame

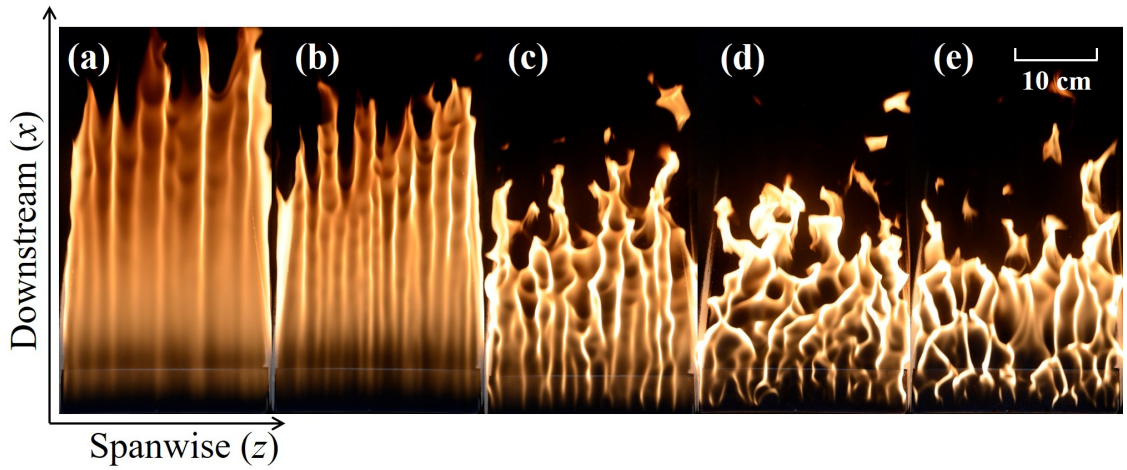

Figure 3.17: Top-views of a 7.5 kW flame at $U = 1.48$ m/s for (a) laminar: 0.5% TI, (b) grid 1: 2.5% TI, (c) grid 2: 8.6% TI, (d) grid 3: 15.3% TI, and (e) bar conditions.

The presence of flame streaks and troughs is believed to affect the downstream heat flux through modification of the local flame standoff distance. It has been shown that the upwash and downwash motions in adjacent flame streaks bend the flame sheet toward and away from the downstream surface, respectively [31]. The area between flame streaks represents a high heat flux region to the downstream surface; the spacing in this region was therefore extracted through image processing to study this effect. Mean streak spacing, l_m, is displayed in Fig. 3.18(a) as a function of downstream location (x). Note that the statistical value of streak spacing follows a log-normal distribution [32] and therefore has a variance from the mean of up to 50%. Under laminar incoming flow conditions, a sharp decrease in l_m is observed between $x = 6$ cm and $x = 10$ cm at all four velocities, indicating that the onset of the flame streaks occurred in this region. Upstream of this region, the relatively

low level of instability in a laminar boundary-layer disfavors the onset of Reynolds stress perturbations, resulting in less streaks with a relatively large mean spacing. To further understand this phenomenon, a coefficient of variation (CV) of the streak spacing is calculated as

$$\mathrm{CV} = \sigma / l_m \tag{3.5}$$

where σ represents the standard deviation of the streak spacing. The results are displayed in Fig. 3.18(b). A higher CV is observed within the initial region which could be driven by the generation of new flame streaks. Further downstream, l_m either remains relatively constant (under $U = 0.99$ and 2.43 m/s) or increases at a slower pace (under $U = 1.48$ and 2.01 m/s). It is observed that CV decreases at downstream locations, indicating that the onset of the streak structure has completed. Meanwhile, the CV is positively related to the mean flow velocity, which is likely to be driven by the stronger instabilities associated with the higher velocity under low TIs. Overall, a very limited streamwise streak growth rate is observed under laminar flow conditions. This indicates that buoyancy from the flame is not enough to drive the significant streak growth reported in a previous study [32]. Another disturbance, namely external flow turbulence, seems to be a plausible source because previous literature [82–84] has shown that freestream turbulence contributes strongly to the growth of streaks in non-reactive boundary-layer flows.

To test this hypothesis under reacting flow conditions, different levels of turbulence intensities were added to the incoming flow. Mean streak spacing under

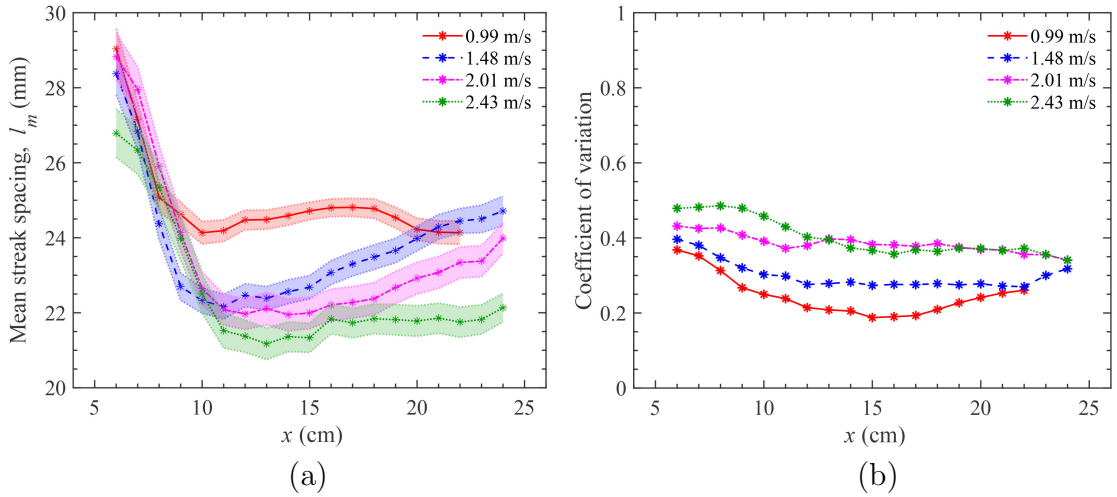

Figure 3.18: (a) Mean streak spacing vs. downstream location (x) under laminar incoming flow conditions and (b) coefficient of variation of the streak spacing. The shaded area in (a) represents 1/20 of the standard deviation of the mean for readability. The gas burner is located between $x = 0$ and $x = 5$ cm. The heat release rate of the flame was maintained at 7.5 kW.

different flow TIs and velocities were measured and plotted in Fig. 3.19. Unlike the laminar flow condition, adding grid-generated turbulence resulted in a uniform onset of flame streaks. Initially, at the region between $x = 4$ and $x = 7$ cm, a sudden surge in l_m occurred, possibly due to the momentum normal to the downstream surface associated with the gas burner. Downstream of this region (at $x > 7$ cm), the effect of the normal momentum fades away and a consistent growth in streak spacing is observed. For the grid 1 condition displayed in Fig. 3.19(a), flow TI remains relatively low at 2.2% to 4.1% and l_m grows linearly along the streamwise direction before becoming saturated. When TI increases to a maximum value of 16.8%, as we can see in Figs. 3.19(b-c), the growth of l_m transitions from nearly linear to quadratic. Meanwhile, the streak spacing is seen to become wider when TI increases at the same downstream location.

Coefficient of variation (CV) of the streak spacing is displayed in Fig. 3.20.

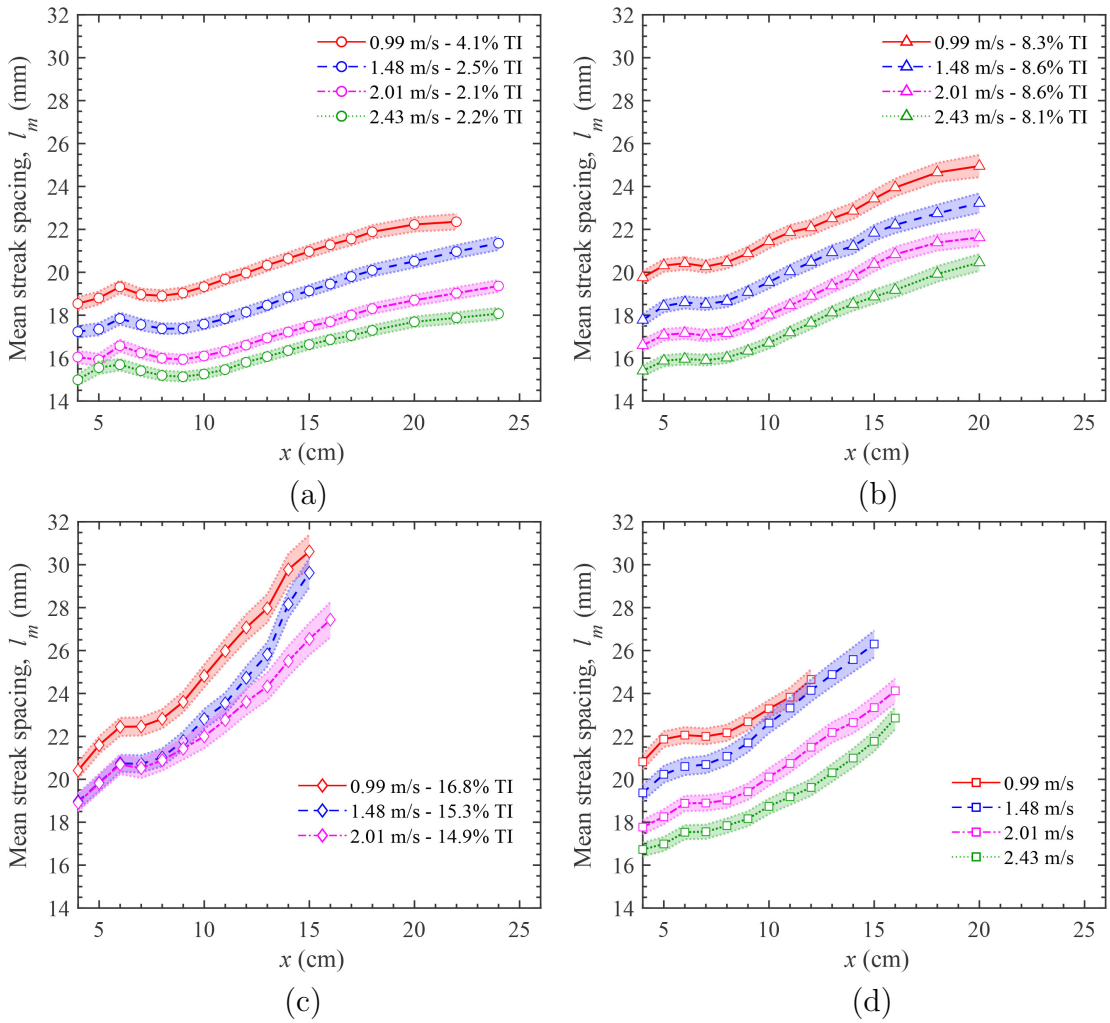

Figure 3.19: Mean streak spacing vs. downstream location x for all flow TIs and velocities: (a) Grid 1, TI = 2.1% - 4.1%, (b) grid 2, TI = 8.1% - 8.6%, (c) grid 3, TI = 14.9% - 16.8%, and (d) bar conditions. The heat release rate of the flame was maintained at 7.5 kW. The shaded area represents 1/20 of the standard deviation.

Unlike the laminar condition, CV profiles under different flow velocities collapse for a fixed grid (i.e., similar flow TIs). The stable value of the CV for grid 1 condition is at 0.27 $\sim$ 0.29 ($x > 10$ cm). This value increases to 0.31 $\sim$ 0.35 when grid 2 was used. Under grid 3 condition, CV further increases to 0.4 $\sim$ 0.6 depending on the downstream locations. A similar trend is observed for bar condition where CV ranges from 0.34 to 0.45. These results show that the CV is barely affected by the

flow velocity when freestream turbulence is imposed into the flow, suggesting that freestream turbulence induced instabilities play a dominating role.

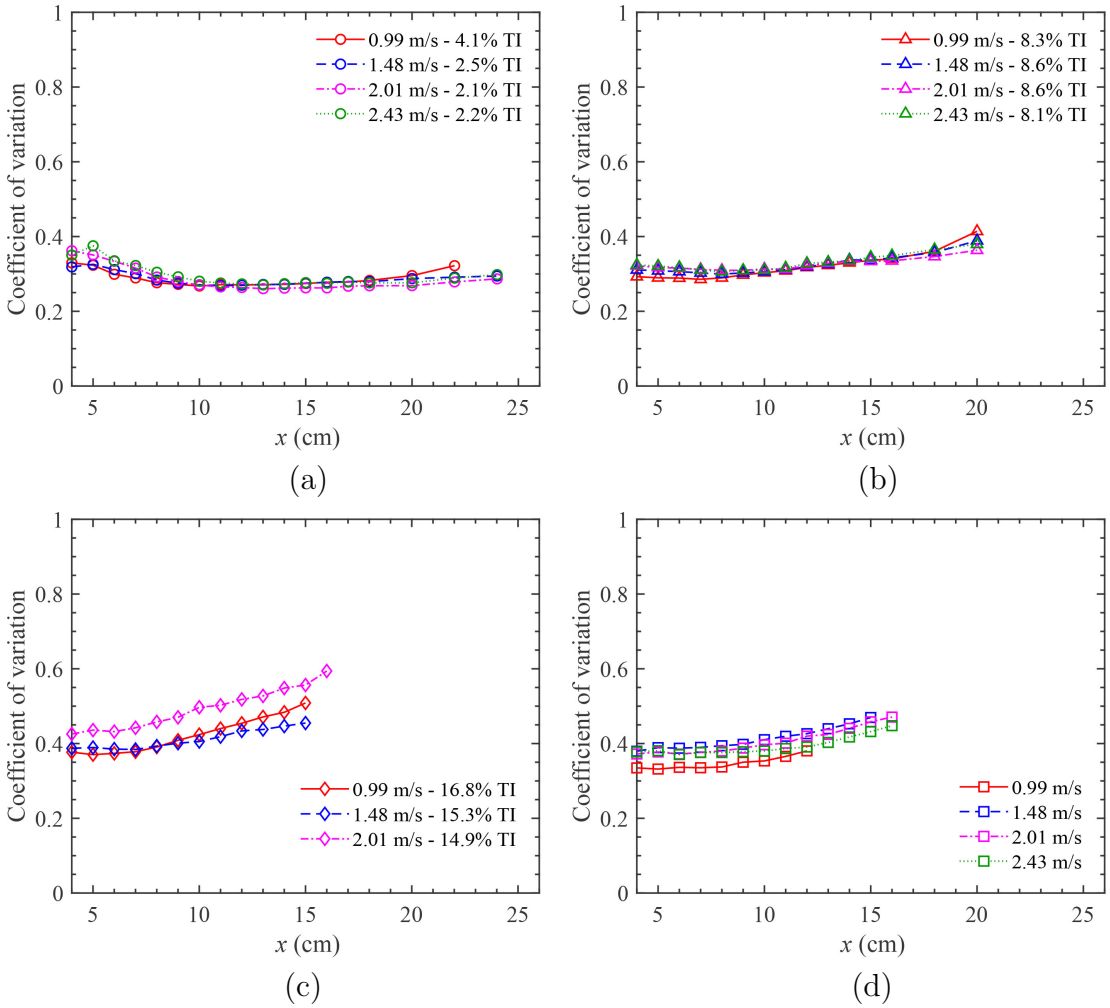

Figure 3.20: Coefficient of variation of the streak spacing vs. downstream location x for all flow TIs and velocities: (a) Grid 1, TI = 2.1% - 4.1%, (b) grid 2, TI = 8.1% - 8.6%, (c) grid 3, TI = 14.9% - 16.8%, and (d) bar conditions. The heat release rate of the flame was maintained at 7.5 kW. The shaded area represents 1/20 of the standard deviation.

These results indicate that instability growth theory may be applicable when considering a freestream turbulence effect. Similar results have been reported by Miller et al. [31, 32] who found that the quadratic growth of streamwise streak spacing can be scaled through Rayleigh-Taylor instability theory. Moreover, the

asymptotic behavior of streak spacing fades away with increasing TI. This is possibly caused by a self-sustaining turbulent state triggered by high flow TI [84] as robust streak growth can be maintained at this state. Additionally, l_m profiles under bar conditions show a similar trend with grid 3 conditions but a slightly lower value due to a lack of three-dimensional velocity fluctuations (see Fig. 3.15(b)). Nevertheless, this fact supports the statement that the same magnitude of instabilities was achieved under these two conditions (i.e., a nearly fully developed turbulent state).

Additionally, for all test cases, results show that the mean streak spacing increased along the streamwise direction but decreased with increasing flow velocity. This is thought to be caused by a competition between boundary-layer instabilities and flow momentum. Both buoyantly driven Rayleigh-Taylor instabilities and freestream turbulence lead to the growth of the streamwise vortex rolls which are further manifested as increased streak spacing. A strong streamwise momentum, however, leads to a thinner boundary-layer thickness which limits the expansion of the vortex roll.

3.4.2.1 Role of momentum

The organized mean streak spacing (see Fig. 3.19) at all test velocities suggest a possible means of performing a scaling analysis. Previous studies [32,82] suggested that the initial streak spacing is directly related to the boundary-layer thickness. Moreover, a clearly negative relationship between l_m and U has been observed in the current experiments. According to the boundary-layer theory [99], the thicknesses

(δ) of laminar and turbulent boundary-layers can be expressed as

$$\delta(x) = 4.91x\mathrm{Re}_x^{-0.5} \tag{3.6}$$

and

$$\delta(x) = 0.37x\mathrm{Re}_x^{-0.2} \tag{3.7}$$

respectively. The local Reynolds number (Re_x) is calculated as

$$\mathrm{Re}_x = Ux/\nu \tag{3.8}$$

where ν is the kinematic viscosity of the fluid. In other words, streak spacing should be able to scale with U^{-n} if it is intrinsically related to δ. Therefore, a scaling factor $(U/U_{ref})^{-n}$ with a $0.20 \leq n \leq 0.50$ is proposed to collapse the mean streak spacing for all flow velocities. A reference velocity of $U_{ref} = 2.43$ m/s was chosen for the current analysis. The scaled mean streak spacing, $l_m/(U/U_{ref})^{-n}$, is displayed in Fig. 3.21. Note that the data upstream of $x = 8$ cm could be affected by the normal momentum associated with the gas burner, and thus, is not included in later analysis. Values of n were optimized at different flow turbulence conditions. We found that $n = 0.30$, 0.28, 0.20 and 0.40 collapses the $l_m/(U/U_{ref})^{-n}$ relationship well for all flow velocities at grid 1, grid 2, grid 3 and bar conditions. This is expected as changing n from 0.30 to 0.20 with increasing flow turbulence intensities follows the changing trend of the exponent of boundary-layer thickness (from 0.50 to 0.20) when laminar to turbulent transition occurs. In addition, the exponent of $n = 0.40$ at bar conditions is close

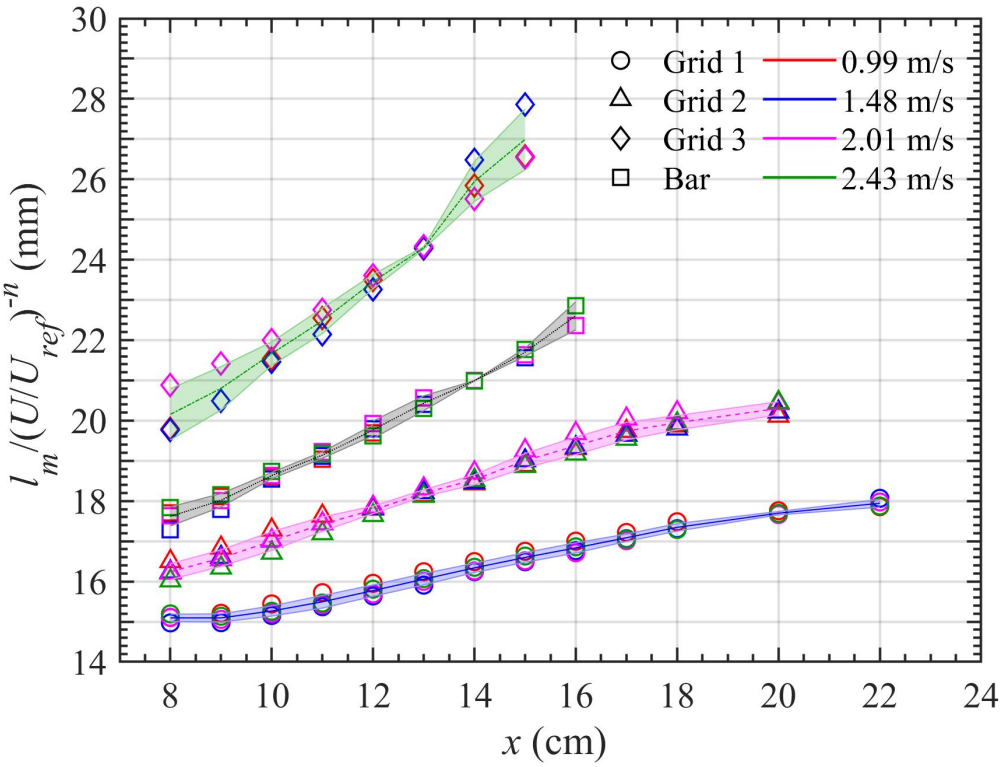

Figure 3.21: Scaled mean streak spacing $l_m/(U/U_{ref})^{-n}$ vs. downstream location (x) for all incoming flow velocities and TIs (Grid 1: TI = 2.1% - 4.1%, grid 2: TI = 8.1% - 8.6%, and grid 3: TI = 14.9% - 16.8%). n varies at different flow TI conditions: $n = 0.30$ for grid 1, $n = 0.28$ for grid 2, $n = 0.20$ for grid 3, and $n = 0.40$ for bar conditions. The heat release rate of the flame was maintained at 7.5 kW. The shaded area represents the standard deviation of the $l_m/(U/U_{ref})^{-n}$ at all flow velocities.

to the theoretical exponential value (0.5) for a laminar boundary-layer, indicating that placing a bar in a laminar flow did not change the thickness of the boundary-layer significantly. This observation agrees with the cold flow boundary-layer data displayed in Fig. 3.15(d). Nonetheless, transition to turbulence occurred at bar conditions. Overall, the experimental data suggests that momentum does not affect the growth rate of streak spacing.

3.4.2.2 Role of free-stream turbulence

In spite of the momentum effect, Fig. 3.21 also shows that the initial streak spacing is enlarged by a higher flow turbulence intensity. In order to better characterize the freestream turbulence effect on streak development, the mean streak spacing was normalized as $l_m/l_{m,x=8cm}$ (x = 11 cm for laminar case) and plotted in Fig. 3.22. The projected normalized laminar and turbulent cold flow boundary-layer thicknesses (δ^*) were also calculated and plotted. Under a laminar condition, the streak spacing increases at a very slow pace, and even remains nearly constant along several downstream locations. It is observed that the normalized streak spacing is confined within the laminar boundary-layer, suggesting limited growth of instabilities at this condition even with the presence of flame buoyancy. When flow TI reaches between 2.1% to 4.1%, a 19% increase of the mean streak spacing is observed at x = 22 cm. This rate exceeds the growth rate of the laminar boundary-layer thickness but still sits within the turbulent boundary-layer. Further increase of TI, i.e., between 8.1% to 8.6% under the grid 2 condition, leads to a larger normalized l_m which lies beyond the vicinity of the normalized turbulent boundary-layer thickness. Finally, under the grid 3 condition where the flow TI is as high as 16.8%, a remarkable streak growth rate, as much as 34%, is seen at x = 15 cm. As expected, the presence of the bar results in a fast growth of normalized l_m but remains slightly slower than the grid 3 condition. This demonstrates that the freestream turbulence induced instability contributes to a faster growth of the mean streak spacing compared to the flame buoyancy-induced instability.

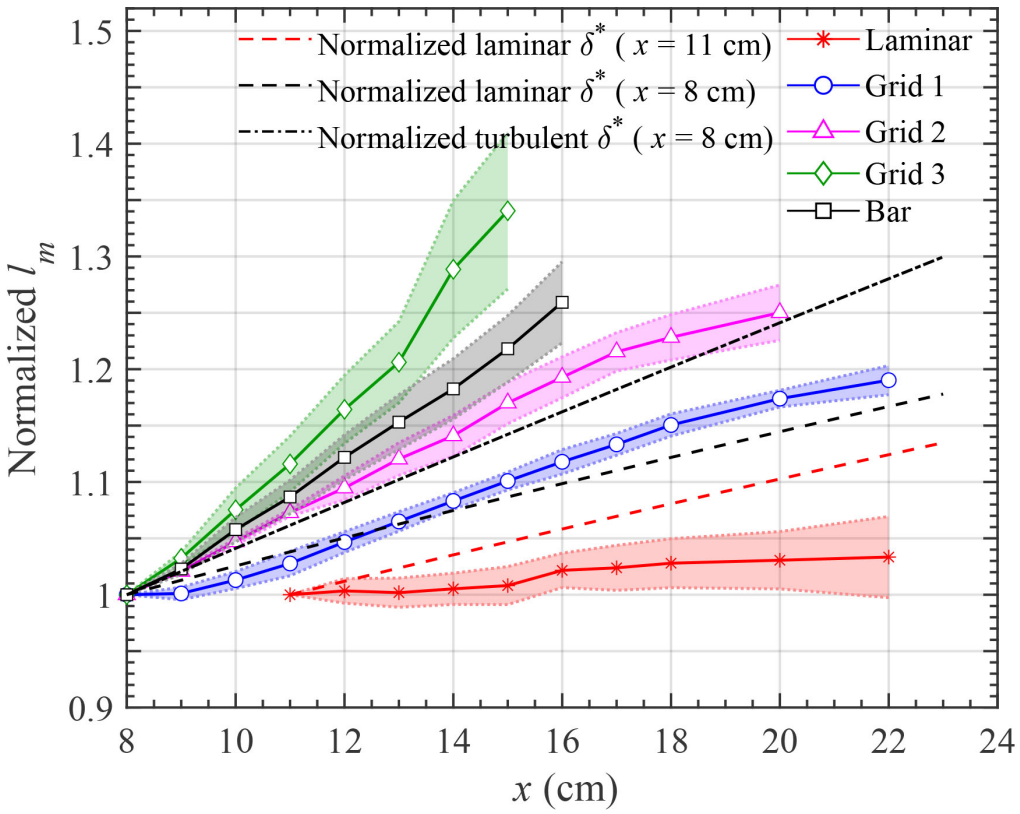

Figure 3.22: Normalized mean streak spacing vs. downstream location (x) at different flow TIs (Grid 1: TI = 2.1% - 4.1%, grid 2: TI = 8.1% - 8.6%, and grid 3: TI = 14.9% - 16.8%). The plotted data represents an average of normalized l_m for all flow velocities. The heat release rate of the flame was maintained at 7.5 kW. The shaded area represents the standard deviation of the normalized mean streak spacings at all flow velocities.

Aside from changing the streak spacing, the arising instability induced by freestream turbulence is also explicitly displayed through the movement of flame streaks. Figure 3.23 displays a typical path for a flame streak recorded at a 240 FPS. Over time, the flame streak grows (at frame (F):1-5), moves downstream, expands and becomes sinuous (F: 5-14), merges with surrounding streaks (F: 17-20), and shows a limited lifetime. To examine this timescale, the persistence of individual streaks was tracked as a function of time through a thin stationary virtual slit (i.e., the green slit in Fig. 3.23) at different downstream locations (more details

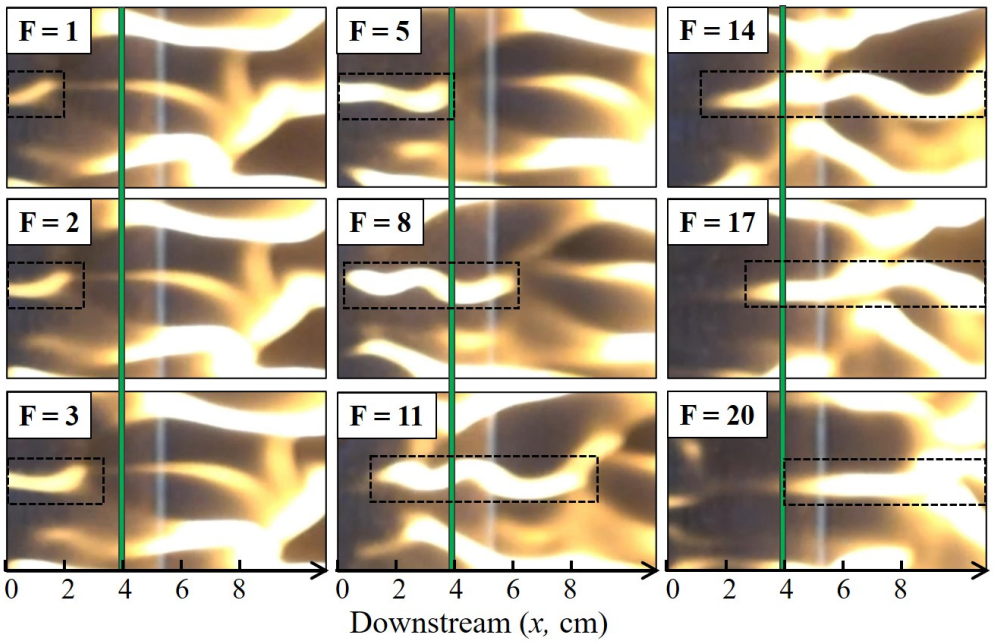

Figure 3.23: Individual flame streak path at grid 3 condition with $U = 1.48$ m/s for a 7.5 kW flame.

can be found in Ref. [32]). The duration over which a streak can be individually distinguished is then defined as the streak duration time.

Figure 3.24 displays the mean streak duration time for different flow TIs along the downstream location. The number of streaks observed for different grid/bar conditions are summarized in Table. 3.2. The mean streak duration time remains relatively constant moving downstream. However, a significant decrease, from ~ 0.4 s to ~ 0.05 s, is observed when the flow TI increases from 2.1% to 15.3%. The same trends are also found for other incoming flow velocities. These results indicate that disturbances induced by the freestream turbulence lead to the breakdown of stable streaks (e.g., streak breaking, merging and splitting) and, presumably, the perturbations associated with these unstable streaks further bolster the flow instability. This mechanism of structural instability, which has been revealed in non-reactive

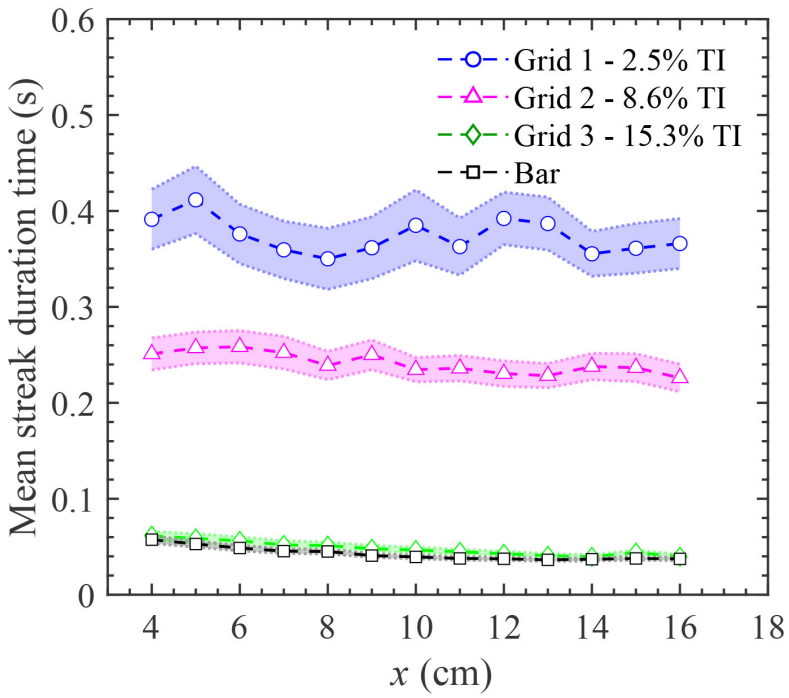

Figure 3.24: Mean streak duration time vs. downstream location (x) for different flow TIs at $U = 1.48$ m/s. Note that flame streaks remained very stable under laminar incoming flows and thus could be assumed to have an infinite duration time in this experiment. The shaded area represents 1/10 of the standard deviation. The heat release rate of the flame was maintained at 7.5 kW.

wall-bounded flow by Farrell and Ioanno [84], could possibly mediate the transition to a self-sustaining turbulent state under which non-linear flame streak behavior was observed.

Table 3.2: Total numbers of streaks identified for different grid/bar conditions

Grids/Bar	Grid 1	Grid 2	Grid 3	Bar
Number of streaks	107∼294	167∼680	513∼1218	300∼1098

Note: The reported values reflect the variation caused by flow velocities and downstream locations.

In order to evaluate the perturbations induced by freestream turbulence (FST), we used a Strouhal number (St) and a Taylor-microscale Reynolds number (Re_λ) to represent the ensemble effect of flow instabilities on the boundary-layer flame and

the cold flow turbulence, respectively. The Strouhal number, St, is defined as

$$\mathrm{St} = f L_{flame}/U \tag{3.9}$$

where f is the average frequency of the streak structures (i.e., inverse of the mean streak duration time), L_{flame} is the flame attachment length (see Section 3.4.3) and U is the average cold flow velocity. The uncertainty of the St was calculated as

$$\sigma_{\mathrm{St}} = \mathrm{St}\sqrt{(\frac{\sigma_f}{f})^2 + (\frac{\sigma_{L_{flame}}}{L_{flame}})^2 + (\frac{\sigma_U}{U})^2} \tag{3.10}$$

where σ_f, $\sigma_{L_{flame}}$ and σ_U are the standard deviation of the streak frequency, flame attachment length and flow velocity, respectively. The Taylor microscale Reynolds number, Re_λ, is calculated as

$$\mathrm{Re}_\lambda = u'_{rms}\lambda/\nu \tag{3.11}$$

where u'_{rms} is the root-mean-square of the velocity fluctuations, λ is the Taylor microscale [100] and ν is the air kinematic viscosity at ambient temperature. To evaluate the Taylor microscale ($\lambda = U\tau$), the integral time scale of the cold flow, τ, is calculated from the time history of the flow velocity, $u(t)$, using a normalized auto-correlation function R(t) through Eq. 3.12

$$\tau = \int_0^\infty R(t)dt \tag{3.12}$$

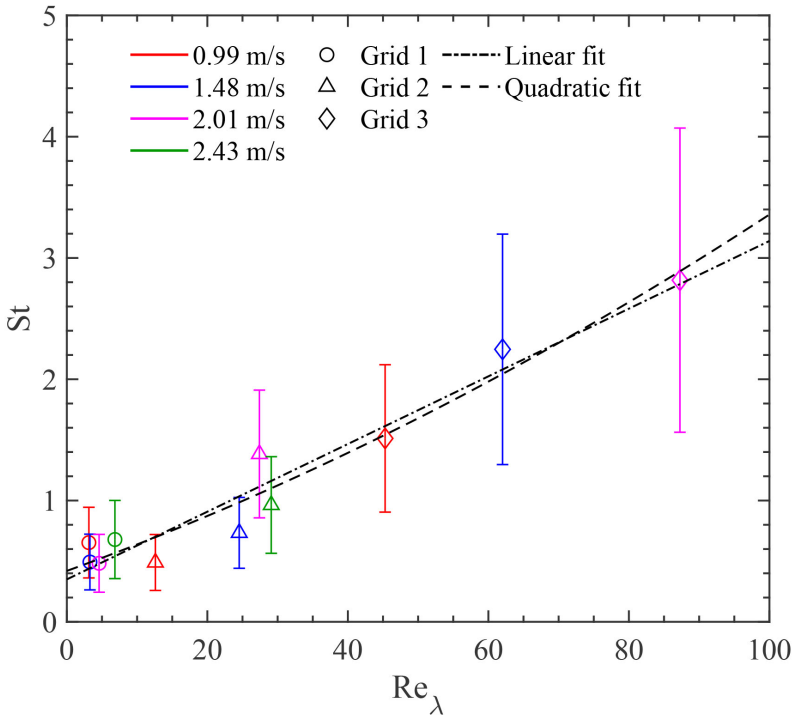

Figure 3.25: Empirical correlations of St and Re_λ. A linear: $St = 0.028Re_\lambda + 0.35$ (R^2=0.94), and quadratic: $St = 0.000084Re_\lambda{}^2 + 0.021Re_\lambda + 0.42$ (R^2=0.95) fit are shown for comparison. The heat release rate of the flame was maintained at 7.5 kW.

where

$$R(t) = \langle u(t)u(t + \Delta t)/u^2 \rangle \tag{3.13}$$

After processing the mean streak duration time and FST data using this method, Fig. 3.25 was obtained for a 7.5 kW flame. Both linear and quadratic functions fit the experimental data well. The displayed streak fluctuation trend aligns well with the quasi-linear (or quadratic) growth of the streak spacing reported in foregoing analysis. In summary, these results along with the analysis on the mean streak spacing growth demonstrate that FST significantly modified the coherent flame structures.

3.4.3 Flame attachment

As mentioned in Section 3.4.2, adding turbulence to the incoming flow also leads to distinct changes to overall flame extension. The length over which flame remains attached to the downstream surface is defined as the flame attachment length L_{flame} (also known as 'flame drag/extension length' for pool fire scenarios under cross-flow). To quantify the freestream turbulence effect on this parameter, pre-calibrated side-views of the flames were taken and converted to attachment length, as displayed in Fig. 3.26. Figures 3.27(a-c) plot the L_{flame} versus flow turbulence intensities at 5 kW, 7.5 kW and 10 kW fires (part of the 2.43 m/s data is missing since higher TI could not be reached at this condition). A consistent decrease of L_{flame} has been observed when higher TIs are applied. At the initial low TI region, e.g., around TI $< 8\%$, the flame attachment length decreases nearly linear against the flow TI. As a comparison, when the TI reaches nearly 15%, a significant drop in the attachment length is observed, which indicates a non-linear decreasing process. This linear to non-linear transition, similar to what we have seen on the flame streak spacing growth (as well as fluctuation) along with increasing flow TI, suggests that a quadratic decreasing function might be applicable for the analysis of L_{flame}. Aside from the FST effect, we can see that L_{flame} becomes larger at higher heat release rates and higher flow velocities, which is similar to previous literature results [88, 89]. This well-organized experimental data indicates a possible avenue of flame attachment prediction using non-dimensional parameters. Several other correlations of L_{flame} have been reported in the literature [86–88] but freestream

turbulence was not considered.

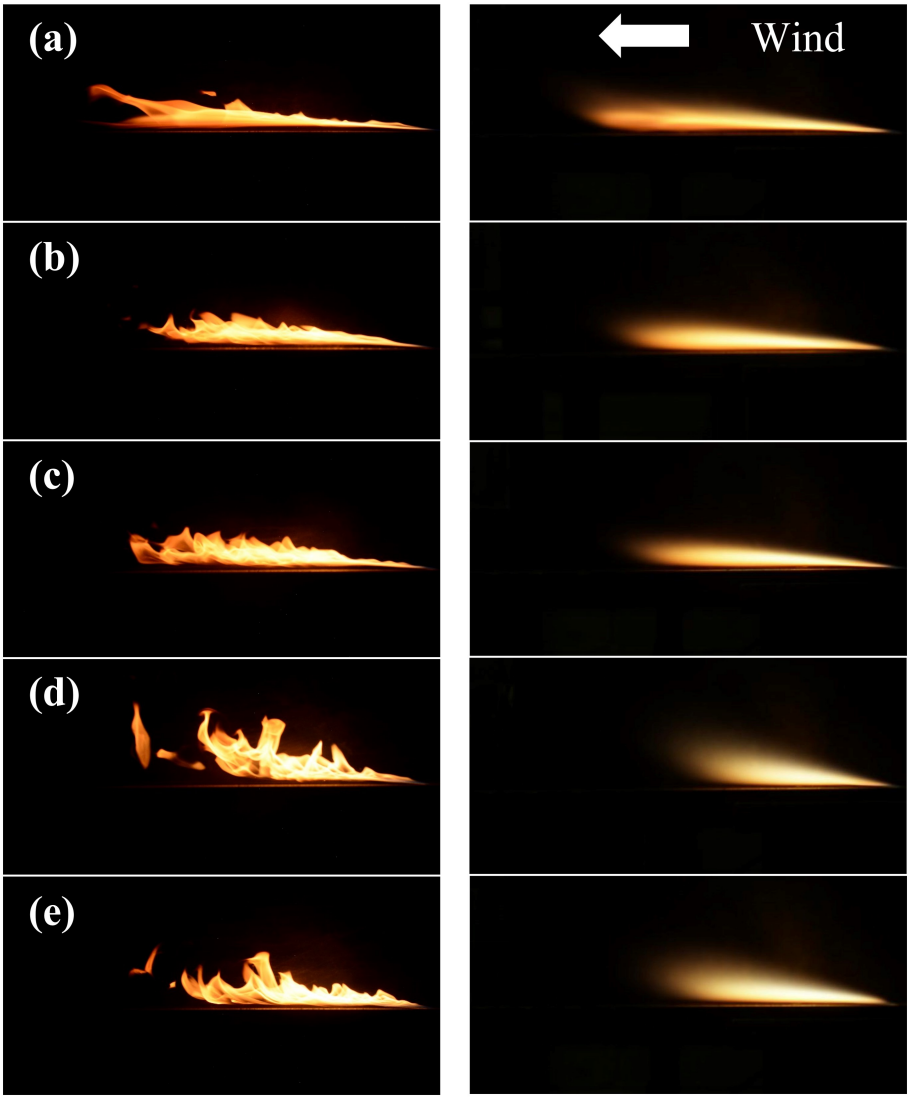

Figure 3.26: Side-views (left: snapshot, right: time-averaged) of a 7.5 kW flame at $U = 1.48$ m/s for (a) laminar: 0.5% TI, (b) grid 1: 2.5% TI, (c) grid 2: 8.6% TI, (d) grid 3: 15.3% TI, and (e) bar conditions.

With the purpose of incorporating the freestream turbulence into a relationship to predict the flame attachment length, parameters describing the flow velocities, fire source buoyancy, heat release rate of the fire and flow turbulence intensity (TI)

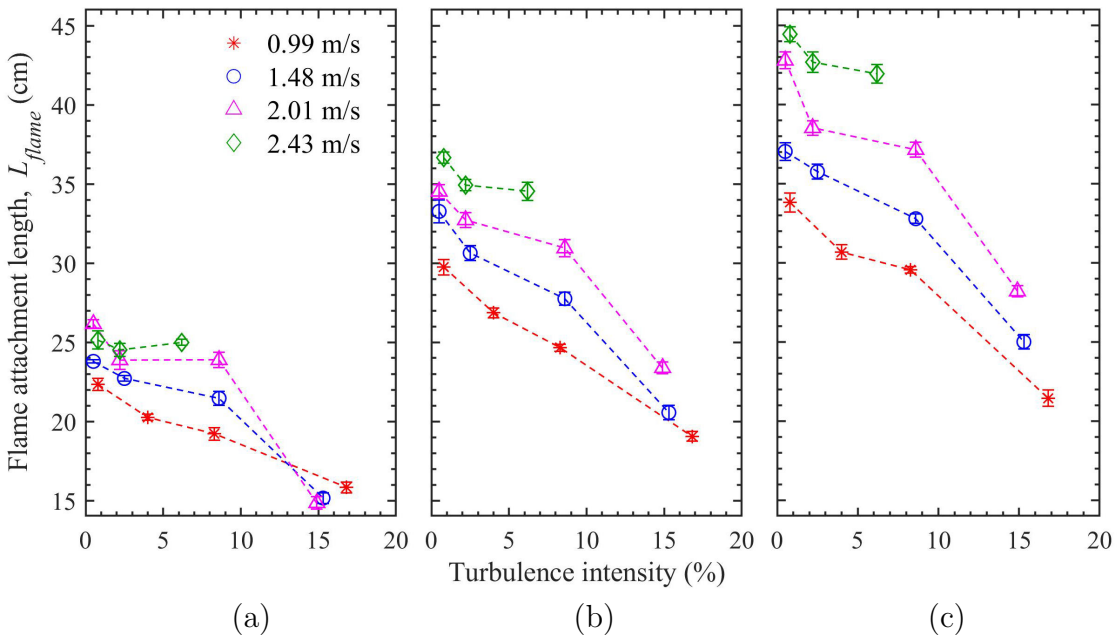

Figure 3.27: Flame attachment length vs. turbulence intensity (TI) for different flow velocities and fire HRRs: (a) 5 kW HRR, (b) 7.5 kW HRR, and (c) 10 kW HRR.

are converted to non-dimensional values. The Froude number, defined as

$$\mathrm{Fr} = U^2/gD \tag{3.14}$$

is used to represent the ratio of the inertial force of the cross flow and the buoyancy of the fire source, where g is the acceleration due to gravity and D is the streamwise depth of the gas burner. The normalized intensity of the fire is given by Eq. 3.15 [101, 102]

$$Q^* = Q'/(\rho c_p T_\infty \sqrt{gD}D) \tag{3.15}$$

with Q' being the actual fire intensity which is calculated as Q/L, L the burner spanwise length, ρ the density, c_p the heat capacity, and T_∞ the temperature of ambient air. Freestream TI is, itself, non-dimensional. Following previous findings, the effect

of the flow TI is expressed as $(1 - \mathrm{TI})^a$ to incorporate either a linear or non-linear decreasing trend of the flame attachment. It was found that an exponential value of a=3 works best for the current data. This is not unexpected since the turbulent fluctuations are three-dimensional, which result in enhanced mixing between the fuel and oxidizer, and therefore combustion with a shorter flame length. Finally, the measured actual flame attachment length, L_{flame}, is normalized as L_{flame}/D using the gas burner streamwise depth D.

The resulting non-dimensional flame attachment length is plotted in Fig. 3.15. A linear relationship fits the proposed non-dimensional parameters (Fr, Q^*, and $(1 - \mathrm{TI})^a$) and the flame attachment length. Previous pool-fire correlations [85–88] have shown a similar positive relationship between flame attachment length and Fr, with an exponent ranging from 0.07 to 0.8. For this experiment, the non-dimensional flame attachment length is found to be positively correlated with $\mathrm{Fr}^{0.15}$ and Q^*, while it is negatively correlated with the flow TI. Finally, a linear function which couples these effects is expressed as Eq. 3.16,

$$L_{flame}/D = 1.67\mathrm{Fr}^{0.15}Q^*(1 - \mathrm{TI})^3 + 1.44, for 2 < \mathrm{Fr} < 12.7. \tag{3.16}$$

This empirical relationship provides a useful way to take the freestream turbulence effect into consideration for classical flame attachment length analysis. Note that the proposed relationship is limited to a TI up to 16.8%. Further investigations will be needed for flows with higher TIs.

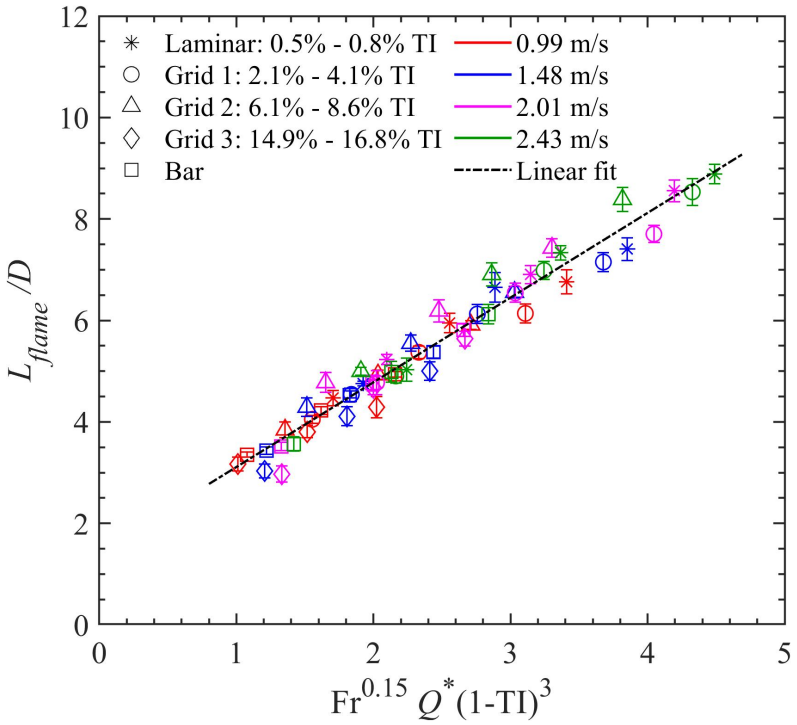

Figure 3.28: Non-dimensional correlation of flame attachment length. Linear fit of the data: $L_{flame}/D = 1.67\mathrm{Fr}^{0.15}Q^{*}(1-\mathrm{TI})^{3} + 1.44, for 2 < \mathrm{Fr} < 12.7$ in this experiment (R^2= 0.96).

3.4.4 Surface heat flux

Both the flame streak distribution and flame attachment length affect the flame to surface heat flux, a vital parameter which controls the spread rate of a flame if combustible material is available, e.g., in wildland fire spread. The above analysis has shown that freestream turbulence modifies those two factors significantly; therefore, downstream surface heat fluxes were measured using a series of Hukseflux water-cooled total heat flux gauges. Six positions were examined along the streamwise direction, with the first gauge located at x = 11 cm (6 cm downstream of the burner trailing edge). Measured heat fluxes of a 7.5 kW fire under different flow TIs are displayed in Fig. 3.29. It is noted that the boundary-layer

flames in this study had a limited fire size (HRR $\leq$10 kW) implying convective heating dominated the flame to surface heat transfer. Consequently, the plotted total heat flux data mainly reflects the trend of convective heat flux. Results show that a higher flow TI leads to a higher surface heat flux in the initial downstream regime, with a heat flux value changing from 30 kW/m^2 to nearly 40 $\sim$ 45 kW/m^2 when the free-stream TI increases from 0.5% to 15.3% under a 1.48 m/s incoming flow velocity. However, a shorter streamwise heating region is observed at higher TI, due to the decreased flame attachment length. Similar trends were observed for 5 kW and 10 kW fires, as well as other flow velocities. These results indicate an overall heat transfer enhancement at high TI conditions, analogous to what has been seen in non-reactive flows [103, 104]. Additionally, the heat flux profile of the bar condition almost overlaps with the grid 3 condition, which again supports our previous assumption that nearly fully developed turbulent flames were achieved in these cases.

The increased heat flux under high flow TI is likely to be caused by a closer mean presence of local flame sheets to the downstream surface. Specifically, flame troughs, of which the local flame sheet mostly consists [3], were redistributed and enlarged laterally by the increasing TI. The spanwise size of the trough was measured as streak spacing in Section 3.4.2 and was seen to be positively related to the flow TI. These troughs, which are essentially driven by streamwise counter-rotating vortices [82] and are pushed towards the ground by the downwash of the vortex pairs, result in steeper near-wall temperature gradients and consequently enhanced heat fluxes. A detailed investigation of the flame heat flux and downwash effect can be found

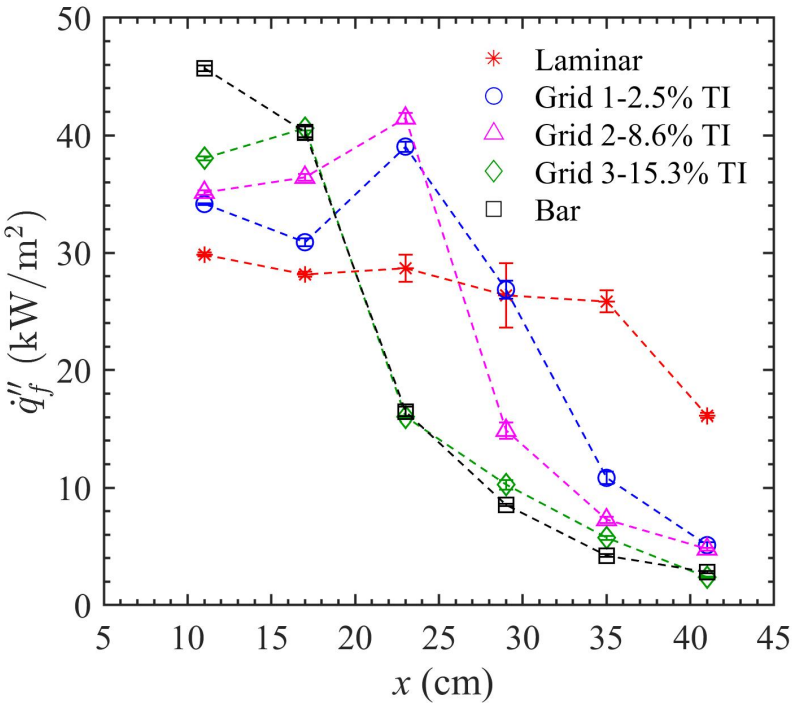

Figure 3.29: Flame to surface heat flux vs. downstream location (x) with different turbulence intensities (TIs) at $U = 1.48$ m/s. The heat release rate of the flame was maintained at 7.5 kW.

from in Ref. [31]. To characterize the global effect of freestream turbulence and its effect on the surface heat flux from boundary-layer flames, a Richardson number-based analysis was performed. The Richardson number, defined as

$$\mathrm{Ri} = \mathrm{Gr}/\mathrm{Re}^2 \tag{3.17}$$

represents the competition between natural and forced convection [28, 89] with the Reynolds number (Re) and Grashof number (Gr) expressed as

$$\mathrm{Re} = L_{flame} U/\nu \tag{3.18}$$

and

$$\mathrm{Gr} = \frac{g(T_f - T_\infty)\beta {L_{HF}}^3}{\nu^2} \tag{3.19}$$

respectively. Here, T_f and T_∞ are the average flame temperature (T_f = ~1500 K) and ambient air temperature, respectively. β is the thermal expansion coefficient, ν is the kinematic viscosity of air at T_∞, L_{HF} is the downstream location of the heat flux gauge representing the characteristic length of the buoyancy, and L_{flame} is the flame attachment length.

Figures 3.30(a-c) displays the measured heat flux versus the local Ri for 5.0, 7.5 and 10.0 kW fires, respectively. Overall, two distinct heating modes, specifically a nearly constant heat flux regime and a power-law decaying heat flux regime, are observed for each flow TI condition. This is expected since a momentum-dominated attached region and a buoyancy-dominated plume region can be formed under mixed convection flame conditions with the heat transfer processes dominated by convection and radiation, respectively. However, different heat fluxes were measured at different flow TI conditions. A fairly uniform 30 kW/m^2 average heat flux was obtained in the momentum-dominated region when the incoming flow was laminar; as a comparison, this heat flux value increased to 40 kW/m^2 when either the flow TI increased to 14.9%-16.8% or a bar was used. Intermediate heat fluxes ranging from 30 to 40 kW/m^2 were obtained when intermediate flow TIs (2.1% - 4.1% and 8.1% - 8.6%) were imposed. In other words, the flame to surface heat flux was enhanced by 33% in the momentum-dominated regime when the highest flow TI was applied in the present experiments. Meanwhile, the critical point where the heat

flux profile transitions from a momentum-dominated to plume mode, was altered by freestream turbulence. Figures 3.30(a-d) show that a transition point near Ri = 1 separates the two aforementioned heating regimes under a laminar incoming flow condition, which has also been reported in previous work [89]. When flow TI becomes higher, the value of the critical Ri decreased. Finally, a Ri = 0.1 is seen to become the critical transition point under grid 3 (with $\sim$ 15% TI) and bar conditions where nearly fully developed turbulence conditions were achieved. Overall, the Richardson number works well to quantify the entire surface heating profile of the boundary-layer flames. The resulting relationship has several other important takeaways. Given that Ri can be determined as Ri $\sim$ Gr/Re^2 $\propto CL_{HF}^3/{L_{flame}}^2$ a valid Ri-based empirical heat flux function seems to be a promising way to evaluate the local heat flux and therefore to evaluate the spread rate of a convection-dominated flame under varying flow TIs.

3.4.5 Discussion

The effect of freestream turbulence on reacting boundary-layer flames was generally observed to be similar to effects previously seen in non-reactive boundary-layer flows [82]. A unique feature which differentiates this study from previous research is that multiple sources of instabilities, such as pre-existing velocity disturbances, flame-induced buoyancy, and freestream turbulence, were introduced and analyzed separately. The pre-existing velocity disturbance governs the initial length scales of coherent flame streaks if the boundary-layer can sufficiently develop before reaching

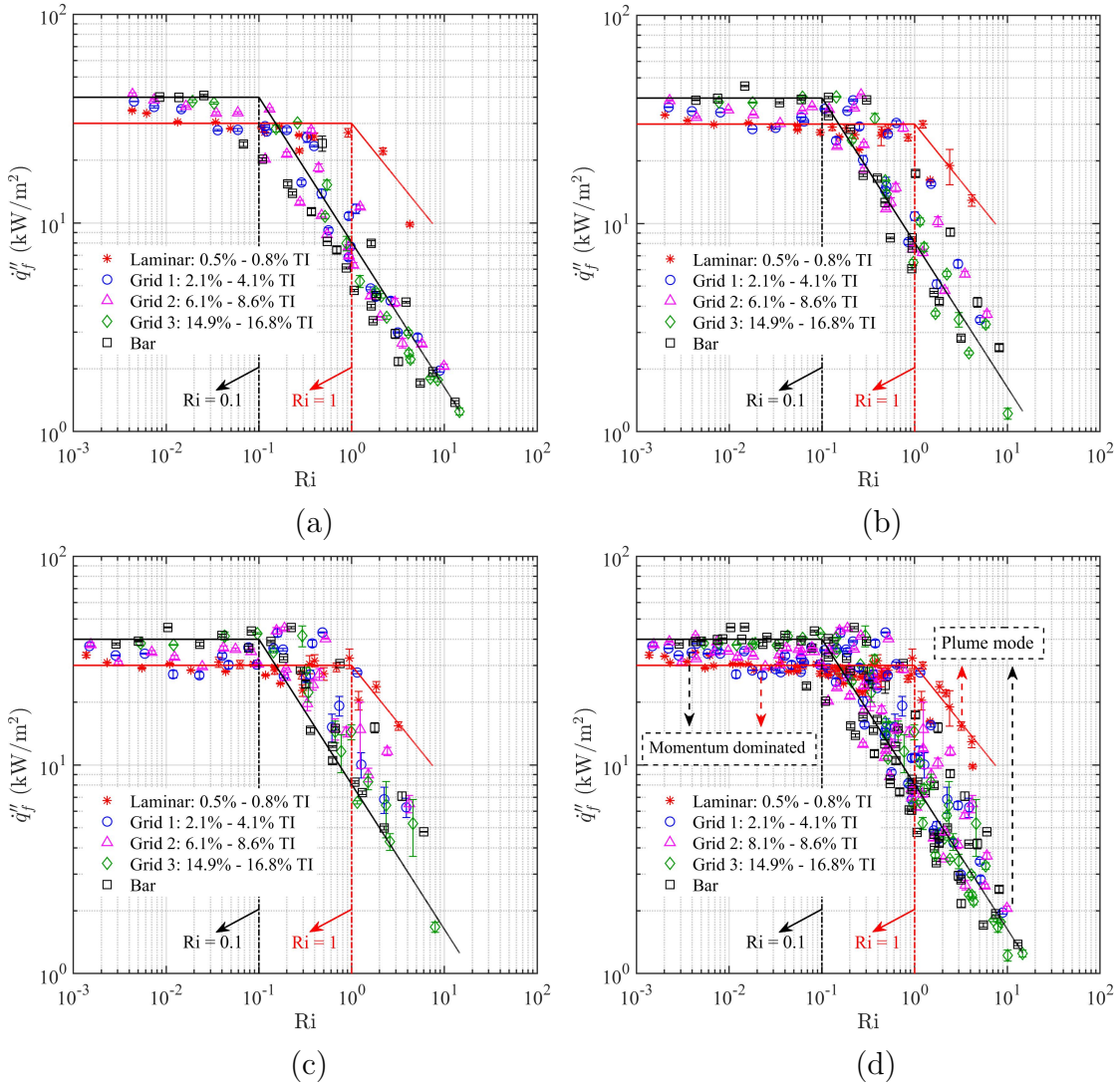

Figure 3.30: Heat flux distribution vs. Ri for different flow turbulence intensities: (a) 5.0 kW HRR, (b) 7.5 kW HRR, (c) 10 kW HRR and (d) combination of all HRRs.

the flame. Meanwhile, the initial streak spacing, which is less likely to be modified by the flame buoyancy, is positively related to the local boundary-layer thickness; this finding is in agreement with previous findings from the same group [31, 32]. Buoyant instabilities had a very weak effect on changing the spatial size of coherent streaks, similar to what has been observed in studies over a heated plate [32, 105] and inclined fires [106]. A possible explanation is that flow momentum dominates

over buoyancy from the flame under mixed convection, especially for fires with a limited heating length. Nevertheless, it is still possible that the local fire dynamics can be dominated by a buoyancy-induced instability, such as a canopy fire located in a large-scale wind-driven wildland fire [107]. Adding turbulence into the freestream emulates what a fire usually faces in a natural environment. Significant instability was triggered by freestream turbulence so that the transition to turbulence occurred early, which further affected the overall flame heating dynamics. Results from this study have highlighted the role of turbulence on modifying both the local and average properties of the flame. Future experiments with different types of fuels, e.g., discrete fuels, are necessary to extrapolate the proposed instability mechanisms to real-world fire scenarios.

3.5 Conclusion

The effect of freestream turbulence on both the physical and thermal structure of a stationary boundary-layer diffusion flame has been examined in this work. The results show that turbulence in the freestream promotes the formation and growth of coherent flame streaks in a boundary-layer flame, destabilizes streamwise vortex rolls, and eventually leads to a transition to turbulence. The growth profile of the mean streak spacing transitions from a linear to a quadratic function along an increasing turbulence intensity. A similar non-linear growth was observed with the mean streak fluctuation versus the Taylor microscale Reynolds number of the flow. Scaling analyses show that the size of coherent flame streaks is proportional to the

incoming boundary-layer thickness but are not always confined within it. The disturbances that freestream turbulence provides lead to significant growth of the streak spacing, which is much larger than the laminar boundary-layer thickness. These results indicate that, for a limited heating length, freestream turbulence plays a more prominent role on boundary-layer flame instability development than buoyancy or the pre-existing Reynolds shear stresses.

Increasing the freestream turbulence leads to a transition to turbulence of the overall flow, resulting in a shorter flame attachment length. A non-dimensional relationship has been proposed to correlate the flame attachment length using the Froude number (Fr), non-dimensional heat release rate (Q^*), and flow turbulence intensity $(1 - \mathrm{TI})^3$. Freestream turbulence redistributed flame streaks, widened the high heat flux flame trough, and ultimately increased the heat flux from flame to the downstream surface. Significant heat flux enhancement was measured when the flame changed from a laminar to a nearly turbulent state triggered by different levels of freestream turbulence. Two different heating modes, a momentum dominated mode and plume mode, have been observed and found to be separated by a critical Richardson number. This critical Richardson number changed from 1.0 to 0.1 when the flame transitioned from a laminar to a nearly fully developed turbulent state.

Finally, similar coherent streaky structures and overall thermal structures were observed at both the highest flow turbulence intensity and bar conditions, suggesting a simple, small-scale, turbulent boundary-layer flame that is reproducible in the laboratory. This configuration might be desirable for small-scale numerical validation studies where the prediction of transition to turbulence has a high degree of

uncertainty. Results from this work serve as a first step to quantify the effects of freestream turbulence on a small-scale boundary-layer flame. The flow turbulence intensity provides a quantifiable and controllable input parameter for boundary-layer flame instability analysis. It is our hope that the turbulence information of the flow together with the collected coherent streak size and flame thermal structure data can provide a database for future fire model evaluation.

Chapter 4: Inclined fire experiment

4.1 Introduction

Fire spread over inclined topography is prevalent in wildland fires. Under such circumstances, fires tend to bend toward the uphill surface, mostly due to a combination of buoyancy-induced flow and a 'blockage' effect between the flame and downstream surface [108]. A closer flame downstream often leads to enhanced heat transfer between the flame and adjacent fuels, thus accelerating the rate of fire spread. As a consequence, fire spreads rapidly uphill, resulting in numerous firefighter fatalities and injuries around the world [109–111]. Evaluation of uphill spread as well as general fire behavior modeling requires an optimized prediction of inclined fire spread, which is an inherently acceleratory process determined by an intrinsic coupling between slope, fire size, local flow, etc. While correlations for fire spread rates have existed since the 1970's [112], physical relationships that describe this coupling and enable prediction of unsteady fire spread rates are not yet developed.

Previous works studying inclined fires can be categorized into those focused on defining a critical angle for fire spread acceleration [113–120], description of the flow field [30,121,122], and characterization of downstream heat transfer [20,118,123,124].

The critical angle is often defined as the slope above which the visible flame appears to be 'pushed' or 'attached' to the downstream inclined surface. It varies from 16° to 27° among different experiments and simulations (see Fig. 4.1a). The presence of sidewalls, which restrict side air entrainment, significantly enhances downstream attachment of flames. For tests without sidewalls, the critical angle falls into a narrower range from 16° to 20° and likely depends upon the width of the flame front. This angle serves as an important indicator for inclined fires since both the flow field and flame spread rate change drastically at this point. Dold et al. [121] tracked this fire-induced flow by releasing soap bubbles ahead of an inclined fire front, finding that a slope higher than 25° resulted in an attached air flow and acceleratory (termed 'eruptive') fire spread. Morandini et al. [30] examined the flow field surrounding a fire spreading along excelsior at a 30° angle using particle image velocimetry, measuring a horizontal flow velocity up to 1.7 m/s ahead of the fire front (0.05 m above the inclined surface). In a later work [30], they conducted velocity and heat flux measurements on a large-scale excelsior bed, confirming the existence of significant convective heating associated with the attached inclined fire. The region over which a flame attaches to the downstream surface is defined as the flame attachment length. Significant increases in the flame attachment length have been reported [113, 118, 119] when the critical angle is reached or exceeded. The flame spread rate accelerates [116, 123, 125, 126] (see Fig. 4.1b) due to an elongated flame attachment length and an associated higher heat flux. These results have illuminated the mechanisms governing spread of inclined fires; however, a predictive model that combines all these aspects is lacking.

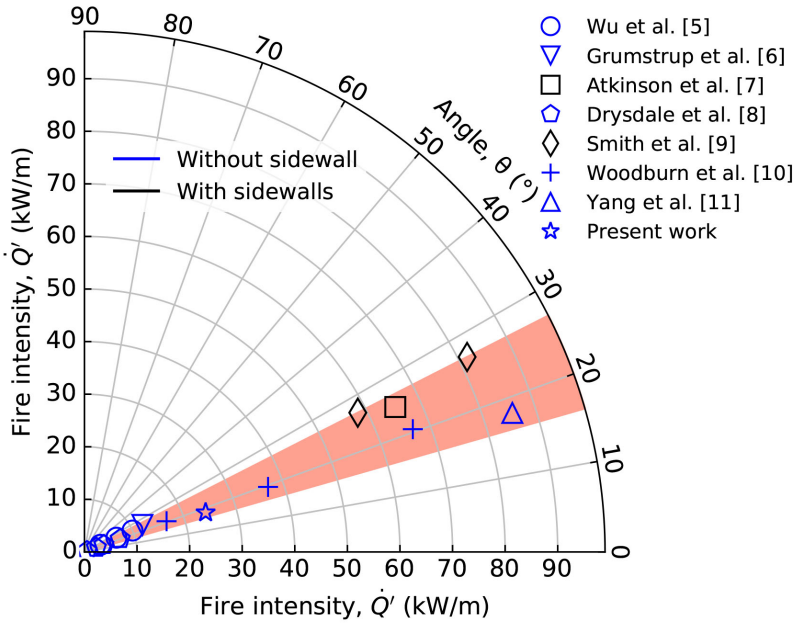

(a)

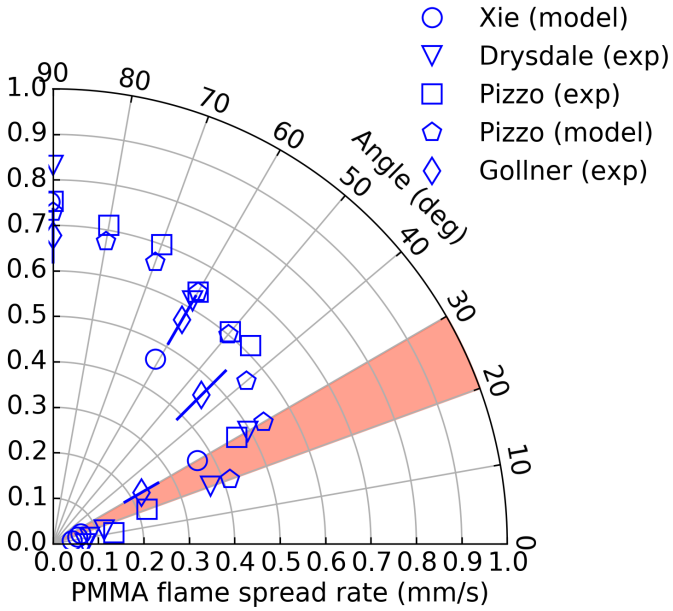

(b)

Figure 4.1: (a) A statistic of critical angles found experimentally and numerically under different fire intensities and (b) dependence of the rate of flame spread (PMMA) on the inclination angle of the fuel surface.

Multiple models have been developed that describe flame spread over an inclined surface, but most are empirically derived. Rothermel's fire spread model [127, 128], is most notable, as one of the most popular operational wildland fire

models, describing the effect of slope on flame spread using an empirical factor. However, this steady-state formulation does not explicitly account for heat transfer processes and thus the convective heating during flame attachment in uphill fire spread and acceleration. Recent results [6, 19, 26, 129] have shown that convective heating is responsible for igniting fine fuel particles that are effectively cooled by ambient air in natural and forced convection to prevent pyrolysis and ignition until direct flame contact occurs. This points out the general importance of understanding the convective environment for heating and cooling of fine fuel materials in fire spread. Liu et al. [130] developed an inclined fire model using a linear flame front based on heat transfer analysis, obtaining good agreement between the model prediction and the measured rate of fire spread. However, description of the local flow was obtained using a Rayleigh number correlation, which hasn't been evaluated for inclined fires. Nor was the convective heating associated with the fire-induced flow was not considered, which added another degree of uncertainty. A later work by Yuan et al. [131] found that better prediction results were achieved by increasing the convection heat transfer coefficient, which reinforces the importance of fire-induced convection in fuel heating. Consideration of the local flow and flame intermittency is then necessary for the precise prediction of convective heat transfer process. Most of the related research focused on purely buoyant flames and wind-driven flames on flat surfaces, leaving a gap in the understanding of dynamics of inclined fires. Recently, Finney et al. [132] using linear regression to characterize the temperature profile and flame intermittency experienced by fuels adjacent to inclined fires. Their results show that the model prediction agrees with the data from spreading fires in

laboratory and field experiments, suggesting general scalability of predictions for characterizing convective heat transfer ahead of linear flame zones. However, the local flow velocity was not part of the model, therefore local convection heat transfer for an arbitrary fuel element cannot be calculated.

This study seeks to explore the fundamental relationships that govern the coupling effect among slope, fire intensity and fire-induced flow. A systematic investigation was conducted using the temperature dataset taken from the USDA Forest Service Missoula Fire Sciences Lab. The dataset was generated across a range of slopes (0° to 30°) and heat release rates (10 kW to 2.25 MW) to ensure general scalability. Meanwhile, this study is in alignment with the works by Finney et al. [132], aiming to provide additional flow velocity measurements for the flame characteristics of a stationary line fire. Using cross-correlation velocimetry, the local flow velocity was derived from the temporal temperature profiles of a thermocouple array. Finally, non-dimensional analysis was carried out to develop generalized relationships for inclined fires.

4.2 Experimental methods

4.2.1 Small tilt table

Two experiments were conducted at the USDA Forest Service Missoula Fire Sciences Lab. The first was a small-scale inclined fire experiment, as illustrated in Fig. 4.2a. Both qualitative observations and quantitative measurements were made to understand the inclined fire and plume behavior. A propane flame was

generated over a tilt table with a 1.22 × 1.22 m^2 surface area, which was made from ceramic fiber insulation board (Super Firetemp). The angle of the tilt table was adjusted from 0° to 30°. The motion of the hot plume, associated with gas density variations caused by temperature differences, was visualized using a retroreflective shadowgraph technique [133]. The shadowgraph setup consisted of a light source, a camera, and a screen on which to cast a shadow. A LED light source was mounted next to a digital camera and focused on a 45° rod mirror mounted at the center of the camera lens. Such arrangement allowed for a coincident illumination of the fire plume, thus avoiding a double shadow in the shadowgraph image. A 3 × 3 m^2 vertical retroreflective screen was mounted flat against a metal frame approximately 12 m away from the digital camera. To avoid over-ranging the camera sensor with luminous flames, a partially premixed propane flame was employed to reduce the soot yield. A propane flow with a 6.6 standard liters per minute (SLPM) flow rate and a 57 SLPM air flow (equivalence ratio $\phi = 2.2$) were fed to a sand burner with a 0.50 × 0.09 m^2 burning area, producing a 10 kW flame. To track the direction of the downstream flow, four low-speed helium jets were injected along the table centerline at a 10 cm interval. The first helium jet was introduced at 16 cm downstream of the burner trailing edge. These helium jets are visible in the shadowgraph images because of the index of refraction difference between the helium and the ambient air.

Along with the shadowgraph observation, temperature measurements were conducted to further the understanding of the visual results. Temperatures were measured using an array of 21 fine-wire thermocouples (50 μm wire diameter, type-

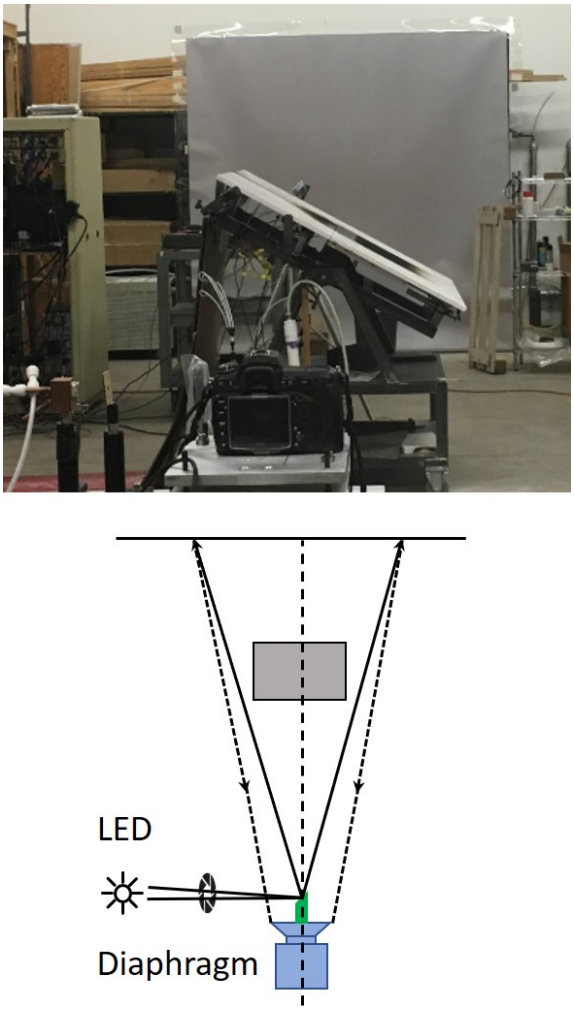

Figure 4.2: Small tilt table with shadow-graph setup

K) mounted along the table centerline. Each thermocouple bead was elevated ~ 8.5 mm height above the table surface. Thermocouple spacing was 0.0125 m for the first 0.163 m, 0.025 m for the next 0.15 m, and then 0.05 m out to 0.1 m. Temperatures of the small-scale experiments were recorded at 500 Hz for 10 seconds using a National Instruments SXCI data acquisition system.

4.2.2 Large tilt table

To scale up the small-scale findings, large-scale experiments were conducted on a 3.66 $\times$ 6.10 m^2 tilt table, as shown in Fig. 4.3. Surface of the table is made from ceramic fiber insulation board (Super Firetemp). Slopes of the table were maintained at 6°, 12°, 18°, 21°, 24° and 30°. Propane diffusion flames were produced using a modular sand burner with heat release rates (HHRs) ranging from 81 kW to 2.25 MW. The total area of the burner is 3.66 $\times$ 1.22 m^2, which is partitioned into 48 equal sections with a 0.61 $\times$ 0.15 m^2 cell size. Propane was supplied to each section of the burner through independently controlled solenoid ball valves exiting a common manifold. Such design allows for the controlling of burner surface area and aspect ratios ($\alpha = L/D$) by opening one or more valves, as summarized in Table. 4.1. Flow of propane gas to the manifold was regulated using a mass flow controller (Omega Model FMA-2612A). For each burner length, the gas flow rates were adjusted to maintain constant fire intensities (Q'). Streamwise temperatures were measured using a linear array of 63 fine-wire thermocouples (50 μm wire diameter, type-K) elevated ~8.5 mm height above the table surface. Spacing between the thermocouples was at 0.02 m for the first 0.76 m and 0.04 m out to 1 m. Temperatures were recorded at 500 Hz for 90 seconds using a National Instruments SXCI data acquisition system. Side-view video of the inclined fire was recorded by a Nikon digital SLR camera (D700) with 1920 $\times$ 1080 resolutions. Systematic video/image recording was not taken according to the experimental design, and thus no data was generated from image processing. The experiment was performed at the USFS Mis-

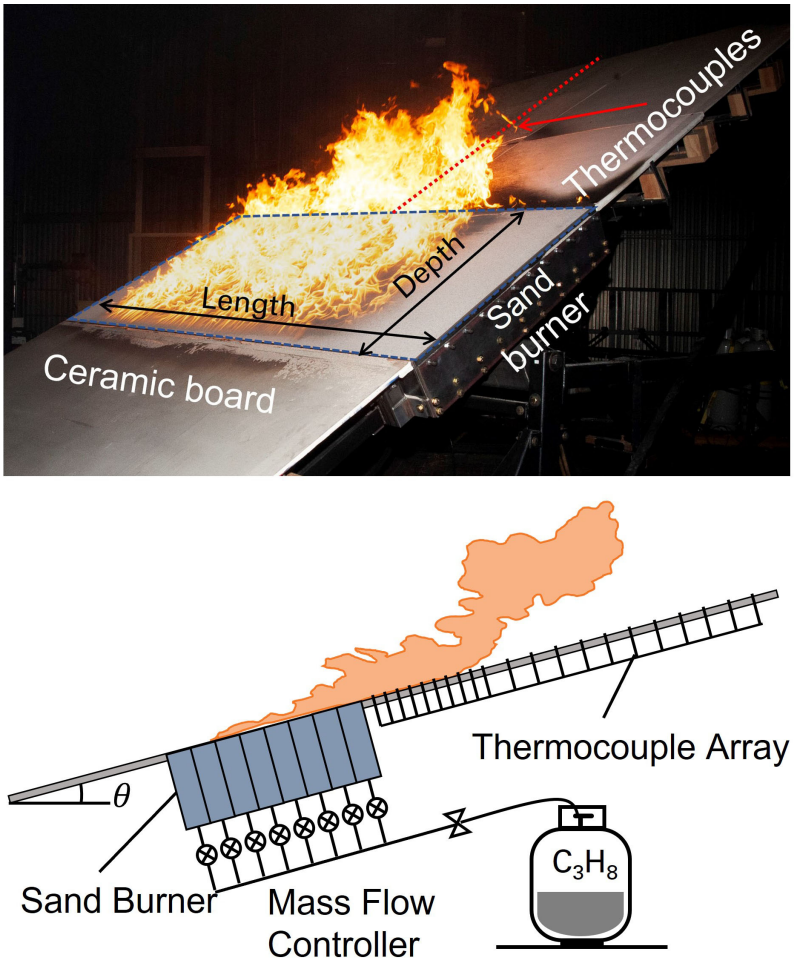

Figure 4.3: Large tilt table

soula Fire Sciences Laboratory and supported by their staff: Josh Deering, Andrew Gorris, Jon Bergroos, and Randy Pryhorocki.

4.3 Cross-correlation velocimetry

The measurement of a two-dimensional velocity flow field in a turbulent flame can be accomplished with particle image velocimetry (PIV). However, the challenge of introducing suitable tracer particles and the need for a very intense laser light sheet over the measurement section [30] make practical implementation of the PIV

Table 4.1: Experimental conditions for the small and large tilt tables.

Table	Fireline Intensity, Q' [kW/m]	Angle, θ [°]	Burner Length, L, [m]	Burner Depth, D, [m]	Aspect ratio, α
Small	20	12, 14, 16, 18, 20, 22, 24, 26, 28	0.5	0.09	5.6
Large	82, 123, 243, 369, 492, 615	6, 12, 18, 21, 24, 30	1.83, 2.44, 3.66	0.3, 0.61, 0.91, 1.22	1.5 to 12

technique difficult. In this study, we measured the flow velocity using a cross-correlation velocimetry (CCV) technique based on the signals of a thermocouple array along a surface downstream of the burner. In principle, cross-correlation velocimetry is based on Taylor's 'frozen eddy' hypothesis [134] for turbulent flows. In Taylor's hypothesis, eddies in a turbulent flow are considered to retain their shape and characteristic, i.e., 'frozen eddy', for a limited time over a given space. If these eddy structures can be identified and traced, then the mean velocity of the flow can be estimated as the weighted average velocities of the eddies [135, 136]. For flows with a dominant velocity component, such as a turbulent flame, a slug of fluid at a specific temperature or an eddy structure can be traced using the temperature signal. When the spacing of the temperature sensors, d, is within the characteristic length of the flow, the eddy structures can be treated as being frozen. For example, Fig. 4.4a displays the measured temperature fluctuations by a pair of thermocouples (1 and 2) with a d = 0.02 m spacing. While some discrepancy exists between two signals owing to the nature of the turbulent flow, overall, the two signals are similar to each other but with a time lag. The time lag, τ, defined as the traveling time of the local flow feature from thermocouple 1 to thermocouple 2, is calculated using a

cross-correlation function. The cross-correlation [137] between a pair of temperature signals over a finite time is defined as follows:

$$R_{T_1'T_2'}(\tau) = \frac{1}{t_s}\int_0^{t_s} T_1'(t)T_2'(t+\tau)dt \tag{4.1}$$

where T_1' and T_2' are the fluctuating components of the temperature data (i.e., $T' = T - \overline{T}$)) and t_s is the sampling time. To minimize the effect of amplitude variations of the temperature fluctuations, a normalized coefficient of the cross-correlation, $\rho_{T_1'T_2'}$, was further calculated using Eq. 4.2

$$\rho_{T_1'T_2'}(\tau) = \frac{R_{T_1'T_2'}(\tau)}{\sqrt{R_{T_1'T_1'}(0)R_{T_2'T_2'}(0)}} \tag{4.2}$$

For signals displayed in Fig. 4.4a, a $\tau = 0.0214$ s was identified at the peak coefficient of the correlation, which is displayed in Fig. 4.4b. Note that a time resolution higher than 0.002 s (1/500, where 500 is the sampling frequency) was achieved using a subsample interpolation method similar to sub-pixel estimation in PIV [138] (see Appendix B). Shifting the signal of the thermocouple 2 for 0.0214 s, we can see that most of the peaks and troughs of the two temperature signals align to each other, indicating a good estimation of τ.

To ensure an optimal time delay (τ), the temperature signals were evaluated with a 3 s sampling window (1500 data points) for the attached flame region. As for the detached flame region, where weaker temperature fluctuations were detected, a 6 s sampling window (3000 data points) was used. Meanwhile, a 0.5 threshold

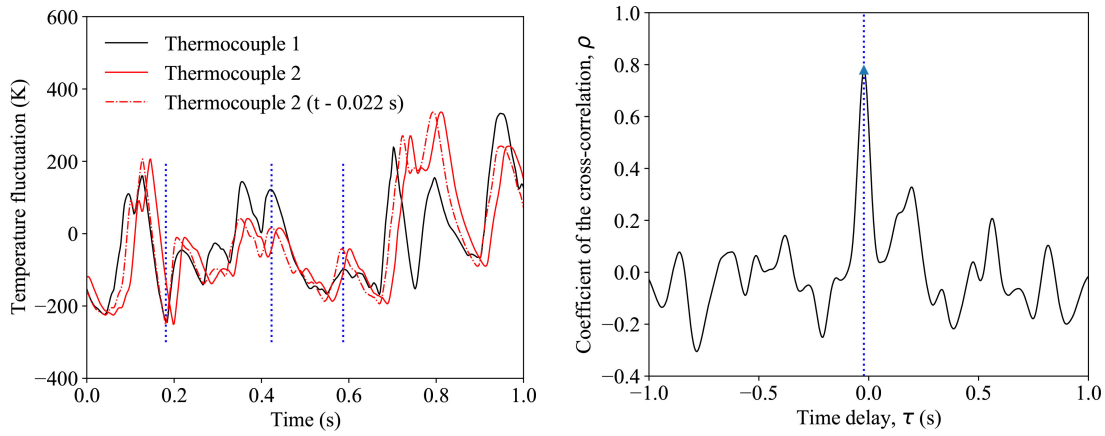

(a) (b)

Figure 4.4: (a) Temperature signals of thermocouple #1 and #2 and (b) normalized coefficient of the cross-correlation between temperature signal #1 and #2.

was set for the cross-correlation coefficient (ρ >0.5) to ensure the similarity of the temperature signals. Velocity of the flow at a given time stamp is then calculated as

$$U = d/\tau \tag{4.3}$$

It is apparent from Eq. 4.3 that the thermocouple based cross-correlation velocimetry technique is subject to errors associated with d and τ. Spacing between thermocouple beads, d, was found to be affected by uncertainty in positioning of the thermocouples and heat-induced distortion of the thermocouple wire. A standard deviation up to 18% was measured for the part of the thermocouple array 2 cm spacing. To suppress such error, signals from thermocouples contained within an 8 cm distance was used to calculate the averaged local flow velocities, which limited the error to less than 4.5%. On the other hand, the 8 cm distance is still less than the integral length of the flame, thus ensuring the overall applicability of the cross-correlation. Estimation of the integral length scale can be found in the Appendix B.

Meanwhile, precision of τ was improved by locating the peak ρ using the subsample interpolation method, thus limiting the associated error. Details can be found in the Appendix B. During the test, soot deposition occurred on the thermocouple bead, which could cause additional error to the CCV technique. To mitigate such error, soot was cleaned before each test. The current data processing did not account for the soot deposition effect.

By treating the sampling time as a sliding window, temporal variations of τ and U were captured. Figure 4.5a displays the results obtained at x= 30 cm for a 246 kW/m fire with a 24° angle. A mean velocity of 1.29 m/s was measured with a 0.24 m/s root-mean square velocity fluctuation. Note that such fluctuation only reflects part of the turbulent fluctuations since the velocity was smoothed over the spacing between thermocouples. Distribution of the velocity is plotted in Fig. 4.5b. The data appears to take on a lognormal distribution, reflecting the turbulent state of the flow [32]. Additionally, the probability distributions of the flow velocities at various downstream locations were obtained and mapped in Fig. 4.6. These results demonstrated the value of the temperature cross-correlation velocimetry technique. In summary, the long-duration exposure of the thermocouple array in a high temperature environment makes it suited for both temperature and velocity measurements under turbulent flame conditions.

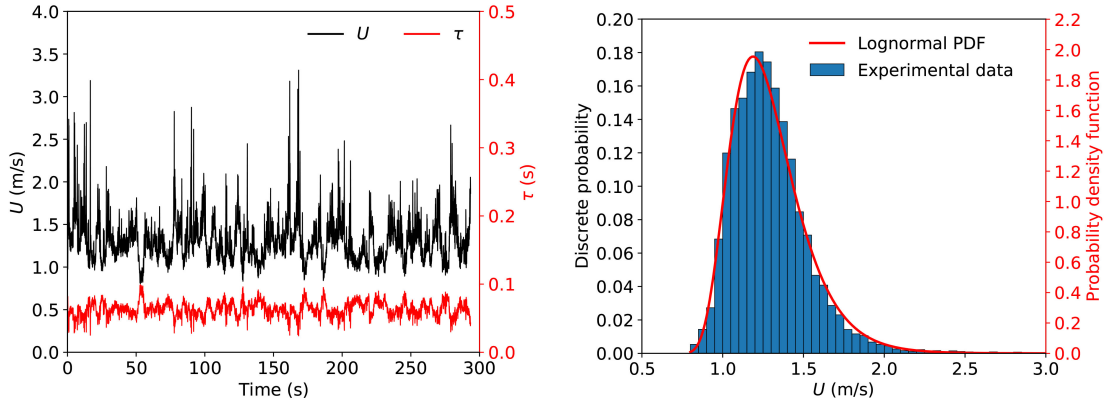

(a) (b)

Figure 4.5: (a) Calculated flow velocity (U) and time delay (τ) vs. time and (b) distribution of the flow velocity (U). Measurements were taken at x= 30 cm for a 246 kW/m fire with a 24° angle (L = 3.66 m, D = 0.61 m). The data was recorded for 300 s for this case.

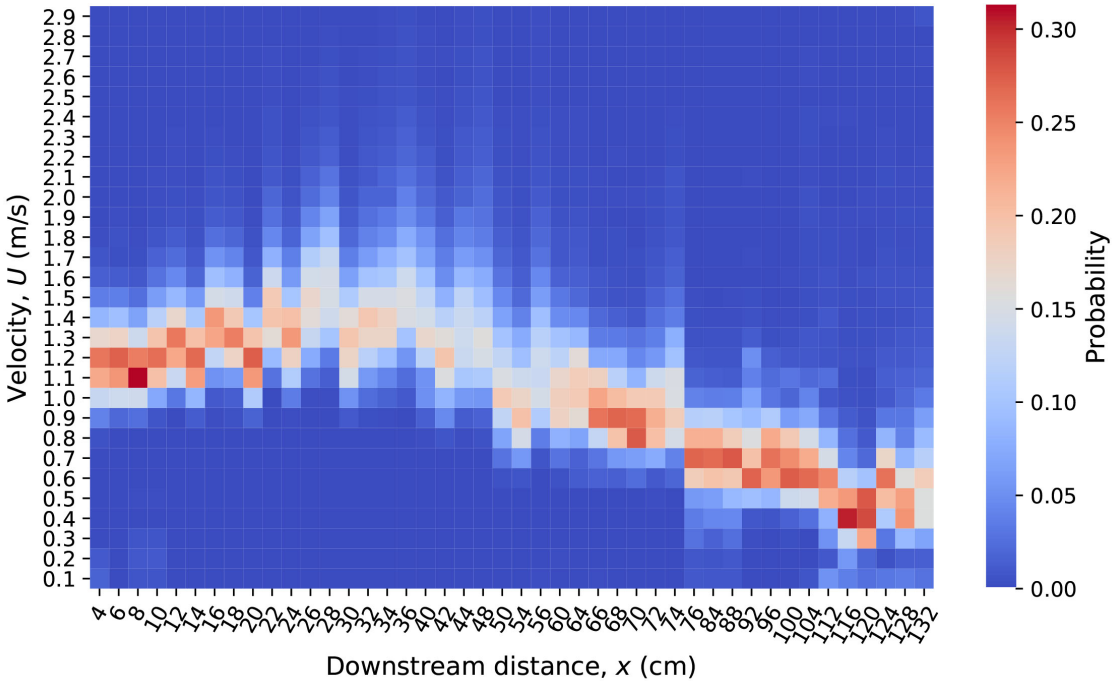

Figure 4.6: 2D heatmap of the velocity probability distributions at different downstream locations (x). Measurements were taken for a 246 kW/m flame with a 24° angle (L = 3.66 m, D = 0.61 m). The data was recorded for 300 s.

4.4 Downstream heating of inclined fires

Heat transfer between the flames and unburned fuels is a key factor in determining rate of fire spread [132]. To characterize the upslope heating by an inclined fire, temperature profiles and flame attachment length were also measured. Scaling analysis was performed to propose generalized relationships for the temperature distribution and flame attachment length

4.4.1 Critical angle

To determine the critical angle, the large tilt table was rotated continuously from $\theta = 0^{\circ}$ to 30°. Figure 4.7 displays a sequence of representative images under different angles of inclination. The flame was observed to tilt toward the upslope direction at $\theta = 6^{\circ}$ but without forward extension. At $\theta = 12^{\circ}$, the flame extended beyond the trailing edge of the burner, but the bulk fire plume remained detached from the surface. While at $\theta = 18^{\circ}$, the majority of the flame was attached to the surface. Such phenomenon becomes more prominent for higher angles of inclination, indicating a critical angle of 18°

4.4.2 Centerline temperature

To examine the slope effect on heating profiles, the mean temperature rise above ambient, ΔT_{mean}, along the downstream centerline array of thermocouples was plotted in Fig. 4.8. log-log scale was used to better illustrate the flames that were attached and detached from the surface. For the smaller table, angles ranging from

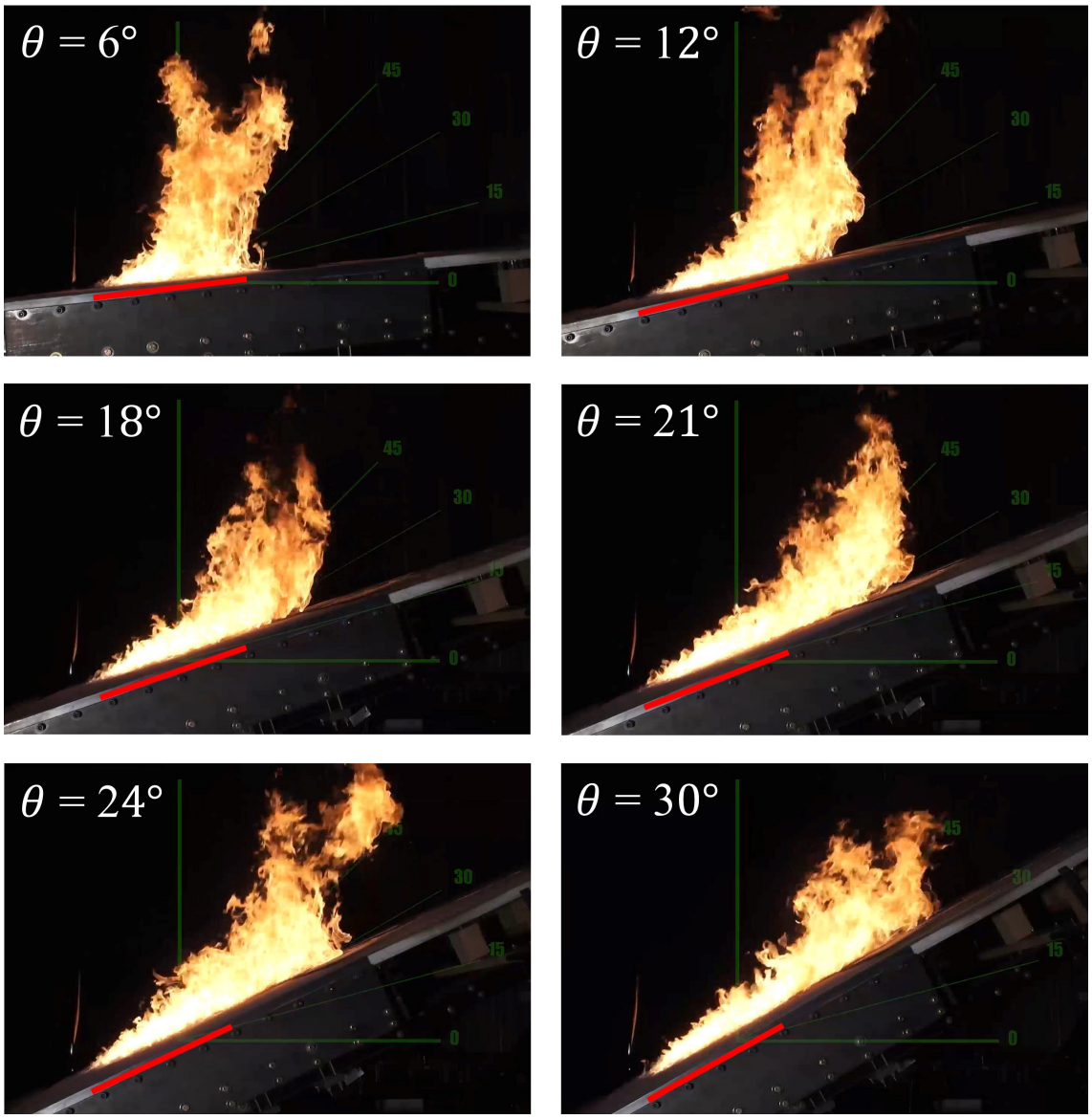

Figure 4.7: Side-views of an inclined fire under different angles. Burner depth (D = 0.61 m) is marked by the red line. Note that the heat release rate was maintained at 750 kW which is a standalone case for demonstration.

12° to 28° with a 2° interval were tested. A short temperature plateau is observed in Fig. 4.8a when the slope increased to 16°. The length of the plateau further increased at 18° but nearly saturated at 20°, indicating a critical angle between 18° and 20° for this flame. Beyond the attached region, the temperature decayed at downstream locations. A slower temperature decay is observed for slopes higher than

20°, which is mostly due to the attached hot plume under higher angles. Similarly, mean temperatures of a large-scale 2.25 MW inclined fire (615 kW/m with a 3.66 m burner length) are displayed in Fig. 4.8b. It is observed that flame attached to the downstream surface when the angle was above 18°, affirming a universal critical angle across different scales. Note that these results did not use sidewalls, limiting the 'trench effect' which resulted in different critical angles in some previous studies [115, 117].

For purely buoyant flames, their vertical centerline temperature has been correlated by McCaffery [62], who used a $Q^{2/5}$ to normalize the flame height. For inclined fires, temperature profiles under attached conditions showed a similar trend, suggesting a possible correlation similar with the buoyant flame. Instead of using $Q^{2/5}$, a flame attachment length, L_f, was used to normalize the downstream distance, x. L_f is defined as the distance between the burner trailing edge and the farthest downstream location with a $\Delta T_{mean} \geq 500$ K, e.g., $T_{mean} \geq 793$ K. Figure 4.9 displays the processed data at an 18° slope with a 3.66 m burner length. Results show that the proposed normalization, x/L_f, collapsed the temperature data for various burner depths and heat release rates. To present the data concisely, a gaussian function was selected to fit the temperature data with x/L_f.

Using the gaussian fitting, ΔT_{mean} of all attached flame conditions ($\theta \geq 18°$) was processed and displayed in Fig. 4.10. Temperature data taken from the small title table was not included since the temperature was affected by the premixed flame. Upon plotting ΔT_{mean} versus x/L_f, three regimes immediately become clear, similar to McCaffrey's plume temperature correlation [62]. Exponents representing

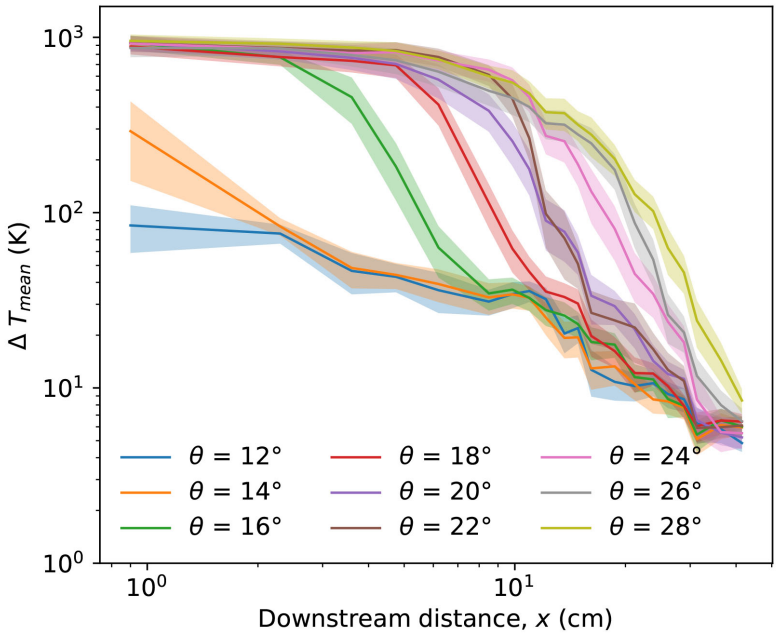

(a)

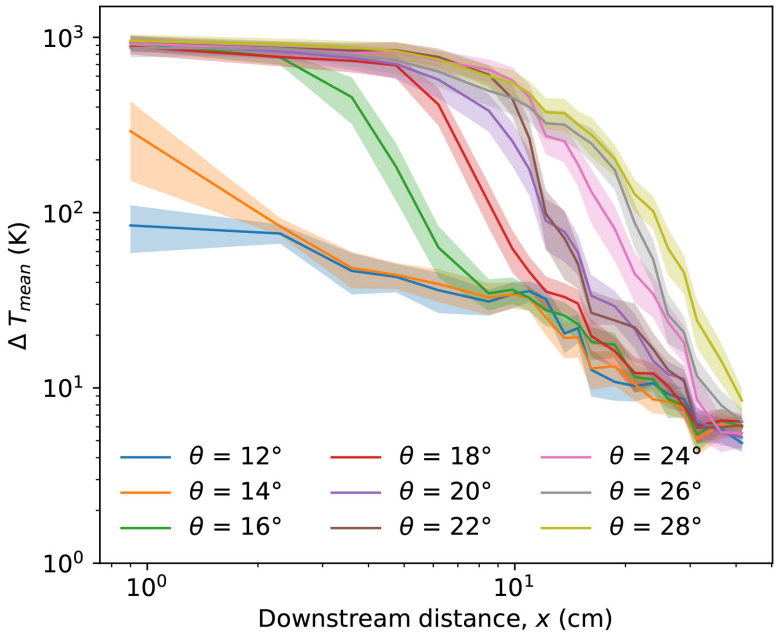

(b)

Figure 4.8: Mean temperature rise vs. centerline downstream locations: (a) small tilt table tests with a 20 kW/m fire intensity, (b) large tilt table tests with a 615 kW/m fire intensity (L = 3.66 m, D = 0.30 m). The shaded area represents 1/2 of the standard deviation.

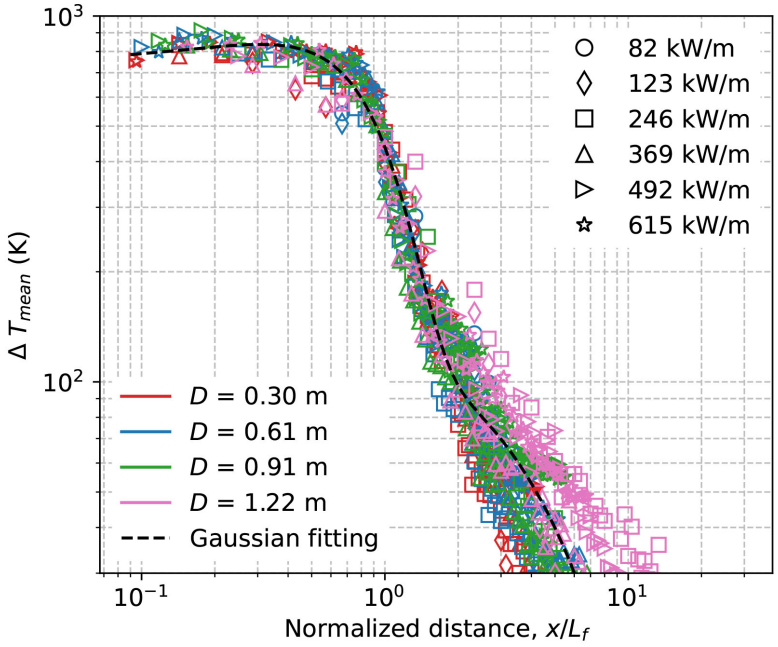

Figure 4.9: Mean temperature rise (ΔT_{mean}) vs. normalized downstream distance (x/L_f). The data was taken under an 18° slope with a 3.66 m burner length, burner depth ranges from 0.30 to 1.22 m.

the fitting between ΔT_{mean} and x/L_f in different regions were then obtained. Within the continuous flame and intermittent regions, exponents of $\eta = 0$ and $\eta =$ -3/2 have been obtained for ΔT_{mean}, respectively. Within the plume region, a $\eta =$ -2 was found to represent the current temperature trend, but it is observed that the temperature profiles diverged at the plume trailing region, i.e., $\Delta T_{mean} \leq 100$ K. This is expected since the hot plume may not be attached to the downstream surface at lower angles. In comparison, McCaffrey's temperature correlation for vertical buoyant flames has shown lower absolute exponents within the intermittent and plume regions, which are $\eta =$ -1 and $\eta =$ -5/3, respectively. Exponents in the intermittent region were recently reported by Finney et al. [132] to vary from about -1/2 to -3/2 adjacent to burner flames when subjected to varying winds, slopes, and burner dimensions.

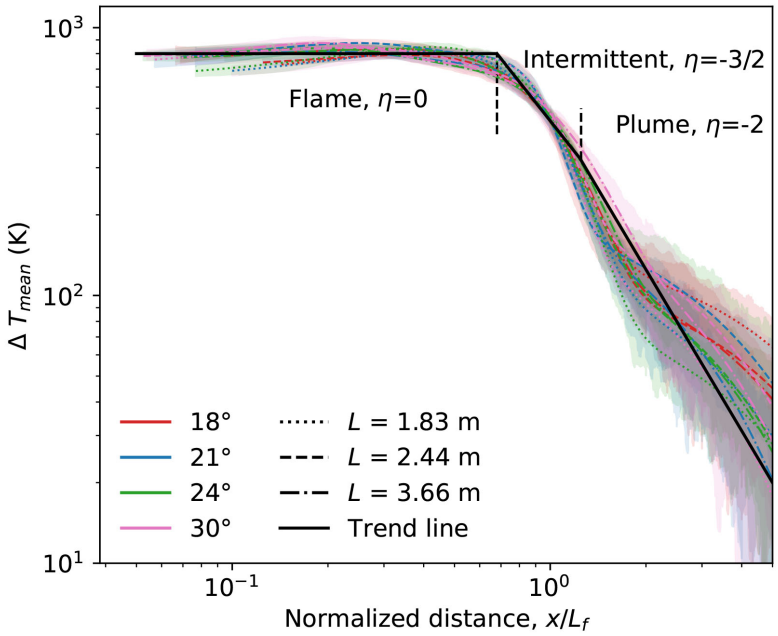

Figure 4.10: Mean temperature rise vs. normalized downstream distance with $\theta \geq 18°$.

Unlike the vertical buoyant flame, which is driven by coaxial buoyancy , the inclined fire is driven by buoyant forces parallel with the inclined surface and normal to the surface [139]. Even though the flame is attached to the surface, the hot plume can be detached due to the normal buoyant force [140], resulting in a faster temperature decay and larger deviations at the plume region. Nevertheless, the overall results show that the centerline temperatures under attached flame conditions are similar to McCaffrey's buoyant flame temperature correlation, suggesting an effective way of correlating the heating profile for inclined fires.

4.4.3 Flame attachment

Once the slope exceeds the critical angle, the flame starts to attach to the inclined surface. The region over which the flame directly impinges on the surface is

defined as the flame attachment length (also known as flame drag/extension length). To determine the length of the flame attachment, intermittency of the flame appearance was obtained by tallying the relative frequency of instantaneous temperature records exceeding 793 K (i.e., at ΔT_{mean}= 500 K). The 793 K threshold was selected since it corresponds to the nominal lower temperature bound for visible thermal radiation emissions from soot in flames [141, 142]. Figure 4.11 displays an overview of flame intermittency for different fire intensities and burner depths under a 30° angle of inclination. An intermittency of 0.5 was used to determine the length of the flame attachment (marked by a white lines). Results show that a wider burner depth leads to a shorter flame attachment length, which is attributed to several factors including increased consumption of fuel within the burner and enhanced entrainment into the flame zone along the lateral edges of the burner [132]. Meanwhile, a larger fire intensity is observed to contribute to a longer flame attachment length.

To further explore the relationships between the slope, fire intensity and flame attachment length, we plotted the data in Figs. 4.12 and 4.13. Fig. 4.12a shows that a larger angle leads to a longer flame attachment length, L_f. In a previous work by Finney et al. [132], the slope factor was treated as $sin^2 2\theta$. We adopted the same method, finding that $sin^2 2\theta$ works well for the current data, as displayed in Fig. 4.12b. Although L_f shows a linear trend with both θ and $sin^2 2\theta$, the latter is suitable for scaling analysis. For a fixed fire intensity, discrepancies in L_f exists among different burner lengths at lower angles, but this effect gradually fades away as angle increases. A possible reason is that the side entrainment is stronger at lower angles, resulting in higher uncertainties of L_f. Meanwhile, Fig. 4.13a plots

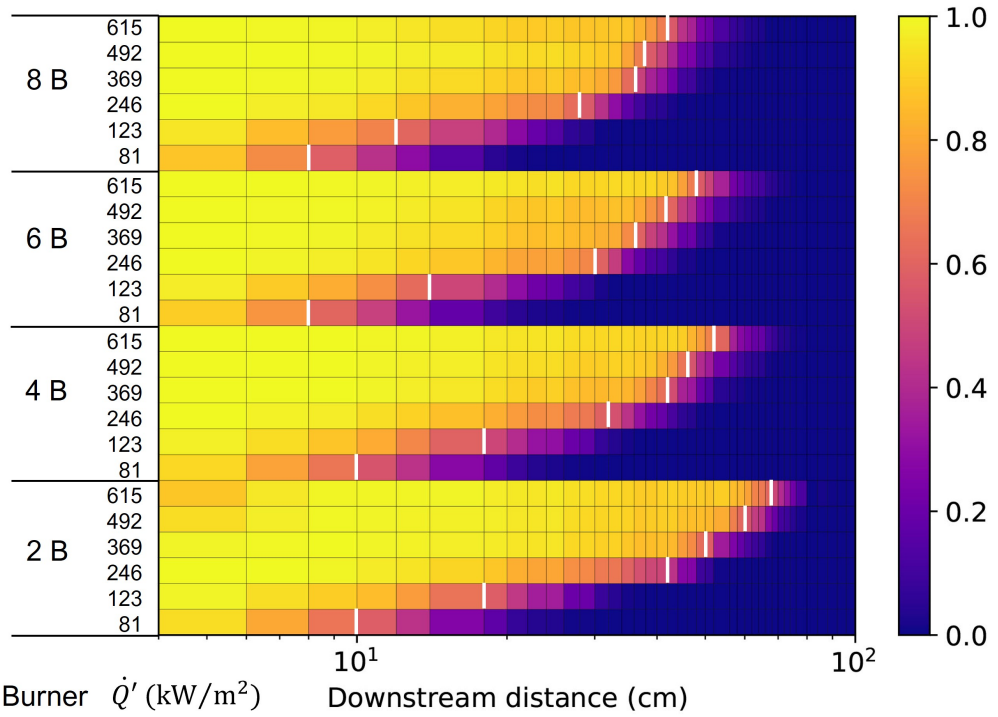

Figure 4.11: Flame intermittency vs. downstream distance under a 30° slope (L = 3.66 m). The white line marks the location with an intermittency of 0.5.

the L_f under different fire intensities. A non-linear trend is observed between $\dot{Q}'$ and L_f. Following work by Quintiere and Grove [102] for vertical line fire plumes, a characteristic plume length scale is given by Eq. 4.4

$$Z = \left[\frac{\dot{Q}'}{\rho_0 c_p T_0 g^{1/2}}\right]^{2/3} \tag{4.4}$$

with $\dot{Q}'$ being the fire intensity, ρ_0 the density, c_p the heat capacity, T_0 the temperature of ambient air, and g the standard acceleration due to gravity. Plot the converted Z in Fig. 4.13b, we observe a linear relationship between Z and L_f. Together with the finding between $sin^2 2\theta$ and L_f, these linear relationships suggest a plausible way of predicting L_f using angle of inclination (θ) and fire intensity ($\dot{Q}'$).

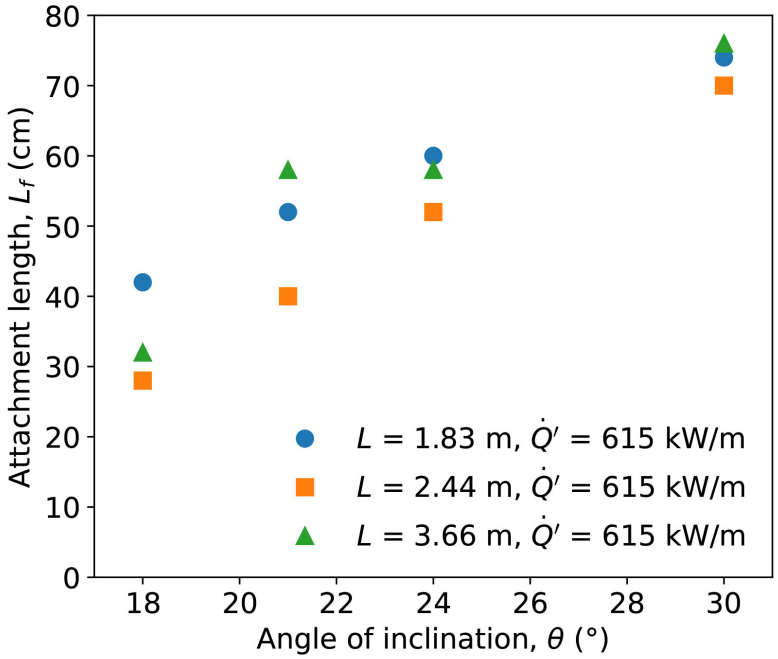

(a)

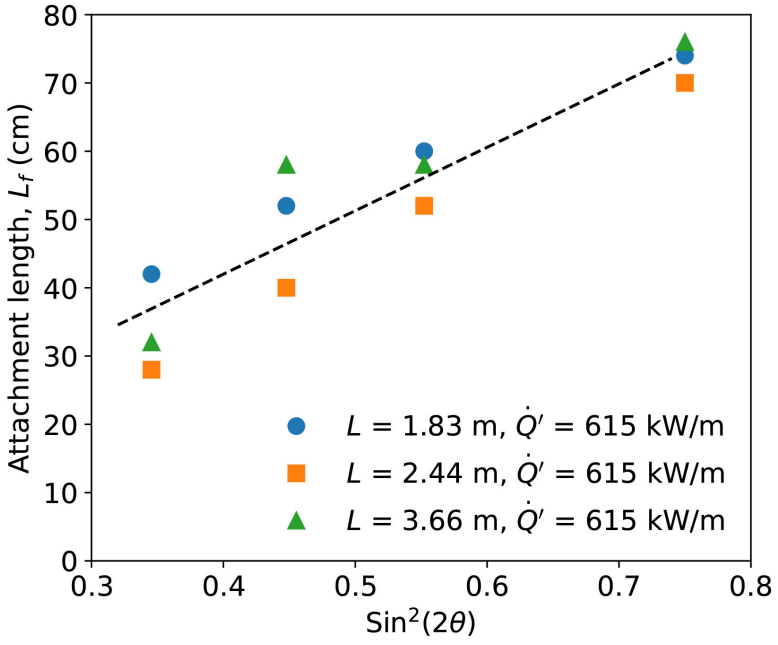

(b)

Figure 4.12: (a) Flame attachment length vs. angle of inclination and (b) Flame attachment length vs. $sin^2 2\theta$

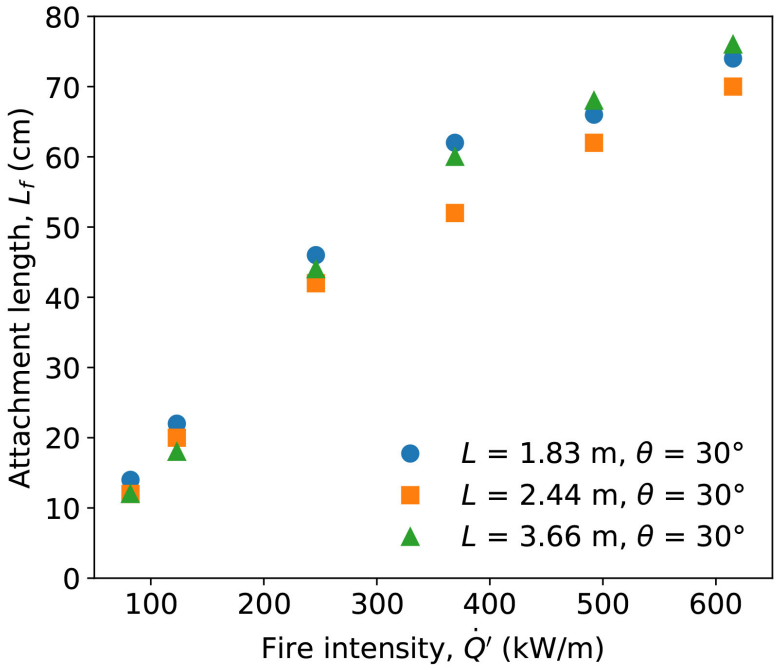

(a)

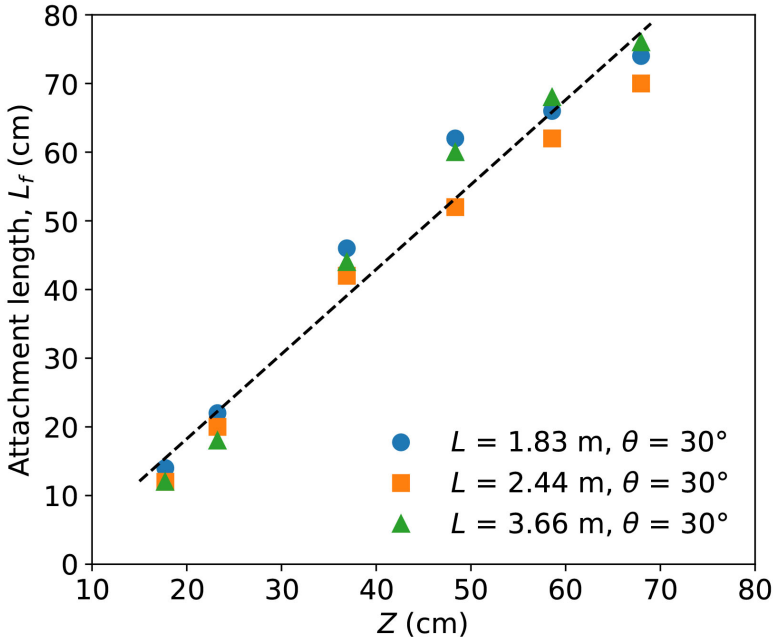

(b)

Figure 4.13: (a) Flame attachment length vs. fire intensity and (b) Flame attachment length vs. Z, with $Z = [\dot{Q}'/\rho_0 c_p T_0 g^{1/2}]^{2/3}$.

With these understandings, we assumed a characteristic flame attachment length, $Zsin^2 2\theta$, for incliend fires. The fire intensity in Eq. 4.4, $\dot{Q}'$, was calculated separately according to the burner aspect ratios, α,

$$\dot{Q}' = \begin{cases} Q/L & \text{if } \alpha \geq 6 \\ Q/[2LD/(L+D)] & \text{if } \alpha < 6 \end{cases} \tag{4.5}$$

When $\alpha \geq 6$, the burner is treated as a line burner with a characteristic length scale of L; while for $\alpha < 6$, the burner depth cannot be ignored, thus having a characteristic length scale of $2LD/(L+D)$, which is equal to its hydraulic diameter [143]. Note that the threshold of $\alpha = 6$ is not necessarily a hard limit but a criterion for a better estimation of the characteristic length of the fire base. Using Eq. 4.5, the characteristic flame length ($Zsin^2 2\theta$) was calculated and displayed in Figs. 13a and 13b. Results show that the measured flame attachment length is linearly related to $Zsin^2 2\theta$, as written in Eq. 4.6

$$L_f = \begin{cases} 1.55Zsin^2 2\theta & \text{if } \alpha \geq 6 \\ 0.72Zsin^2 2\theta & \text{if } \alpha < 6 \end{cases} \tag{4.6}$$

The above analysis shows that the flame attachment length of an inclined fire with no wind can be predicted using angle of inclination and fire intensity. The temperature distribution and the flame attachment length together describe the thermal structure of the inclined fire. However, such information is not enough to characterize the heat transfer between the flame and the combustible material along the downstream

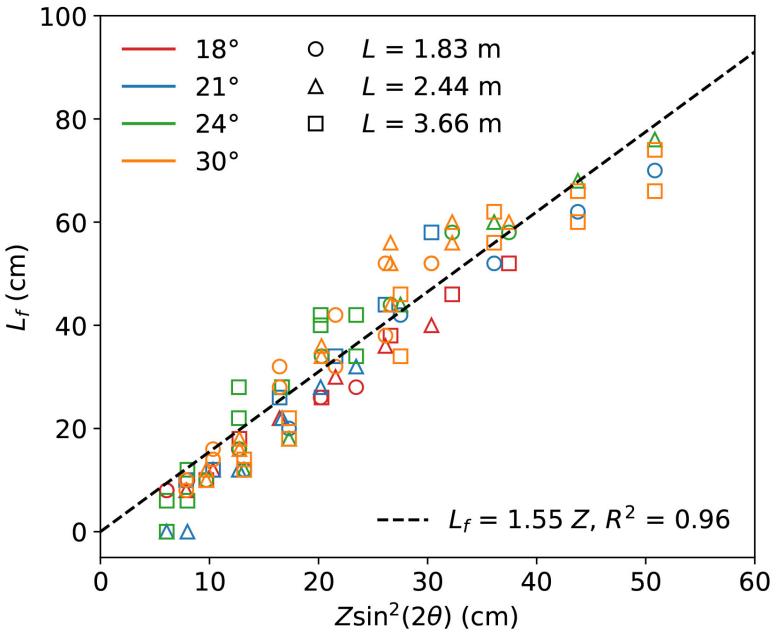

(a)

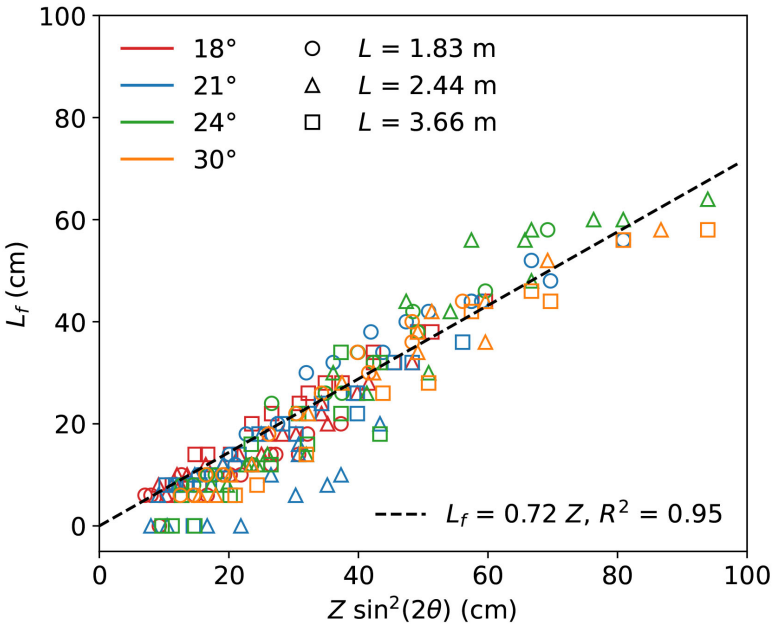

(b)

Figure 4.14: Flame attachment length vs. $Zsin^2 2\theta$: (a) results with burner aspect ratio larger than 6 ($\alpha \geq 6$) and (b) results with burner aspect ratio less than 6 ($\alpha < 6$).

location. For that purpose, the flow velocity is needed.

4.5 Flow dynamics of inclined fires

The flow field of the inclined fires were examined using shadowgraph and cross-correlation velocimetry techniques. Shadowgraph images gave a qualitative understanding of the flow motion which facilitates the theoretical flow dynamics analysis; local flow velocities measured by cross-correlation velocimetry serves as a dataset for the evaluation of the theoretical results.

4.5.1 Flow field of the small-scale inclined fire

To visualize the buoyancy induced flow and the uphill air entrainment, a sequence of shadowgraph images is displayed in Fig. 4.15. Additionally, low-speed helium inlets were injected to illustrate the flow directions under various angles of inclination. At $\theta = 0°$, the left helium inlet bent toward the flame, driven by the entraining air; the three right most inlets were not affected. For a larger angle, at $\theta = 10°$, all four helium inlets bent toward the flame, indicating a stronger local entrainment. At $\theta = 15°$, the farthest right inlet is seen to be pushed away from the flame. This phenomenon became more prominent at $\theta = 20°$, indicating a stronger buoyancy-induced flow along the inclined surface. At an angle of 25°, the flame was nearly fully attached to the surface. The only visible helium inlet on the right bent almost at a 90° angle, driven by the propagating hot plume. Finally, the helium inlets were no longer visible under a 30° slope, where the plume was completely attached to the surface.

Along with the shadowgraph observation, local flow velocities were examined

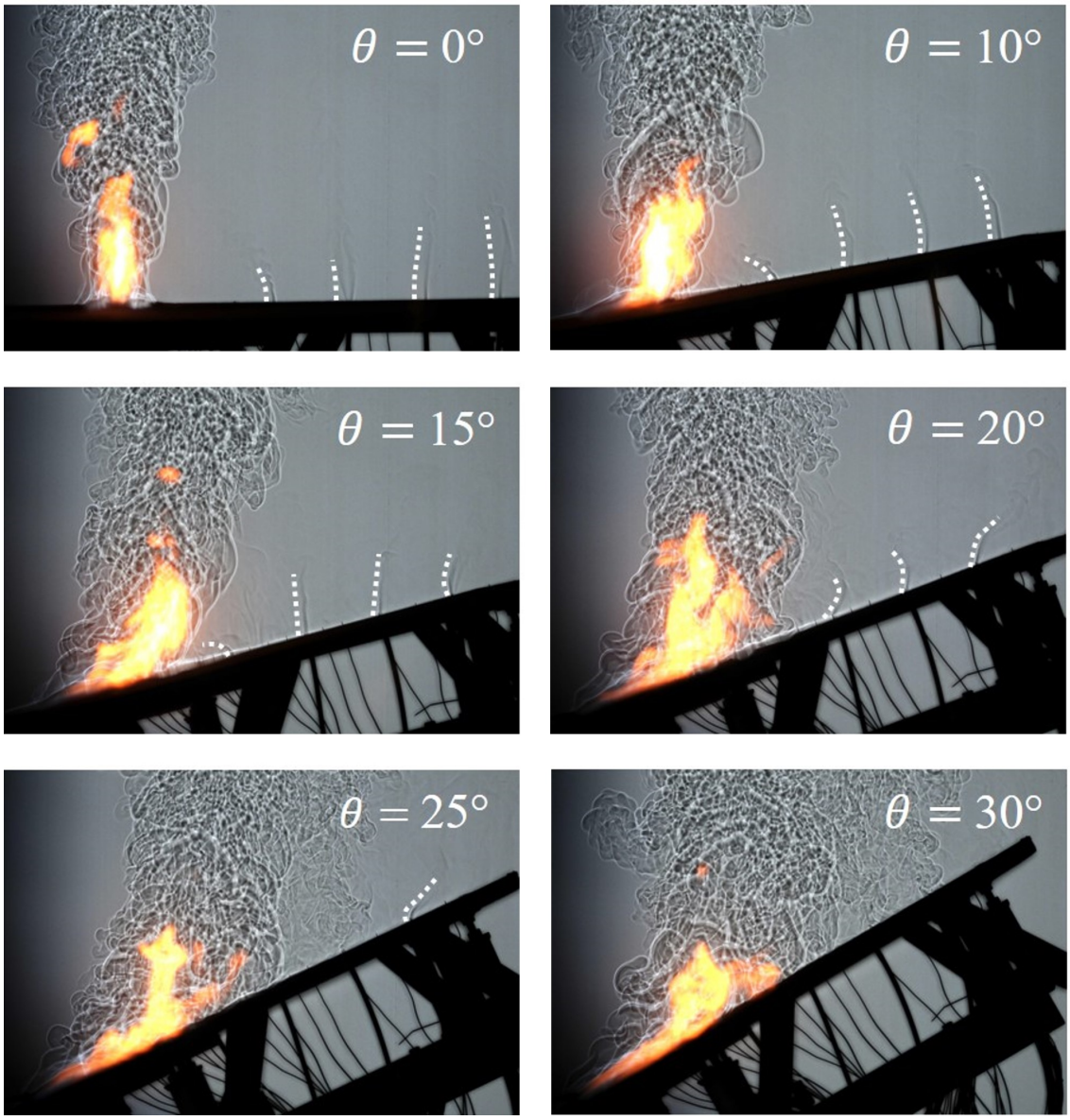

Figure 4.15: Image sequence of the inclination of a 10 kW flame and the impact on helium inlets (marked by the white dashed line).

for angles ranging from 14° to 24°, as displayed in Fig. 4.16. Negative flow velocities were detected for $\theta = 14°$, representing the entraining air flow toward the flame. When the angle increased to 16°, switch of the flow direction occurred, meaning that the flow was pushed away from the flame. For angles higher than 18°, velocity of the flow increased to a peak value then decreased at further downstream locations.

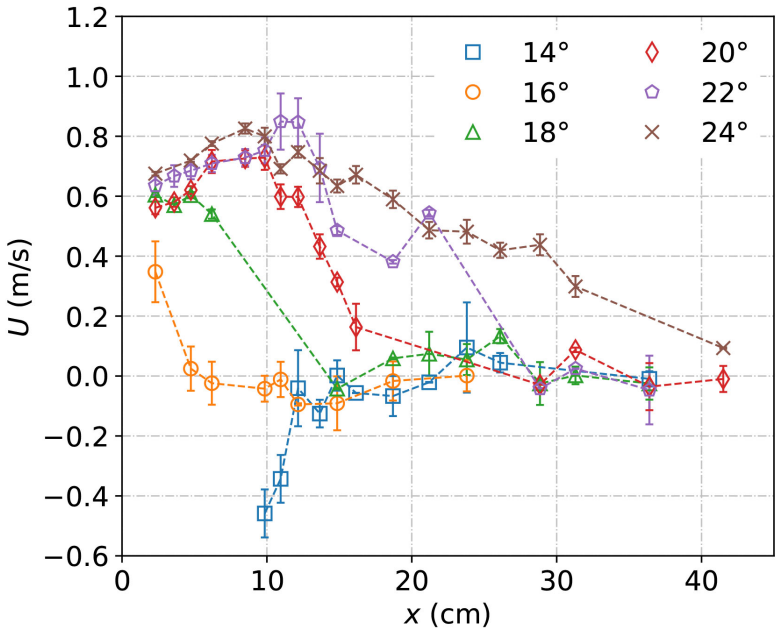

Figure 4.16: Surface flow velocity vs. downstream distance of a 10-kW flame. Error bar represents the standard deviation of the velocity.

Such behavior is essentially caused by the attachment and detachment of the fire plume. The surface flow was accelerated by the tangential buoyancy within the attached region. Beyond this region, the surface flow slowed down due to a lack of momentum. For angles from 20° to 24°, positive flow velocities were detected at farther downstream locations, which agrees with the flow direction probed by the helium jets. These results suggest that the buoyancy component overcomes the air entrainment when the critical angle is reached, thus dominating the surface flow.

4.5.2 Local flow velocity of the large-scale fire

To examine the relationship between the flame structure and flow dynamics, we plotted the heating profile and local velocities together in Fig. 4.17. Results were obtained from a 246 kW/m fire with a 24° angle. At the flame region where

$x < 30$ cm, the flow was accelerated by a strong buoyant force along the inclined surface. The velocity approached to a maximum at a location near the boundary between the flame and intermittent regime. The high temperature and high flow velocity in this region result in higher heat transfer which favors the occurrence of eruptive flame spread. Within the intermittent region (30 cm $< x <$ 80 cm), the flow velocity decayed after its peak. It is likely that the buoyancy at this region was not strong enough to accelerate the flow. On the other hand, buoyancy normal to the surface drove the flow away from the surface, resulting in flame pulsation (back-and-forth movement), which also contributed to a lower flow velocity along the surface. Although having a decaying velocity and a lower gas temperature, the pulsation of the flow still facilitates convective heating from the gas to the fuel in this region. At the plume region, where the gas temperature remains low ($T_{mean} < 320$ K if $x > 100$ cm), a relatively steady flow with a ~ 0.5 m/s velocity was measured. A similar flow velocity, at around 0.5 m/s, was also obtained in a numerical simulation by Verma [76], where a 100 kW/m inclined line fire with a 24° slope was simulated. For fine fuel particles, convective cooling is likely to take place within this region if the contribution from radiation is significant.

The surface flow velocity is affected by both slope and fire intensity. Figure 4.18 displays part of the results. Fig. 4.18a shows that both concurrent (positive velocity, away from the flame base) and opposed (negative velocity, heading to the flame base) flows were detected using the cross-correlation velocimetry technique. At an angle of 6°, the flame is similar to a purely vertical buoyancy driven flame. A steady negative velocity was measured, indicating an opposed flow driven by the

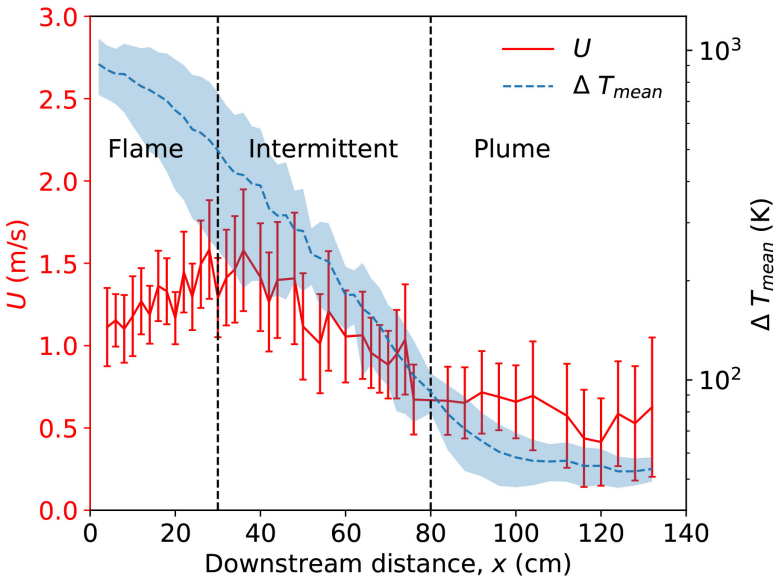

Figure 4.17: Velocity and temperature profiles of a 246 kW/m flame with a 24° angle (L = 3.66 m, D = 0.61 m). The shaded area and error bars represent the standard deviation.

entraining air. This velocity decreased to nearly 0 m/s at around $x = 60$ cm, which is consistent with shadowgraph observations presented earlier. For a larger slope at 12°, the partially attached flame has a positive velocity in the attached region; however, the flame detached from the surface after a short distance, resulting in a rapid decay of the flow velocity. Air entrainment is then seen to dominate the flow at farther downstream locations. For angles from 18° to 30°, the velocity profiles show a similar trend since the flames were attached. However, different peak velocities were detected due to the variation of the attachment length. Similar trend is observed in Fig. 4.18b for various fire intensities. Overall, under attached conditions, magnitude of the local surface flow velocity is proportional to the flame attachment length, which is essentially determined by the angle of inclination and the fire intensity.

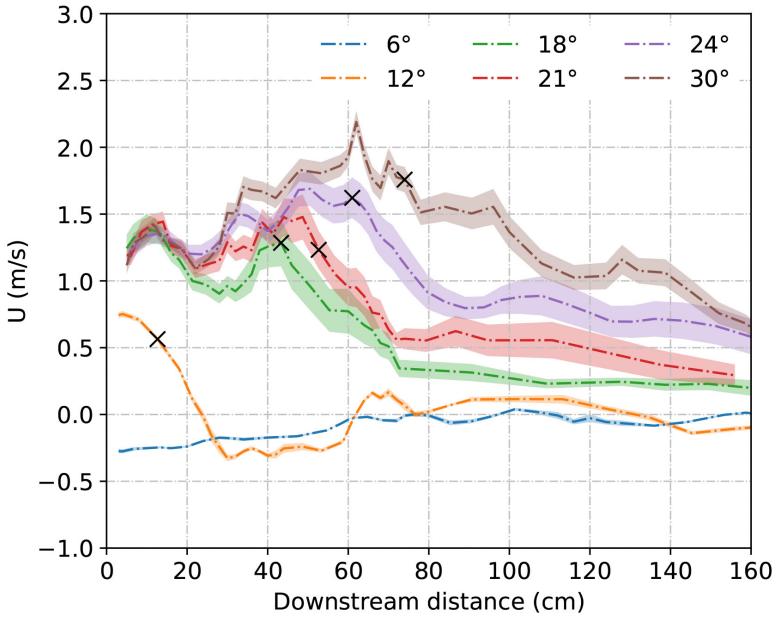

(a)

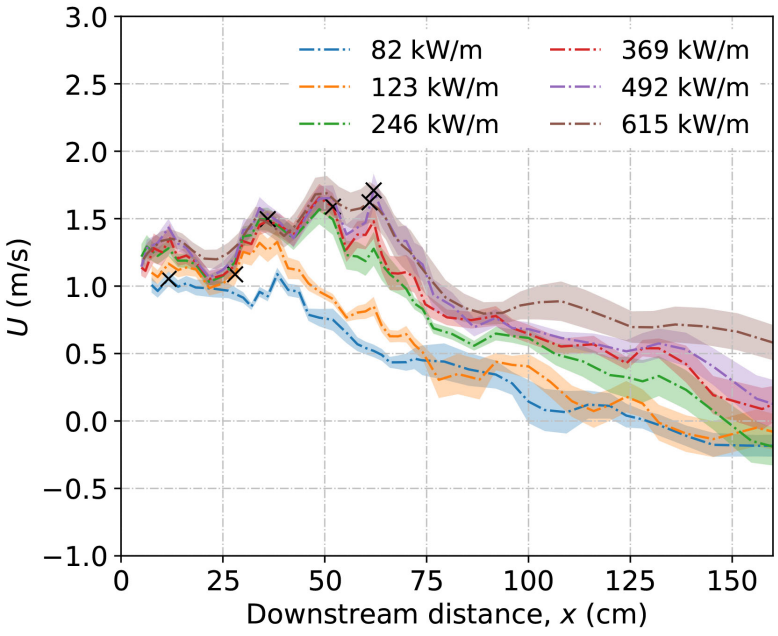

(b)

Figure 4.18: Surface flow velocities vs. downstream distance: (a) velocities under various slopes with a 615 kW/m fire intensity, (b) velocities under various fire intensities with a 24° slope. The shaded area represents 1/4 of the standard deviation. Flame attachment length was marked by '×'.

4.5.3 Velocity vs. flame attachment length

For fire spread problems, the rate of heat transfer is greatest within the attached flame region. In order to obtain optimal heat transfer coefficient, it is vital to know the local flow velocity. Results in section 4.5.2 have concluded that the flow velocity is positively related to the flame attachment length, which is determined by the slope and fire intensity. Ultimately, all these parameters are related to the buoyancy component along the inclined surface.

Figure 4.19 shows the buoyant force F_{buoy} decomposed into a component normal to the slope, $F_{buoy,n}$, and another component parallel to the slope, $F_{buoy,p}$. At high angles of inclination, $F_{buoy,p}$ becomes sufficiently large, pushing the flame toward the inclined surface, providing momentum for the flow. According to the momentum balance equation, $F_{buoy,p}$ can be represented by $\mathrm{Gr}sin\theta$. The Grashof number is calculated as Eq. 4.7

$$\mathrm{Gr} = \frac{g\beta(T_{mean} - T_0)(L_f + D/2)^3}{\nu^2}, \tag{4.7}$$

where g is the standard acceleration due to gravity, β is the coefficient of thermal expansion ($1/T_{mean}$), T_0 is the ambient air temperature, L_f is the flame attachment length, D is the burner streamwise depth and ν is the kinematic viscosity of air. On the other hand, the flow momentum is also proportional to Re^2, with the Reynolds number calculated as

$$\mathrm{Re} = \overline{U}(L_f + D/2)/\nu \tag{4.8}$$

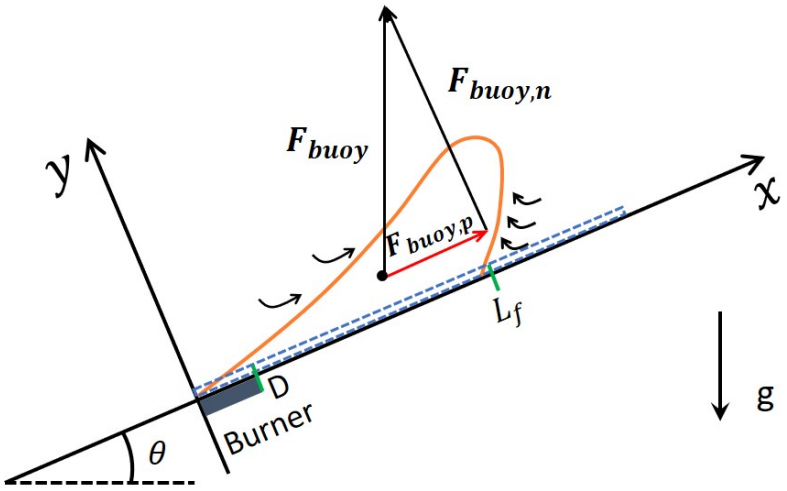

Figure 4.19: Decomposition of the buoyant force for inclined fire configuration

where $\overline{U}$ is the mean flow velocity at the attached region. If such analysis holds true, a force balance between $F_{buoy,p}$ and flow momentum should be expected, which is

$$\mathrm{Gr}sin\theta = \mathrm{Re}^2 \tag{4.9}$$

To evaluate Eq. 4.9, we calculated the Gr$sin\theta$ and Re. Results are plotted in Fig. 4.20. It is clear that Eq. 4.9 works well for line fires with aspect ratio higher than 6, i.e., $\alpha \geq 6$. For fires with $\alpha < 6$, a larger deviation from the theoretical value is observed in Fig. 4.20b. A possible reason is that stronger side entrainment occurred for tests with small burner aspect ratio, resulting variations in flow velocity and flame attachment length. Overall, a good agreement is observed between the experimental data and the theoretical prediction. Eq. 4.9 was validated by these results, proving that the momentum of the surface flow was mostly provided by the buoyancy component along the inclined surface.

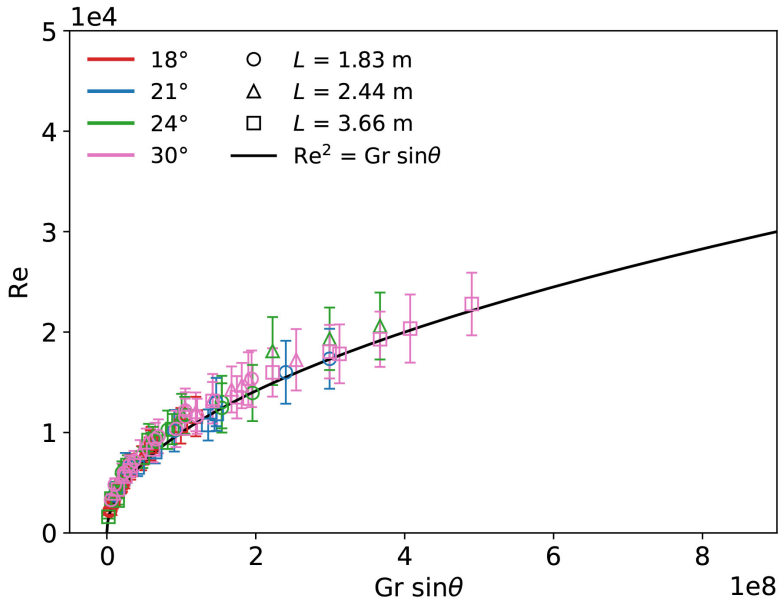

(a)

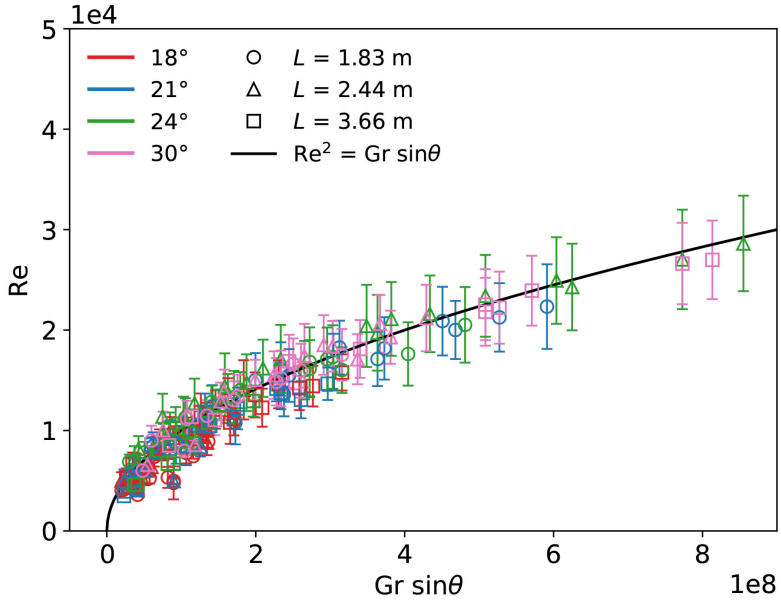

(b)

Figure 4.20: Re vs. Gr$sin\theta$: (a) results with $\alpha \geq 6$ and (b) results with $\alpha < 6$. The error bar represents 1/2 standard deviation of the velocity within the attached region.

4.6 Slope, fire intensity and surface flow velocity

Two main relationships have been obtained in Sections 4 and 5. Equation 4.6 describes the flame attachment length (L_f) using fire intensity ($\dot{Q}'$) and angle of inclination (θ); equations 4.7 - 4.9 estimate the flow momentum using the buoyancy component along the inclined surface, which was derived from the flame attachment length (L_f) and slope (θ). Using these equations, a new relationship which corelates the mean flow velocity using the fire intensity and angle of inclination is derived as

$$U = \begin{cases} 1.24 sin^2 2\theta \sqrt{gAZsin\theta} & \text{if } \alpha \geq 6 \\ 0.85 sin^2 2\theta \sqrt{gAZsin\theta} & \text{if } \alpha < 6 \end{cases} \tag{4.10}$$

with $Z = [\dot{Q}'/\rho_0 c_p T_0 g^{1/2}]^{2/3}$. To evaluate the derived relationship, we plotted the predicted surface flow velocity against the measured velocity. Figure 4.21a shows that Eq. 4.10 overpredicted the flow velocity in $\sim 11\%$ for burners with high aspect ratios ($\alpha \geq 6$). For burners with low aspect ratios ($\alpha < 6$), the velocity prediction performed well for most of the tests. However, for low flow velocities (< 1 m/s) with an 18° angle, Eq. 4.10 overestimated the flow velocity, as displayed in Fig. 4.21b. These discrepancies between the measured and the predicted velocity could be attributed by the uncertainties associated with the flame attachment prediction in Eq. 4.6. Nevertheless, results show that the proposed relationship is able to predict the mean value of the fire induced flow using the fire intensity and inclined geometry, providing a useful reference for future fire model development.

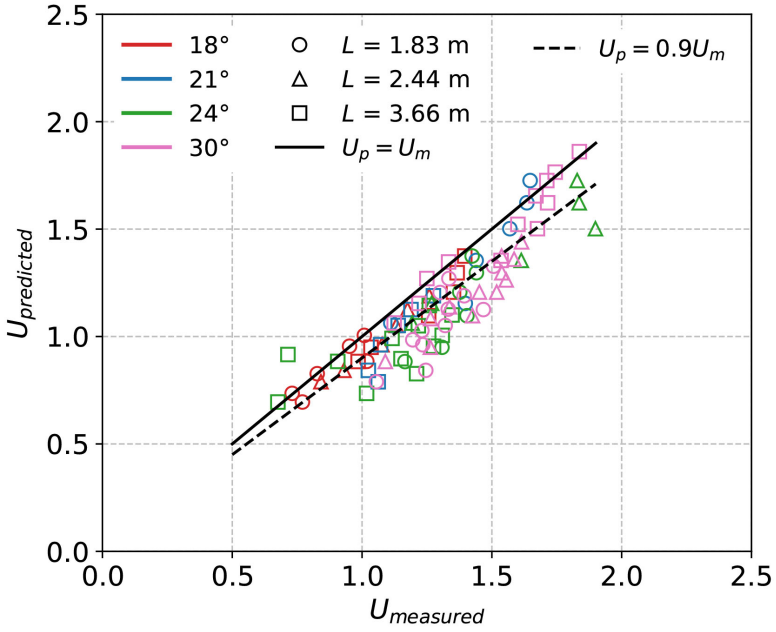

(a)

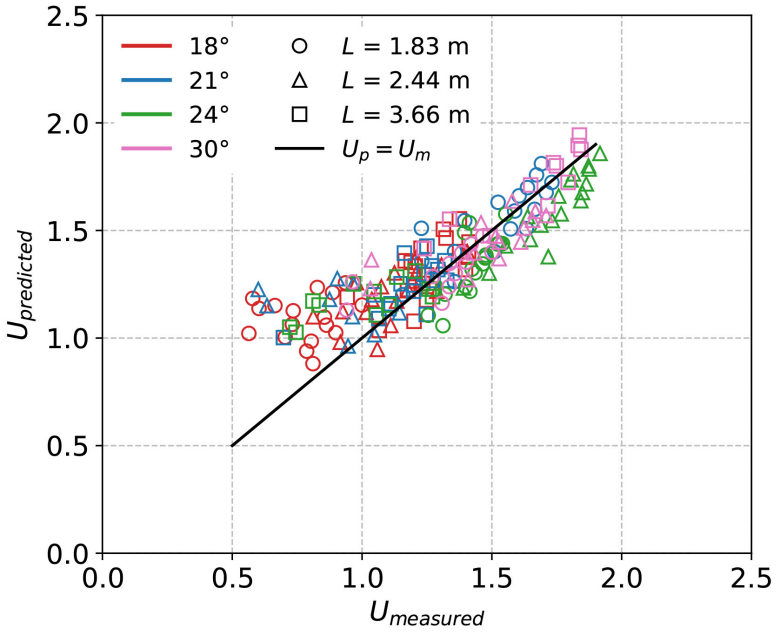

(b)

Figure 4.21: Predicted mean velocity vs. measured mean velocity for the attached flame region: (a) results with $\alpha \geq 6$ and (b) results with $\alpha < 6$. Error bars (up to 31% of the mean) are not displayed for a better illustration of the results.

In wildfire spread, role of buoyant flame dynamics has been re-evaluated [6,26]. The reported results have shown that wildfire spread is closely related to the tight coupling between the fire-induced flow and fine-particle response to convection. The traditional lumped heat transfer model is not suitable for ignition prediction of fine fuel particles [144]. The high heat transfer coefficient associated with fine particles resulting in substantial convective cooling [6], which effectively offset heating by thermal radiation. Ignition occurs until convective heating by contact with flames and hot gasses takes place. These findings highlight the importance of local flow velocity which is needed for the estimation of heat transfer coefficient. Most of the related research focuses on purely buoyant flames and wind-driven flames, leaving a gap on the dynamics of inclined fires. This study measured the temperature and flow velocity of the inclined fire simultaneously, providing a valuable dataset for the development of linear regression models. On the other hand, generalized relationships that describe the tight coupling of slope, fire intensity and surface flow velocity were proposed using scaling analysis. Clearly, the momentum of the surface flow is served by the tangential buoyancy components of the inclined fire. The magnitude of the momentum scales with the 2/3 power of fire intensity, and $sin^2 2\theta$ of the slope. These relationships enable the evaluation of the mean flow velocity in the attached flame region, providing a useful reference for future fire model development.

4.7 Conclusion

In this Chapter, multi-scale experiments were designed to test the downstream heating and flow dynamics of inclined fires. Flames were found to attached to the inclined surface at a critical angle of 18°, independent of the scales of the flame. Under attached conditions, the centerline flame temperatures closely resembled McCaffery's temperature correlation for purely buoyant flames (no slope). Flame, intermittent and plume regions defined by McCaffery have been applied into current inclined fires, with gradients of $\eta = 0$, $\eta = -3/2$ and $\eta = -2$, respectively. The length of the flame region is found to be linearly related to the slope factor ($sin^2 2\theta$) and characteristic flame length (Z), written as $L_f \sim Z sin^2 2\theta$.

The flow field of the inclined fires were examined using shadowgraph images and a cross-correlation velocimetry technique. The shadowgraph images with an additional direction tracker (helium jets) showed the existence of reversed flow and tangential fire-induced flow depending on angles of inclination. Cross-correlation velocimetry captured local flow velocities and their directions, serving as an effective velocity measurement tool under the hostile high-temperature environment. Velocity profiles along the downstream location showed that the local flow was accelerated in the attached flame region driven by the buoyancy component along the surface. The peak of the flow velocity was detected near the boundary of the flame and intermittent regions. The flow velocity slowed down after the peak due to weak buoyancy within the intermittent and plume regions. Using stress analysis, momentum of the attached flow was expressed using the buoyancy component along

the surface, meaning $\mathrm{Gr}sin\theta = \mathrm{Re}^2$. This formula was further validated using the experimental data.

Finally, a generalized relationship with a single empirical constant was proposed to correlate the mean flow velocity using the fire intensity and angle of inclination. Good agreement was observed between the proposed relationship and experimental data. Results from this work have highlighted the importance of the role of fire-induced flow. The proposed relationships that describe the coupling effect between fire intensity, angles of inclination, and fire-induced flow server as a first step to develop physical-based inclined fire spread models. It is our hope that the measure local flow velocity can provide additional dataset for future linear regression model development.

Chapter 5: Conclusions and future work

5.1 Conclusions

In this dissertation, experimental techniques and data analysis methods were developed and applied to understand the thermal and fluid structure of three canonical fires. The discovered fire characteristics, providing both enhanced understanding and new data for model validation.

The first experiment characterized the thermal structure of a turbulent buoyant ethylene diffusion flame. A dual-thermocouple technique was used to provide accurate gas temperature measurements. Both sensitivity and uncertainty analyses showed that this improved dual-TC technique has advantages under hostile flame environments where the bead diameter may change due to soot deposition or other effects. Measured temperatures were compensated using a temporally-varying time constant, producing a systematic temperature dataset for 15 kW buoyant turbulent ethylene flames. The resultant mean, rms and PDF temperature profiles provide a detailed picture of the turbulent flame structure. These temperature measurements, alongside existing data such as the radiant power distribution, local soot volume fraction and soot temperature, as well as future gas velocity measurements will provide a detailed dataset of this flame for validation and development of radi-

ation models.

The second experiment characterized the physical and thermal structure of a stationary wind-driven flame. The role of the freestream turbulence was carefully examined. The results show that turbulence in the freestream promotes the formation and growth of coherent flame streaks in a boundary-layer flame, destabilizes streamwise vortex rolls, and eventually leads to a transition to turbulence and a shorter flame attachment length. A non-dimensional relationship was proposed to correlate the flame attachment length using the Froude number (Fr), non-dimensional heat release rate (Q^*), and flow turbulence intensity $(1 - \mathrm{TI})^3$. It was found that freestream turbulence redistributed flame streaks, widened the high heat flux flame trough, and ultimately increased the heat flux from flame to the downstream surface. Significant heat flux enhancement was measured when the flame changed from a laminar to a nearly turbulent state triggered by different levels of freestream turbulence. Two different heating modes, a momentum dominated mode and plume mode, have been observed and found to be separated by a critical Richardson number. This critical Richardson number changed from 1.0 to 0.1 when the flame transitioned from a laminar to a nearly fully developed turbulent state.

Finally, the uphill heating and flow dynamics of inclined fires with heat release rates ranging from 10 kW to 2.25 MW were examined. Flames were found to attached to the inclined surface at a critical angle of 18°, independent of the scales of the flame. Under attached conditions, the centerline flame temperatures closely resembled McCaffery's temperature correlation for purely buoyant flames (no slope). Flame, intermittent and plume regions defined by McCaffery have been applied into

current inclined fires, with exponents of $\eta = 0$, $\eta = -3/2$ and $\eta = -2$, respectively. Length of the flame region is found to be linearly related to the slope factor (sin^2 2θ) and characteristic flame length (Z), written as $L_f \sim Z sin^2\ 2\theta$. The flow field of the inclined fires were examined using shadowgraph images and a cross-correlation velocimetry technique. The shadowgraph images showed the existence of a reversed flow and tangential fire-induced flow depending on the angle of inclination. The cross-correlation velocimetry technique captured the local flow velocities and their directions, showing that the local flow was accelerated in the attached flame region driven by the buoyancy component along the surface. Results showed that the momentum of the attached flow is proportional to the buoyancy component along the upslope surface, meaning Gr $sin\theta = \mathrm{Re}^2$. Finally, a generalized relationship was proposed to correlate the mean flow velocity using the fire intensity and angle of inclination.

5.2 Future work

During wildland fire spread both slope and wind act together to modify fire dynamics, commonly accelerating the rate of fire spread. When exposed to an external wind, a horizontally-spreading fire bends towards the concurrent direction, enhancing both radiative and convective heat transfer between the flame and adjacent unburnt fuel. A similar phenomena occurs when fire spreads uphill, where both the pressure difference-induced 'Coanda' effect and fire-induced flow 'push' the fire towards the inclined surface, resulting in a faster rate of fire spread. Often times,

wildland fires occur with the presence of both slope and wind, thus subjecting flames to their coupled effects. Although the individual effect of either wind or slope has been widely examined, work investigating their coupled effects is still limited.

At present, most efforts combining the effects of slope and wind use the fire rate of spread as an explicit output. Although the fire rate of spread has been widely adopted in such analyses, shortcomings exist for practical applications. The rate of spread essentially depends on the heating from the flame and the fuel properties, but the later varies from case to case. Moreover, it has been found that convective heat transfer significantly modifies the fire rate of spread. Particularly for fine fuel elements in wildland vegetation, convective cooling is observed to effectively offset heating by thermal radiation until convective heating by contact with flames and hot gasses occurs. Resolving these heat transfer processes could be a more physical and universal approach to model the combined effects of slope and wind. Towards that purpose, flow field measurements of fires could be conducted in future using the developed temperature-correlation velocimetry (TCV) technique.

Appendix A: Radiant heat flux estimation

The heat flux to a thermocouple bead can be estimated by assuming the thermocouple bead has a diameter of d_i, i =1,2. The fire is idealized to have a cylindrical shape, with a height of $z_f = 0.7$ m, and diameter of $d_f = 0.152$ m. The radiative power per unit volume of the fire (kW/m^3) is

$$\dot{q}_r''' = \frac{Q}{V_f}\chi_r, \tag{A.1}$$

where Q is the theoretical heat-release rate (15 kW), $V_f$is the flame volume ($z_f \pi d_f^2/4$), and χ_r is the radiant fraction (0.34 for ethylene).

Figure. A.1 shows a thermocouple placed at a radius of r_{th} and a height of Z_{th}. For an infinitely-small flame volume element at a height of z_0, radius of r_0 from the centerline, and an azimuthal angle of θ degree from x axis, the distance of the element to thermocouple is

$$d_{th-f} = \{[(r_{th} + r_0)sin(\theta/2)]^2 + [(r_{th} - r_0)cos(\theta/2)]^2 + (z_0 - z_{th})^2)\}^{1/2}. \tag{A.2}$$

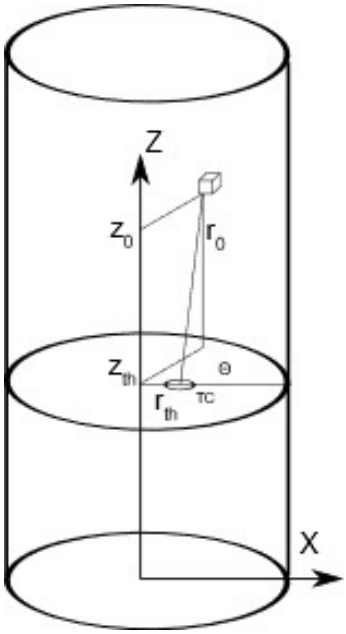

Figure A.1: Idealized flame radiant heat flux calculation.

The radiant heat flux per unit area to the surface of the thermocouple is

$$q''_{r,u} = \int_0^{d_f/2} \int_0^{z_f} \int_0^{2\pi} \frac{r_0}{\dot{q}'''_r} d\theta dz_0 dr_0. \tag{A.3}$$

Using Eq. A.3, $\dot{q}''_{rad}$ for a thermocouple can be determined. The highest possible heat flux is determined at the center location (0 cm radius, 2.5D = 0.38 m height), with $\dot{q}''_{rad} = 45$ kW/m^2.

Appendix B: Subsample interpolation of time lag and Estimation of the integral length

B.1 Subsample interpolation of time lag

Raw temperature data of this study was recorded at 500 Hz, which limited the time resolution to 0.002 s. This limitation results in discrete velocities since the velocity is derived using $U = d/\tau$ with a fixed d. In order to obtain a high-resolution velocity, the time resolution needs to be improved. Therefore, a subsample interpolation method [145, 146] was implemented to better estimate the location of the peak of the cross-correlation function. A gaussian curve fitting was applied to 5 data points closet to the peak (i.e., τ = -0.022 s) of the correlation coefficient. The new peak of the gaussian curve in Fig. B.1 was used to locate the updated time lag, i.e., τ = -0.0214 s. This way, the time resolution was improved subsample delay-time resolution was achieved, enhancing the flow velocity estimation.

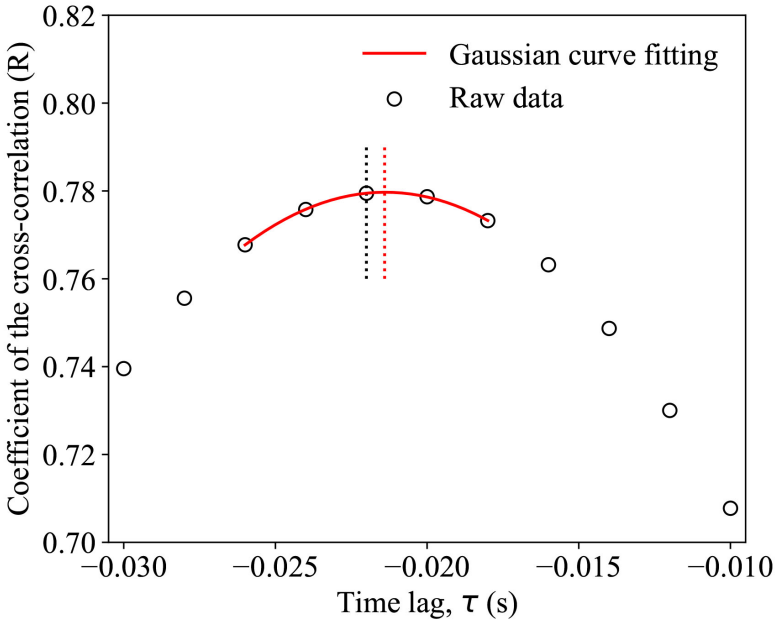

Figure B.1: Subsample interpolation of the discrete cross-correlation function..

Bibliography

[1] W.E. Cascio. Wildland fire smoke and human health. *Science of the total environment*, 624:586–595, 2018.

[2] National interagency fire center. `https://www.nifc.gov/fire-information/statistics/wildfires`. Accessed: 2021-10-17.

[3] Headwaters Economics. Wildfires destroy thousands of structures each year, 2020.

[4] F.A. Albini. A model for fire spread in wildland fuels by-radiation. *Combustion Science and Technology*, 42(5-6):229–258, 1985.

[5] F.A. Williams. Mechanisms of fire spread. *Symposium (International) on Combustion*, 16(1):1281–1294, 1977.

[6] M.A. Finney, J.D. Cohen, S.S. McAllister, and W.M. Jolly. On the need for a theory of wildland fire spread. *International Journal of Wildland Fire*, 22(1):25–36, 2013.

[7] D. Frankman, B.W. Webb, B.W. Butler, D. Jimenez, J.M. Forthofer, P. Sopko, K.S. Shannon, J.K. Hiers, and R.D. Ottmar. Measurements of convective and radiative heating in wildland fires. *International Journal of Wildland Fire*, 22(2):157–167, 2012.

[8] F.A. Albini. Wildland fire spread by radiation-a model including fuel cooling by natural convection. *Combustion Science and Technology*, 45(1-2):101–113, 1986.

[9] H.W. Emmons. Fire in the forest. *Fire Research Abstracts and Reviews*, 5(3):163–178, 1964.

[10] H.C. Hottel, G.C. Williams, and F.R. Steward. The modeling of firespread through a fuel bed. *Symposium (International) on combustion*, 10(1):997–1007, 1965.

[11] H.C. Hottel, G.C. Williams, and G.K. Kwentus. Fuel preheating in free-burning fires. *Symposium (International) on Combustion*, 13(1):963–970, 1971.

[12] P.H. Thomas. Some aspects of the growth and spread of fire in the open. *Forestry: An International Journal of Forest Research*, 40(2):139–164, 1967.

[13] W.H. Frandsen. Fire spread through porous fuels from the conservation of energy. *Combustion and Flame*, 16(1):9–16, 1971.

[14] N.P Kurbatskiy and G.P. Telitsin. Theoretical and experimental analysis of the radiation mechanisms for the spread of forest fire. *Characteristics of the process of combustion in forests. Edited by Kane, EV USSR Academy of Science, Siberian Branch, Krasnoyarsk*, pages 1–33, 1977.

[15] G.F. Carrier, F.E. Fendell, and M.F. Wolff. Wind-aided firespread across arrays of discrete fuel elements. i. theory. *Combustion science and technology*, 75(1-3):31–51, 1991.

[16] E.A. Catchpole, W.R. Catchpole, and R.C. Rothermel. Fire behavior experiments in mixed fuel complexes. *International Journal of Wildland Fire*, 3(1):45–57, 1993.

[17] W.R. Catchpole, E.A. Catchpole, B.W. Butler, R.C. Rothermel, G.A. Morris, and D.J. Latham. Rate of spread of free-burning fires in woody fuels in a wind tunnel. *Combustion Science and Technology*, 131(1-6):1–37, 1998.

[18] J.B. Fang and F.R. Steward. Flame spread through randomly packed fuel particles. *Combustion and flame*, 13(4):392–398, 1969.

[19] P.G. Baines. Physical mechanisms for the propagation of surface fires. *Mathematical and Computer Modelling*, 13(12):83–94, 1990.

[20] J.L. Dupuy and J. Maréchal. Slope effect on laboratory fire spread: Contribution of radiation and convection to fuel bed preheating. *International Journal of Wildland Fire*, 20(2):289–307, 2011.

[21] G.M. Byram, H.B. Clements, E.R. Elliott, and P.M. George. An experimental study of model fires: Technical report no. 3. 1964.

[22] M. Vogel and F.A. Williams. Flame propagation along matchstick arrays. *Combustion Science and Technology*, 1(6):429–436, 1970.

[23] L. Jiang, Z. Zhao, W. Tang, C.H. Miller, J. Sun, and M.J. Gollner. Flame spread and burning rates through vertical arrays of wooden dowels. *Proceedings of the Combustion Institute*, 37(3):3767–3774, 2019.

[24] M.A. Finney, J.D. Cohen, I.C. Grenfell, and K.M. Yedinak. An examination of fire spread thresholds in discontinuous fuel bedsa. *International Journal of Wildland Fire*, 19(2):163–170, 2010.

[25] K.M. Yedinak, J.D. Cohen, J.M. Forthofer, and M.A. Finney. An examination of flame shape related to convection heat transfer in deep-fuel beds. *International Journal of Wildland Fire*, 19(2):171–178, 2010.

[26] M.A. Finney, J.D. Cohen, J.M. Forthofer, S.S. McAllister, M.J. Gollner, D.J. Gorham, K. Saito, N.K. Akafuah, B.A. Adam, and J.D. English. Role of buoyant flame dynamics in wildfire spread. *Proceedings of the National Academy of Sciences*, 112(32):9833–9838, 2015.

[27] A.V. Singh and M.J. Gollner. A methodology for estimation of local heat fluxes in steady laminar boundary layer diffusion flames. *Combustion and Flame*, 162(5):2214–2230, 2015.

[28] Xiaoyu Ju, Michael J. Gollner, Yiren Wang, Wei Tang, Kun Zhao, Xingyu Ren, and Lizhong Yang. Downstream radiative and convective heating from methane and propane fires with cross wind. *Combustion and Flame*, 204:1–12, jun 2019.

[29] X. Silvani and F. Morandini. Fire spread experiments in the field: temperature and heat fluxes measurements. *Fire Safety Journal*, 44(2):279–285, 2009.

[30] F. Morandini, X. Silvani, J.L. Dupuy, and A. Susset. Fire spread across a sloping fuel bed: Flame dynamics and heat transfers. *Combustion and Flame*, 190:158–170, 2018.

[31] C.H. Miller, W. Tang, M.A. Finney, S.S. McAllister, J.M. Forthofer, and M.J. Gollner. An investigation of coherent structures in laminar boundary layer flames. *Combustion and Flame*, 181:123–135, 2017.

[32] C.H. Miller, W. Tang, M.A. Sluder, E.T.and Finney, S.S. McAllister, J.M. Forthofer, and M.J. Gollner. Boundary layer instabilities in mixed convection and diffusion flames with an unheated starting length. *International Journal of Heat and Mass Transfer*, 118:1243–1256, 2018.

[33] C.B. Clements, A.K. Kochanski, D. Seto, B. Davis, C. Camacho, N.P. Lareau, J. Contezac, J. Restaino, W.E. Heilman, S.K. Krueger, et al. The fireflux ii experiment: a model-guided field experiment to improve understanding of fire–atmosphere interactions and fire spread. *International journal of wildland fire*, 28(4):308–326, 2019.

[34] R.L. Panton. Overview of the self-sustaining mechanisms of wall turbulence. *Progress in Aerospace Sciences*, 37(4):341–383, 2001.

[35] D. Zeng, P. Chatterjee, and Y. Wang. The effect of oxygen depletion on soot and thermal radiation in buoyant turbulent diffusion flames. *Proceedings of the Combustion Institute*, 37(1):825–832, 2019.

[36] G. Xiong, D. Zeng, P.P. Panda, and Y. Wang. Laser induced incandescence measurement of soot in ethylene buoyant turbulent diffusion flames under normal and reduced oxygen concentrations. *Combustion and Flame*, 230:111456, aug 2021.

[37] FM Global. FireFOAM,. Available from: `http://www.fmglobal.com/modeling`.

[38] Y. Wang, P. Chatterjee, and John L. De Ris. Large eddy simulation of fire plumes. *Proceedings of the Combustion Institute*, 33(2):2473–2480, 2011.

[39] K. McGrattan, S. Hostikka, R. McDermott, J. Floyd, and M. Vanella. Fire Dynamics Simulator User's Guide. *NIST Special Publication 1019 Sixth Edition*, page 347, 2019.

[40] S.P. Kearney and T.W. Grasser. Laser-diagnostic mapping of temperature and soot statistics in a 2-m diameter turbulent pool fire. *Combustion and Flame*, 186:32–44, 2017.

[41] Z. Wang, Wai C. Tam, K. Lee, and A. Hamins. Temperature Field Measurements using Thin Filament Pyrometry in a Medium-Scale Methanol Pool Fire - NIST Technical Note 2031. 2018.

[42] E.T. Hariharan, S.B.and Sluder, M.J. Gollner, and E.S. Oran. Thermal structure of the blue whirl. *Proceedings of the Combustion Institute*, 37(3):4285–4293, 2019.

[43] S.B. Hariharan, P.M. Anderson, H. Xiao, M.J. Gollner, and E.S. Oran. The blue whirl: Boundary layer effects, temperature and OH* measurements. *Combustion and Flame*, 203:352–361, 2019.

[44] G. Cox and R. Chitty. A study of the deterministic properties of unbounded fire plumes. *Combustion and Flame*, 39(2):191–209, 1980.

[45] O. Korobeinichev, M. Gonchikzhapov, A. Tereshchenko, I. Gerasimov, A. Shmakov, A. Paletsky, and A. Karpov. An experimental study of horizontal flame spread over PMMA surface in still air. *Combustion and Flame*, 188:388–398, 2018.

[46] S. Brohez, C. Delvosalle, and G. Marlair. A two-thermocouples probe for radiation corrections of measured temperatures in compartment fires. 39:399–411, 2004.

[47] W.C. Strahle and M. Muthukrishnan. Thermocouple time constant measurement by cross power spectra. *AIAA Journal*, 1976.

[48] M. Vachon, P. Cambray, T. Maciaszek, and J.C. Bellet. Temperature and velocity fluctuation measurements in a diffusion flame with large buoyancy effects. *Combustion Science and Technology*, 48(5-6):223–240, 1986.

[49] S.J. Fischer, B. Hardouin-Duparc, and W.L. Grosshandler. The structure and radiation of an ethanol pool fire. *Combustion and Flame*, 70(3):291–306, 1987.

[50] M. Kunugi and H. Jinno. Measurements of fluctuating flame temperature. *Symposium (International) on Combustion*, 7(1):942–948, jan 1958.

[51] E.J. Weckman and A.B. Strong. Experimental investigation of the turbulence structure of medium-scale methanol pool fires. *Combustion and Flame*, 105(3):245–266, 1996.

[52] A. Ballantyne and J.B. Moss. Fine wire thermocouple measurements of fluctuating temperature. *Combustion Science and Technology*, 1977.

[53] L.J. Forney and G.C. Fralick. Three-wire thermocouple: Frequency response in constant flow. *Review of Scientific Instruments*, 66(5):3331–3336, 1995.

[54] P.G. O'Reilly, R.J. Kee, R. Fleck, and P.T. McEntee. Two-wire thermocouples: A nonlinear state estimation approach to temperature reconstruction. *Review of Scientific Instruments*, 72(8):3449–3457, 2001.

[55] M. Tagawa and Y. Ohta. Two-thermocouple probe for fluctuating temperature measurement in combustion - Rational estimation of mean and fluctuating time constants. *Combustion and Flame*, 109(4):549–560, 1997.

[56] P.A. Santoni, T. Marcelli, and E. Leoni. Measurement of fluctuating temperatures in a continuous flame spreading across a fuel bed using a double thermocouple probe. *Combustion and Flame*, 131(1-2):47–58, 2002.

[57] M.C. Croarkin, W.F. Guthrie, G.W. Burns, M. Kaeser, and G.F. Strouse. Temperature-Electromotive Force Reference Functions and Tables for the Letter-Designated Thermocouple Types Based on the ITS-90. *National Institute of Standards and Technology. Monograph 175*, 1993.

[58] C.R. Shaddix. Correcting Thermocouple Measurements for Radiation Loss: A Critical Review. pages 1–10, 1999.

[59] B.N. Taylor and C.E. Kuyatt. NIST Technical Note 1297 1994 Edition Guidelines for Evaluating and Expressing the Uncertainty of NIST Measurement Results. 1994.

[60] V. Gururajan and F.N. Egolfopoulos. Direct sensitivity analysis for ignition delay times. *Combustion and Flame*, 209:478–480, 2019.

[61] D. Bradley and A.G. Entwistle. Determination of the emissivity, for total radiation, of small diameter platinum-10% rhodium wires in the temperature range 600-1450 c. *British Journal of Applied Physics*, 12(12):708, 1961.

[62] B.J. McCaffrey. Purely buoyant diffusion flames: some experimental results, NBSIR 79-1910. Technical report, 1979.

[63] C.S. McEnally, Ü.Ö. Köylü, L.D. Pfefferle, and D.E. Rosner. Soot volume fraction and temperature measurements in laminar nonpremixed flames using thermocouples. *Combustion and Flame*, 109(4):701–720, 1997.

[64] R.P. Bhatta, R.K. Annamalai, S.and Mohr, M. Brandys, I.L. Pegg, and B.s Dutta. High temperature thermal conductivity of platinum microwire by 3 ω method. *Review of Scientific Instruments*, 81(11):114904, 2010.

[65] A. Salvi, J. Hoard, M. Bieniek, M. Abarham, D. Styles, and D. Assanis. Effect of volatiles on soot based deposit layers. *Journal of Engineering for Gas Turbines and Power*, 136(11), 2014.

[66] J.G. Quintiere. *Fundamentals of fire phenomena*. Wiley, London, 2006.

[67] R.J. Santoro, T.T. Yeh, J.J. Horvath, and H.G. Semerjian. The transport and growth of soot particles in laminar diffusion flames. *Combustion Science and Technology*, 53(2-3):89–115, 1987.

[68] G. De Falco, G. Moggia, M. Sirignano, M. Commodo, P. Minutolo, and A. D'Anna. Exploring soot particle concentration and emissivity by transient thermocouples measurements in laminar partially premixed coflow flames. *Energies*, 10(2):232, 2017.

[69] C.B. Clements, S. Zhong, X. Bian, W. E. Heidman, and D.W. Byun. First observations of turbulence generated by grass fires. *Journal of Geophysical Research Atmospheres*, 113(22):1–13, 2008.

[70] H.W. Emmons. The film combustion of liquid fuel. *ZAMM-Journal of Applied Mathematics and Mechanics/Zeitschrift für Angewandte Mathematik und Mechanik*, 36(1-2):60–71, 1956.

[71] C.H. Miller, M.J. Gollner, M.A Finney, and D. Gorham. An investigation of wildfire dynamics via fixed inclinable burners. In *9th US National Combustion Meeting*, 2015.

[72] N. Gustenyov, N.K. Akafuah, A. Salaimeh, M.A. Finney, S. McAllister, and K. Saito. Scaling nonreactive cross flow over a heated plate to simulate forest fires. *Combustion and Flame*, 197:340–354, 2018.

[73] M. Heck. The influence of wind on the structure of inclined flames. Master's thesis, University of Maryland, College Park, 2020.

[74] A.W. Cook, W. Cabot, and P.L. Miller. The mixing transition in rayleigh–taylor instability. *Journal of Fluid Mechanics*, 511:333–362, 2004.

[75] P.S. Kumar, V. Raghavan, and T. Sundararajan. Experimental study of burning of methanol fed porous spheres in grid generated turbulent field. *International Journal of Heat and Mass Transfer*, 114:354–362, 2017.

[76] S. Verma. *Understanding flame structure in wildfires using Large Eddy Simulations*. PhD thesis, University of Maryland, College Park, 2014.

[77] N. Frangieh, G. Accary, D. Morvan, and S. Méradji. Wildfires front dynamics : 3D structures and intensity at small and large scales. 211:54–67, 2020.

[78] L. Zhou and A.C. Fernandez-Pello. Turbulent burning of a flat fuel surface. *Fire Safety Science*, 3:415–424, 1991.

[79] L. Zhou and A.C. Fernandez-Pello. Solid fuel combustion in a forced, turbulent, flat plate flow: the effect of buoyancy. *Symposium (International) on Combustion*, 24(1):1721–1728, 1992.

[80] A. Singh and A.V. Singh. Burning behavior of mixed-convection wind-driven flames under varying freestream conditions. *Fire Safety Journal*, 122:103320, 2021.

[81] P. S. Klebanoff, K. D. Tidstrom, and L. M. Sargent. The three-dimensional nature of boundary-layer instability. *Journal of Fluid Mechanics*, 1962.

[82] M. Matsubara and P. H. Alfredsson. Disturbance growth in boundary layers subjected to free-stream turbulence. *Journal of Fluid Mechanics*, 430:149–168, 2001.

[83] L. Brandt and D.S. Schlatter, P.and Henningson. Transition in boundary layers subject to free-stream turbulence. *Journal of Fluid Mechanics*, 517:167–198, 2004.

[84] B.F. Farrell and P.J. Ioannou. Dynamics of streamwise rolls and streaks in turbulent wall-bounded shear flow. *Journal of Fluid Mechanics*, 708:149–196, 2012.

[85] J. R. Welker and C. M. Sliepcevich. Bending of wind-blown flames from liquid pools. *Fire Technology*, 2(2):127–135, 1966.

[86] P. K. Raj. A physical model and improved experimental data correlation for wind induced flame drag in pool fires. *Fire Technology*, 46(3):579–609, 2010.

[87] L. Hu. A review of physics and correlations of pool fire behaviour in wind and future challenges. *Fire Safety Journal*, 91:41–55, 2017.

[88] Y. Lin, X. Zhang, and L. Hu. An experimental study and analysis on maximum horizontal extents of buoyant turbulent diffusion flames subject to relative strong cross flows. *Fuel*, 234:508–515, 2018.

[89] W. Tang, C.H. Miller, and M.J. Gollner. Local flame attachment and heat fluxes in wind-driven line fires. *Proceedings of the Combustion Institute*, 36(2):3253–3261, 2017.

[90] V.B. Apte, R.W. Bilger, A.R. Green, and J.G. Quintiere. Wind-aided turbulent flame spread and burning over large-scale horizontal PMMA surfaces. *Combustion and Flame*, 85(1-2):169–184, 1991.

[91] I.T. Leventon, J. Li, and S.I. Stoliarov. A flame spread simulation based on a comprehensive solid pyrolysis model coupled with a detailed empirical flame structure representation. *Combustion and Flame*, 162(10):3884–3895, 2015.

[92] I.T. Leventon, K.T. Korver, and S.I. Stoliarov. A generalized model of flame to surface heat feedback for laminar wall flames. *Combustion and Flame*, 179:338–353, 2017.

[93] N. Ren, Y. Wang, and A. Vilfayeau, S.and Trouvé. Large eddy simulation of turbulent vertical wall fires supplied with gaseous fuel through porous burners. *Combustion and Flame*, 169:194–208, 2016.

[94] L. Cattafesta, C. Bahr, and J. Mathew. Fundamentals of wind-tunnel design. *Encyclopedia of Aerospace Engineering*, 2010.

[95] P.E. Roach. The generation of nearly isotropic turbulence by means of grids. *International Journal of Heat and Fluid Flow*, 8(2):82–92, 1987.

[96] R.E. Hanson, H.P. Buckley, and P. Lavoie. Aerodynamic optimization of the flat-plate leading edge for experimental studies of laminar and transitional boundary layers. *Experiments in fluids*, 53(4):863–871, 2012.

[97] R. Narasimha and S.N. Prasad. Leading edge shape for flat plate boundary layer studies. *Experiments in Fluids*, 17(5):358–360, 1994.

[98] L.V. King. Xii. on the convection of heat from small cylinders in a stream of fluid: Determination of the convection constants of small platinum wires with applications to hot-wire anemometry. *Philosophical transactions of the royal society of London. series A, containing papers of a mathematical or physical character*, 214(509-522):373–432, 1914.

[99] B.C. Sakiadis. Boundary-layer behavior on continuous solid surfaces: Ii. the boundary layer on a continuous flat surface. *AiChE journal*, 7(2):221–225, 1961.

[100] P.L. O'Neill, D. Nicolaides, D. Honnery, J. Soria, et al. Autocorrelation functions and the determination of integral length with reference to experimental and numerical data. In *15th Australasian fluid mechanics conference*, volume 1, pages 1–4. University of Sydney, Sydney, NSW, Australia, 2004.

[101] E.E. Zukoski, T. Kubota, and B. Cetegen. Entrainment in fire plumes. *Fire safety journal*, 3(2):107–121, 1981.

[102] J.G. Quintiere and B.S. Grove. A unified analysis for fire plumes. *Symposium (International) on Combustion*, 27(2):2757–2766, 1998.

[103] G. Melina, P.J.K. Bruce, G.F. Hewitt, and J.C. Vassilicos. Heat transfer in production and decay regions of grid-generated turbulence. *International Journal of Heat and Mass Transfer*, 109:537–554, 2017.

[104] G. Melina, P.J.K. Bruce, J. Nedić, S. Tavoularis, and J.C. Vassilicos. Heat transfer from a flat plate in inhomogeneous regions of grid-generated turbulence. *International Journal of Heat and Mass Transfer*, 123:1068–1086, 2018.

[105] R.R. Gilpin, H. Imura, and K.C. Cheng. Experiments on the onset of longitudinal vortices in horizontal blasius flow heated from below. *J. Heat Transfer.*, 100:71–77, 1978.

[106] R.S.P. Hakes, W. Coenen, A.L. Sánchez, M.J. Gollner, and F.A. Williams. Stability of laminar flames on upper and lower inclined fuel surfaces. *Proceedings of the Combustion Institute*, 38(3):4515–4523, 2021.

[107] E.V. Mueller, N. Skowronski, J.C. Thomas, K. Clark, M.R. Gallagher, R. Hadden, W. Mell, and A. Simeoni. Local measurements of wildland fire dynamics in a field-scale experiment. *Combustion and Flame*, 194:452–463, 2018.

[108] E. Sluder. Understanding the influence of wind and slope on flames in wildland fires. Master's thesis, 2019.

[109] B.W. Butler, R.A. Bartlette, L.S. Bradshaw, J.D. Cohen, P.L. Andrews, T. Putnam, and R.J. Mangan. Fire behavior associated with the 1994 South Canyon fire on Storm King Mountain, Colorado. *Res. Pap. RMRS-RP-9. Ogden, UT: U.S. Department of Agriculture, Forest Service, Rocky Mountain Research Station. 82 p.*, 009(RMRS-RP-9):1–66, sep 1998.

[110] D.X. Viegas. Recent Forest Fire Related Accidents in Europe, 2009.

[111] J.J. Sharples, A.M. Gill, and J.W. Dold. The trench effect and eruptive wildfires: lessons from the King's Cross Underground disaster, 2009.

[112] R.C. Rothermel. *A mathematical model for predicting fire spread in wildland fuels*, volume 115. Res. Pap. INT-115. Ogden, UT: U.S. Department of Agriculture, Intermountain Forest and Range Experiment Station, 1972.

[113] Y. Wu, H.J. Xing, and G. Atkinson. Interaction of fire plume with inclined surface. *Fire Safety Journal*, 35(4):391–403, 2000.

[114] T.P. Grumstrup, S.S. McAllister, and M.A. Finney. Qualitative flow visualization of flame attachment on slopes. *10th U.S. National Combustion Meeting*, 2017-April:1–6, 2017.

[115] G.T. Atkinson, D.D. Drysdale, and Y. Wu. Fire driven flow in an inclined trench. *Fire Safety Journal*, 25(2), 1995.

[116] D.D. Drysdale and A.J.R. Macmillan. Flame spread on inclined surfaces. *Fire Safety Journal*, 18(3):245–254, 1992.

[117] D.A. Smith. Measurements of flame length and flame angle in an inclined trench. *Fire Safety Journal*, 18(3):231–244, 1992.

[118] P. J. Woodburn and D. D. Drysdale. Fires in inclined trenches: Time-varying features of the attached plume. *Fire Safety Journal*, 31(2):165–172, 1998.

[119] Z. Yang and H. Chen. Experimental Study on Flame Geometry along the Inclined Surface with and without Sidewalls by Using a Gas Burner. *Procedia Engineering*, 211:925–933, 2018.

[120] Y. Zhang, J. Ji, Q. Wang, X. Huang, Q. Wang, and J. Sun. Prediction of the critical condition for flame acceleration over wood surface with different sample orientations. *Combustion and Flame*, 159(9):2999–3002, 2012.

[121] J.W. Dold and A. Zinoviev. Fire eruption through intensity and spread rate interaction mediated by flow attachment. *Combustion Theory and Modelling*, 13(5):763–793, 2009.

[122] F. Morandini, X. Silvani, D. Honoré, G. Boutin, A. Susset, and R. Vernet. Slope effects on the fluid dynamics of a fire spreading across a fuel bed: PIV measurements and OH chemiluminescence imaging. *Experiments in Fluids*, 55(8), 2014.

[123] M.J. Gollner, X. Huang, J. Cobian, A.S. Rangwala, and F.A. Williams. Experimental study of upward flame spread of an inclined fuel surface. *Proceedings of the Combustion Institute*, 34(2):2531–2538, 2013.

[124] X. Silvani, F. Morandini, and J.L. Dupuy. Effects of slope on fire spread observed through video images and multiple-point thermal measurements. *Experimental Thermal and Fluid Science*, 41:99–111, 2012.

[125] W. Xie and P.E. DesJardin. An embedded upward flame spread model using 2D direct numerical simulations. *Combustion and Flame*, 156(2):522–530, feb 2009.

[126] Y. Pizzo, J.L. Consalvi, and B. Porterie. A transient pyrolysis model based on the B-number for gravity-assisted flame spread over thick PMMA slabs. *Combustion and Flame*, 156(9):1856–1859, sep 2009.

[127] R.C. Rothermel. A mathematical model for predicting fire spread in wildland fuels. *Light-Emitting Diodes: Research, Manufacturing, and Applications V*, 4278:7, 2001.

[128] P.L. Andrews. The rothermel surface fire spread model and associated developments: A comprehensive explanation. *USDA Forest Service - General Technical Report RMRS-GTR*, 2018(371):1–121, 2018.

[129] A.L. Sullivan. Inside the Inferno: Fundamental Processes of Wildland Fire Behaviour. *Current Forestry Reports 2017 3:2*, 3(2):150–171, apr 2017.

[130] Q. Liu, D. Baccarella, S. Hammack, T. Lee, C.D. Carter, and H. Do. Influences of freestream turbulence on flame dynamics in a supersonic combustor. *AIAA Journal*, 55(3):913–918, 2017.

[131] X. Yuan, N. Liu, X. Xie, and D.X. Viegas. Physical model of wildland fire spread: Parametric uncertainty analysis. *Combustion and Flame*, 217:285–293, 2020.

[132] M.A. Finney, .P. Grumstrup, and I. Grenfell. Flame Characteristics Adjacent to a Stationary Line Fire. *Combustion Science and Technology*, 00(00):1–21, 2020.

[133] G.S. Settles and M.J. Hargather. Retroreflective shadowgraph technique for large-scale flow visualization. *Applied Optics, Vol. 48, Issue 22, pp. 4449-4457*, 48(22):4449–4457, aug 2009.

[134] G.I. Taylor. The Spectrum of Turbulence. *Proceedings of the Royal Society of London. Series A - Mathematical and Physical Sciences*, 164(919):476–490, feb 1938.

[135] G. Cox. Gas velocity measurement in fires by the cross-correlation of random thermal fluctuations-A comparison with conventional techniques. *Combustion and Flame*, 28(C):155–163, 1977.

[136] S.R. Rockwell. An investigation into the use of Cross Correlation Velocimetry. page 64, 2009.

[137] R.D. Keane and R.J. Adrian. Theory of cross-correlation analysis of PIV images. *Applied Scientific Research*, 49:191–215, 1992.

[138] M. Raffel, C.E. Willert, J. Kompenhans, et al. *Particle image velocimetry: a practical guide*, volume 2. Springer, 1998.

[139] A. Umemura and C.K. Law. Natural-convection boundary-layer flow over a heated plate with arbitrary inclination. *Journal of Fluid Mechanics*, 219:571–584, 1990.

[140] S.R. Hanna, G.A. Briggs, and J.C. Chang. Lift-off of ground-based buoyant plumes. *Journal of hazardous materials*, 59(2-3):123–130, 1998.

[141] E.E. Zukoski, B.M. Cetegen, and T. Kubota. Visible structure of buoyant diffusion flames. *Symposium (International) on Combustion*, 20(1):361–366, jan 1985.

[142] J.L. Dupuy, J. Maréchal, and D. Morvan. Fires from a cylindrical forest fuel burner: combustion dynamics and flame properties. *Combustion and Flame*, 135(1-2):65–76, oct 2003.

[143] F. Tang, Q. He, and J. Wen. Effects of crosswind and burner aspect ratio on flame characteristics and flame base drag length of diffusion flames. *Combustion and Flame*, 200:265–275, 2019.

[144] L. Benny, N. Chui, N. Warner, and M.J. Gollner. A Study of Intermittent Convective Heating Effects on Fine Fuel Ignition. pages 1–9, 2019.

[145] S.S. I. Cespedes, Y. huang, J. Ophir. Methods for Subsample Time Delays of Digitezed Echo Signals.Pdf, 1995.

[146] L. Svilainis, K. Lukoseviciute, V. Dumbrava, and A. Chaziachmetovas. Subsample interpolation bias error in time of flight estimation by direct correlation in digital domain. *Measurement: Journal of the International Measurement Confederation*, 46(10):3950–3958, 2013.